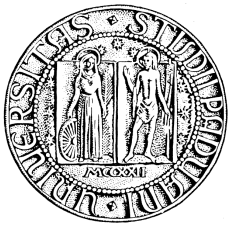

UNIVERSITÀ DEGLI STUDI DI PADOVA
Facoltà di Scienze MM.FF.NN.
Dipartimento di Fisica ed Astronomia "G. Galilei"

Corso di Laurea Magistrale in Astronomia

Dark Matter searches at Galactic Center with MAGIC data.

Relatore: Prof. Mosé Mariotti
Correlatore : Dott. Michele Doro
Controrelatore : Prof. Alberto Franceschini

Laureanda: Gaia Vanzo

Anno Accademico 2014–2015

Introduction

Since the Galactic nucleus has been discovered to be a radio source in the 1950s, the Galactic Centre has been the object of many researches: due to a remarkable activity and its proximity ($\sim 8\,\mathrm{kpc}$ away) it serves as a free and unique laboratory both for astrophysics and particle physics. It is also a promising target to search for the annihilation of dark matter into standard model particles, as the Milky Way is believed to be embedded in a halo of dark matter particles, whose density is expected to be strongly peaked towards its centre. By simulating cosmological structure formation, cold dark matter particles well reproduce the observed large scale structure of our universe. Amongst some dark matter candidates, there are non-baryonic weakly interacting massive particles, with whose mass is expected to be in the range from tens of GeV to tens of TeVs. They are expected to annihilate or decay, producing in the final states high energy neutrinos, relativistic electrons and protons with their antiparticles and also photons. The spectrum of the produced photons is predicted to cover a wide range of energy up to the mass of the DM particle, and therefore gamma ray instruments are well suited to search gamma rays produced in the annihilation process.
To perform this search we did some MAGIC! The MAGIC telescopes (Major Atmospheric Gamma-ray Imaging Cherenkov) are a stereoscopic system of Cherenkov telescopes, which indirectly observe gamma rays by detecting the Cherenkov light which is produced by the extensive air showers induced by the interaction of gamma rays with the atoms and molecules of the atmosphere.
They are situated at the Roque de Los Muchachos Observatory, in La Palma (Canary Islands, Spain) at 2200 meters above sea level, a stunning and wondrous location where the sun sets beyond inflamed clouds and a field of stars light the nights. Due to this location, the Galactic Centre culminates at high zenith angle $\sim 58^{\mathrm{o}}$ Zd and we analysed data with $62^{\mathrm{o}} < \mathrm{Zd} < 70^{\mathrm{o}}$; at such large Zd the Cherenkov light from air showers from the GC is more spread on the ground, resulting in a bigger telescope effective collection area but in a higher telescope energy threshold. We observed the gamma-ray emission above 600 GeV coming from the center of our galaxy and we did not detect any dark matter signal excess respect to the astrophysically complex gamma-ray background, composed of contribution from the GC point source, the Fermi Bubbles, the diffuse gamma ray emission, Supernovae Remnants and Pulsar Wind Nebula. Therefore, to obtain an upper limit for the gamma-ray flux, we used a work in progress code, a likelihood function (called full likelihood) which is Dark Matter oriented as it includes in the analysis the expected gamma-ray spectral shape, for dark matter with a given mass and decay channel.
Considering a Navarro Frenk and White dark matter halo model, and a $b\bar{b}$ decay channel for annihilating Dark Matter, we applied the full likelihood to data coming from the region with angular distance $0.15^{\mathrm{o}} < \theta < 0.35^{\mathrm{o}}$ from the Galactic Centre and obtained upper limits for the gamma-ray flux. This has then been converted to upper limit for the annihilation cross section $< \sigma v >$.
In Chapter 1 an overview of the production mechanism of gamma ray and gamma-ray sources

is provided, before reviewing Cherenkov telescopes and the MAGIC telescopes (Chapter 2) and dark matter evidences and properties (Chapter 3). In Chapter 4 an overview is provided of the Galactic Centre and we end by presenting the analysis and reconstruction of the data (Chapter 5) and our results (Chapter 6).
Our limits are comparable with the HESS results, which observe the GC t lower Zd and for more hours, and even more constraining above 2 TeV. A more detailed analysis will follow this work.

Introduzione

Sin da quando, negli anni '50, il nucleo Galattico stato scoperto essere una sorgente radio, il Centro Galattico stato l'oggetto di molte ricerche: essendo situato a soli $\sim 8\,\mathrm{kpc}$ e notevolmente attivo, si presenta come un singolare e prezioso laboratorio per l'Astrofisica e la Fisica Particellare. Risulta essere anche un target promettente per la richerca di materia oscura che annichila in particelle del Modello Standard, in quanto la Via Lattea si pensa sia avvolta da un alone di materia oscura, la cui densit ci si aspetta sia fortemente piccata verso il centro. Attraverso la simulazione della formazione delle strutture cosmiche, si osservato come la *cold dark matter* ben riproduca la struttura su larga scala del nostro universo. Tra i vari candidati vi sono delle particelle massive non barioniche debolmente interagenti la cui massa ci si aspetta sia tra la decina di GeV e la decina di TeV. La loro annichilazione produrrebbe, negli stati finali, neutrini altamente energetici, elettroni e protoni relativistici (e relative antiparticelle) e fotoni. Lo spettro prodotto da questi ultimi coprirebbe un'ampia gamma di energie fino alla massa di tale particella e di conseguenza i telescopi Cherenkov si presentano come lo strumento ottimale per rilevare fotoni gamma prodotti in tale processo di annichilazione.
Per fare ci abbiamo utilizzato i telescopi MAGIC (Major Atmospheric Gamma-ray Imaging Cherenkov), che sono un sistema stereoscopico di telescopi Cherenkov che osservano indirettamente la luce Cherenkov prodotta dagli sciami particellari indotti dall'interazione dei fotoni gamma con gli atomi e i nuclei presenti nell'atmosfera.
Tali telescopi si trovano all'Osservatorio del Roque de Los Muchachos, situato in La Palma (alle Isole Canarie in Spagna) a 2200 metri sul livello del mare, un luogo magico e meraviglioso, dove il sole tramonta tra rosse nuvole e il cielo un campo di stelle. Tuttavia, a causa di tale posizine geografica, il Centro Galattico culmina ad alti angoli zenitali $\sim 58^{\mathrm{o}}$ Zd e noi abbiamo analizzato dati i cui angoli Zenitali sono compresi tra $62^{\mathrm{o}} < \mathrm{Zd} < 70^{\mathrm{o}}$. A cos alti Zd la luce Cherenkov, prodotta dagli sciami di fotoni gamma provenienti dal Centro Galattico, maggiormente spalmata sul suolo, risultando in una maggiore area efficace del telescopio ma anche in una maggiore energia di soglia. Abbiamo osservato l'emissione gamma di energia superiore ai 600 GeV proveniente dal centro della nostra galassia e non abbiamo rilevato alcun eccesso di segnale di materia oscura rispetto al background astrofisico, composto dalle Fermi Bubbles, l'emissione gamma diffusa, resti di Supernova e plerion. Di conseguenza, per ottenere un *upper limit* sul flusso di raggi gamma, abbiamo usato un codice ancora in via di sviluppo, che una funzione di verosomiglianza (chiamata *full likelihood*) che maggiormente orientata alla ricerca di materia oscura in quanto nell'analisi incluso lo spettro di annichilazione per una data massa e un dato canale di decadimento.
Nel primo capitolo presenteremo una panoramica dei meccanismi di produzione di raggi gamma e le loro sorgenti astrofisiche; successivamente entreremo nell'ambito dei Telescopi Cherenkov e di MAGIC e presenteremo brevemente le evidenze dell'esistenza della materia oscura e le relative propriet dedotte dall'osservazione. Nel Capitolo 4 presentermo il Centro Galattico e infine l'analisi da noi compiuta (nel Capitolo 5) e analizzeremo i nostri risultati (Capitolo 6).

I limiti da noi ottenuti sono comparabili con quelli dei telesocpi HESS, che osservano il Centro Galattico a minori angoli Zenitali e per pi ore, e addirittura pi stringenti sopra i 2 TeV. Ulteriori studi a proseguo di questo lavoro sono previsti.

Contents

1 γ rays **7**
- 1.1 Production mechanisms of gamma rays . . . 7
  - 1.1.1 Fermi acceleration mechanism . . . 10
- 1.2 Gamma ray sources . . . 12
  - 1.2.1 Local Sources . . . 13
  - 1.2.2 Galactic Objects . . . 14
  - 1.2.3 Extragalactic Objects . . . 18

2 Cherenkov Telescopes and MAGIC **21**
- 2.1 Electromagnetic shower . . . 21
- 2.2 Hadronic Showers . . . 24
- 2.3 Cherenkov Telescopes . . . 26
- 2.4 The MAGIC Telescopes . . . 33
  - 2.4.1 Structure frames and reflectors . . . 33
  - 2.4.2 Camera . . . 35
  - 2.4.3 Trigger system . . . 36

3 The Dark Matter **39**
- 3.1 Dark Matter Evidences . . . 39
  - 3.1.1 Rotation curves . . . 39
  - 3.1.2 Gravitational Lensing . . . 40
  - 3.1.3 Imprint on the CMB . . . 42
- 3.2 Dark Matter candidates . . . 43
- 3.3 Dark Matter Annihilation spectrum . . . 47
- 3.4 Dark matter annihilation flux . . . 49

4 The Galactic Center **51**
- 4.1 The Milky Way . . . 51
- 4.2 Morphology of the Galactic Center . . . 51
- 4.3 The G2 Gas Cloud . . . 54
- 4.4 The Fermi Bubbles . . . 55
- 4.5 Dark Matter halo . . . 56
- 4.6 The MeV/GeV point source . . . 58
  - 4.6.1 Origin of the signal . . . 59

5 MAGIC Data Reconstruction and Analysis **67**
- 5.1 Data Reconstruction . . . 67
- 5.2 Data Analysis . . . 73
- 5.3 DM optimized analysis with the Full-Likelihood method . . . 76

5.3.1 The J factor 76
5.3.2 Definition of the ROI 76
5.3.3 The Full Likelihood method 79

6 Results and Conclusions **83**
6.1 Results 83
6.2 Conclusions 88

A The Fermi-LAT **i**

APPENDIXES **i**

B Cherenkov emission **ii**

C The DISP extimation **iv**

D Effective collection Area **v**

List Of Figures **xv**

List Of Tables **xix**

Chapter 1

γ rays

> I soon became convinced... that all the theorizing would be empty brain exercise and therefore a waste of time unless one first ascertained what the population of the universe really consists of.
>
> Fritz Zwicky

In 1900 the first gamma rays were discovered as produced by an excited nucleus: Paul Villard, a French physicist and chemist, observed a radiation emitted by the radium; though this radiation was more penetrating than the previous observed radiation emitted by the radium (alpha and beta rays) Villard did not give it a new name. It was in 1903 that Rutherford gave the name "gamma" rays: as alpha, beta and gamma are the first three letters in the Greek alphabet, so the corresponding rays ordered by how much they penetrates various materials.
The term 'gamma ray' refers to photons with energy above 511 keV: this lower limit is given by the annihilation of electron and positron at rest, which gives a pair of gamma rays at exactly 511 keV. If the particles are unbound(free annihilation) the resulting gamma rays, instead of a single line, will have a continuous energy distribution. So gamma rays cover a band of energy which is larger than all the rest of the electromagnetic spectrum; This broad band of energy is divided into Low Energy (LE) gamma rays (< 30 MeV), High Energy (HE) gamma rays (from 30 MeV to 100 GeV), Very High Energy (VHE) gamma-rays (from 100 GeV to 100 TeV) and Ultra High Energy gamma rays (above 100 TeV).

1.1 Production mechanisms of gamma rays

Electromagnetic radiation can be produced either by "thermal" or by "non thermal" processes. Thermal radiation is generated by the thermal motion of charged particles in matter, where the interaction between the radiation and the radiating material is so intense that the energy density of both are identical and follow a black body spectrum. On the other hand, non-thermal processes derive from violent events, where the characteristics of the emitted radiation do not depend on the temperature of the source.
For a thermal radiator with the the peak of the emission E_{max} in the gamma-ray band of the order ~ 1 MeV, we would need temperature of the order of 10^{10} K (from Wien's Law, $E_{max} = 2.82 k_B T$ where k_B is the Boltzmann constant). At such high temperatures we expect

non thermal processes to step in, and so we expect gamma rays to be produced through non-thermal mechanisms, such as Bremsstrahlung, synchrotron emission, curvature radiation, pion decay, inverse Compton scattering and synchrotron self-Compton.

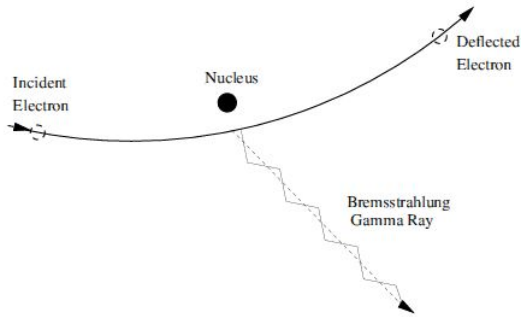

Figure 1.1: Sketch of electron Bremsstrahlung.

Bremsstrahlung (see Figure 1.1) means "breaking radiation" in German: when the electrostatic field of a nucleus deflects an incident charged particle, electromagnetic radiation is emitted with amplitude proportional to the deceleration causing the deflection and with the same direction of the incident particle. If the particle is relativistic, the deflected radiation will be beamed within an angle $\alpha \sim 1/\gamma$ where γ is the Lorentz factor. In order for Bremsstrahlung to occur, the energy of the charged particle $E = \gamma mc^2$ needs to be above a critical energy which depends on the material crossed and the resulting energy distribution of the photons follows the energy distribution of the incident charged particle. Since the energy emitted is proportional to $1/m^2$, Bremsstrahlung plays an important role mainly for light particles. Astrophysically, since protons are less motile than electrons, Bremsstrahlung is dominant with an electron-ion interaction and will produce photons of all energies up to the electron energy. Thermal Bremsstrahlung is produced by electrons with thermal(Maxwell-Boltzmann) distribution and is mostly observed in the radio domain in HII or ionized hydrogen regions and in the X-rays in the hot intercluster medium of galaxies. Non-thermal Bremsstrahlung is produced by accelerated electrons, which often have a power law distribution; this kind of distribution can be produced for instance in shock waves as in Supernova Remnants (and so the emission is in gamma rays) or in clusters of galaxies where accretion or merger shocks are present (and the emission is in the hard X-ray dominion). Electron-electron Bremsstrahlung is normally ignored compared to electron-ion Bremsstrahlung, but it was showed that in solar flares it can contribute to the hard X-ray emission. [49]

Synchrotron radiation occurs when a charged particle moves in a magnetic field: the Lorentz's force induce a rotation of the particle around the magnetic field lines resulting in a spiralized motion. The description of the phenomenon the non-relativistic case, the spiralizing particle emits photons at the Larmour frequency $\omega_L = qB/mc$, where q and m are the particle's charge and mass respectively, B is the magnetic field and c is the light velocity. In the relativistic case the synchrotron radiation is beamed into a cone of angle $\alpha \sim m_e c^2/E$ and results in a continuum spectrum which can be seen in Figure 1.2, which reaches the peak at $\omega_c = 1.5 \times \omega_L \gamma^2 \sin\theta$, where θ is the pitch angle between the velocity and the magnetic field line.

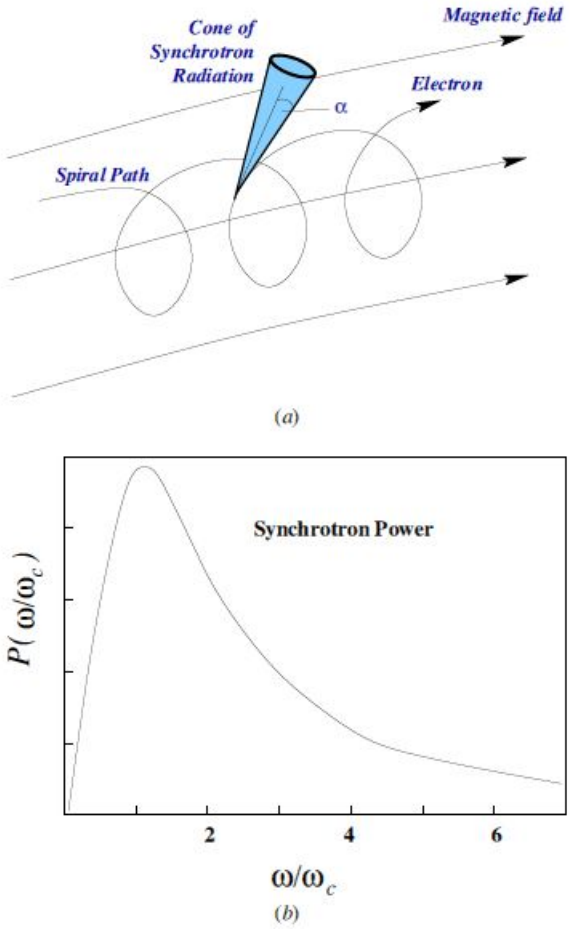

Figure 1.2: *(a)* The geometry of synchrotron emission of a spiralizing charged particle in a magnetic field. *(b)* The emitted power spectrum: it increases as $(\omega/\omega_c)^{1/3}$, peaks at ω_c and then decreases as $\exp(-2\omega/\omega_C)$

Curvature radiation is synchrotron radiation with strong magnetic field ($10^8 - 10^9$ G), so instead of spiralizing along the magnetic field line, the charged particle is constrained to move almost parallel to them with almost zero pitch angle.This happens for example in the strong magnetosphere of a pulsar.

From the inelastic scattering of relativistic protons and nuclei with the environment, mesons are produced and the larger cross section is for pions ($\pi^{\pm}$ and π^0), each with the same probability of being produced. The energy threshold for pion production is $E_{th} = 2m_\pi c^2(1 + 4m_\pi/4m_p) \sim 280$ MeV. Charged pions decay into leptons ($e^{\pm}$, $\mu^{\pm}$) and neutrinos, while neutral pions mostly decay in two photons, with the peak of the emission at $E_\gamma = m_{\pi^0}c^2/2 \sim 67.5$ MeV.

The Compton scattering is the scattering of a photon off an unbound electron: $\gamma e^- \rightarrow \gamma e^-$so that the photon transfers momentum the low energy electrons. The Inverse Compton Scattering is the collision of a high energy electron with a low energy photon which then acquires considerably energy; this acceleration mechanism is the dominant mechanism producing VHE gamma rays. Based on the energy and momentum conservation in the frame of the electron at rest, the energy of the scattered electron is $h\nu' = m_e c^2/[1 - \cos\theta + m_e c^2/h\nu]$ where θ is the angle of the scattered photon.

In the synchrotron self-Compton, the photon bath produced by the synchrotron mechanism will interact through inverse Compton with the same relativistic electrons that produced the synchrotron radiation. This kind of emission can be observed in Blazars and in Supernova Remnant, and shows a similar shape of the spectrum than the synchrotron emission, as can be seen in Figure 1.3.

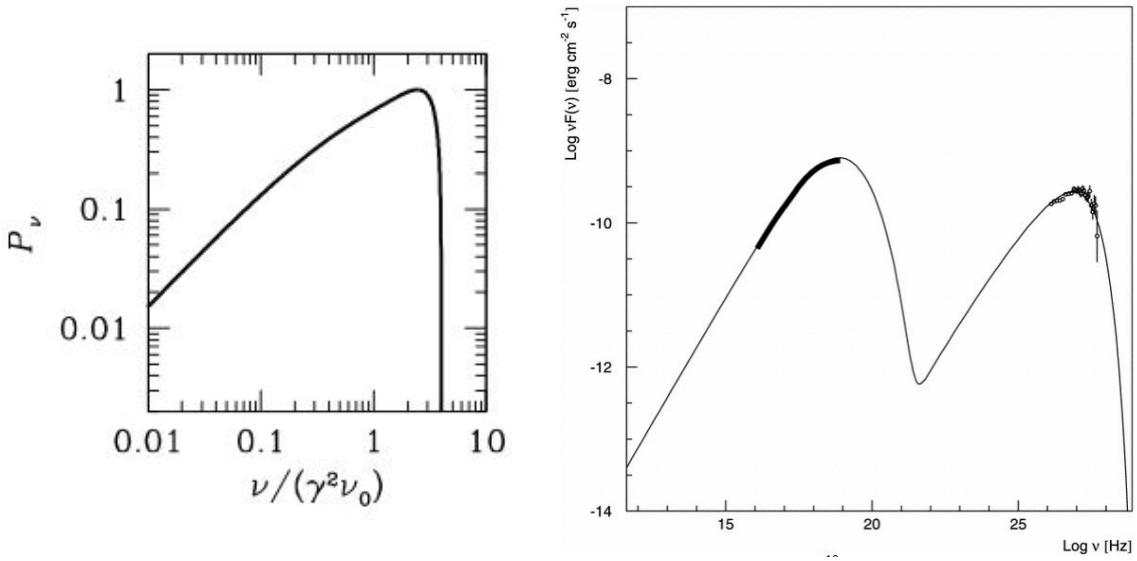

Figure 1.3: Left: specturm of Inverse Compton radiation. Right: Typical spectral energy distribution of an Active Galactic Nuclei showing the combined emission of the Inverse Compton, the peak in the lower frequency, and the synchrotron self-Compton emission, the higher frequency peak.

After the production, gamma rays might loose energy due to interactions along their path, mainly through Compton Scattering, pair production and photoelectronic absorption.

1.1.1 Fermi acceleration mechanism

The first (historically) version of the Fermi acceleration mechanism (later dubbed the *second order fermi mechanism*) was proposed in 1949 by Enrico Fermi and describes the acceleration of charged particles off magnetic irregularities. Let us look at Figure 1.4 and consider a cosmic ray with initial quadrimomentum $(E_1, \overline{p}_1)$ "scattering" elastically on a magnetic cloud that moves with $V \ll c$, and exiting it with quadrimomentum $(E_2, \overline{p}_2)$; we will label with the apex $'$ the quantities in the cloud system and without in the laboratory system.

Doing a first Lorentz transformation between the cloud and the laboratory system we obtain

$$E_1' = \gamma E - 1(1 - \beta cos\theta_1) \tag{1.1}$$

$$E_2 = \gamma E_2'(1 + \beta \cos\theta_2') \tag{1.2}$$

where $\beta = V/c$ and γ is the Lorentz factor. Applying the conservation of energy in the cloud system (i.e. the CM system) $E_2' = E_1'$,we obtain the energy gain for a single cosmic

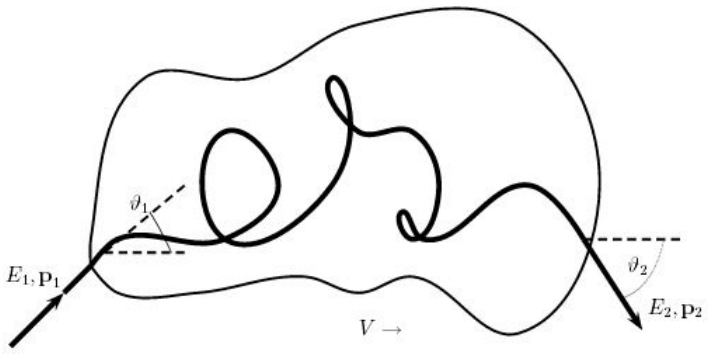

Figure 1.4: A cosmic ray "scattering" in a magnetic cloud moving with velocity V [47]

ray

$$\epsilon = \frac{E_2 - E_1}{E_1} = \frac{1 - \beta\cos\theta_1 + \beta\cos\theta_2' - \beta^2\cos\theta_1\cos\theta_2'}{1-\beta^2} - 1 \tag{1.3}$$

But the cosmic ray scatters off magnetic irregularities many times and its exit angle is random, therefore $< \cos\theta_2' >= 0$. The collision rate of the cosmic rate with the cloud depends on their relative velocity $(c - V\cos\theta_1)$ when considering ultra relativistic velocity of the particles, and therefore the collision rate is

$$\frac{dn}{d\Omega_1} \propto (1 - \beta\cos\theta_1) \tag{1.4}$$

We get $< \cos\theta_1 >$ by weighting by $dn/d\Omega_1$ and averaging over all angles:

$$< \cos\theta_1 >= \int \cos\theta_1 \frac{dn}{d\Omega_1} d\Omega_1 / \int \frac{dn}{d\Omega_1} d\Omega_1 = -\frac{\beta}{3} \tag{1.5}$$

Plugging everything in 1.1.1 we get:

$$\bar{\epsilon} = \frac{1 + \beta^2/3}{1-\beta^2} - 1 \simeq \frac{4}{3}\beta^2 \tag{1.6}$$

So since $\beta^2 > 0$, the average gain is always positive, but it's only of second order on the small parameter β so the second order Fermi mechanism is not very efficient. It can also be demonstrated that the resulting energy spectrum of the accelerated particle depends strongly on the cloud parameters.

The first order Fermi mechanism, or diffuse shock acceleration, consists in the acceleration by crossing and recrossing a shock, as can be seen in Figure 1.5: in a supernova event (as we will see in the next pages) a shock wave (SW) is formed and it expels the outer layer of the star outward. The SW denotes a discontinuity in the pressure, density and temperature, which assume higher values behind the shock wave (up stream) and lower values beyond the shock wave (downstream). Let's assume that the particle moves from downstream towards the non relativistic shock in the x direction with relativistic velocity, forming an angle θ with the plane of the shock. For isotropically distributed directions of the particles, the probability that a particle will cross the shock wave with an angle of incidence between θ and $\theta + \mathrm{d}\theta$ is proportional to $\sin\theta\mathrm{d}\theta$ and the rate at which the particles approach the front is proportional to $\cos\theta$. So the energy gain after one shock crossing results

$$\epsilon = \beta \int_0^{\pi/2} 2\cos^2\theta \sin\theta \mathrm{d}\theta = \frac{2}{3}\beta \tag{1.7}$$

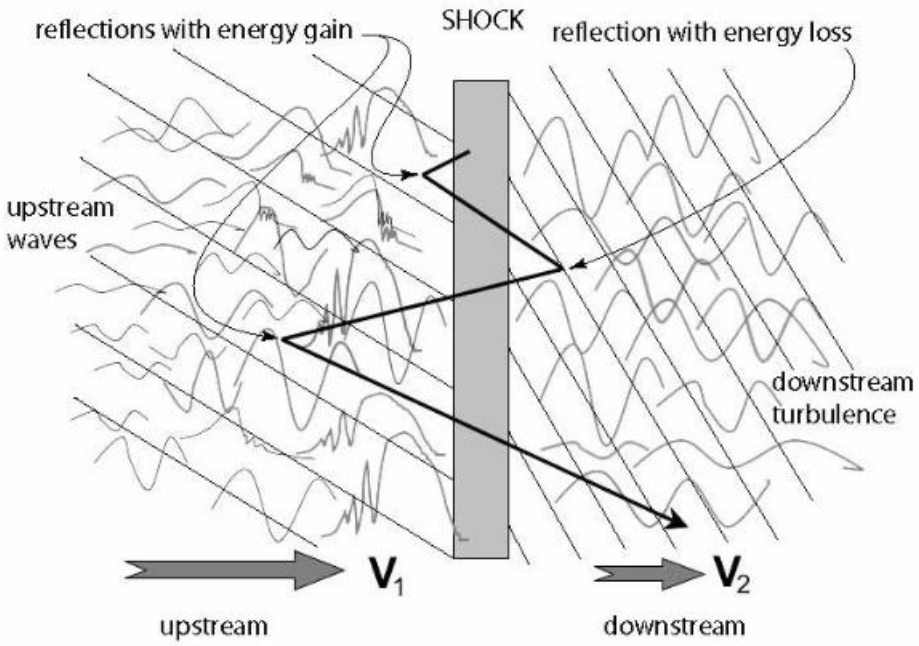

Figure 1.5: The schematic representation of the diffuse shock acceleration of a charged particle: on the left the shock is the upstream plasma flow with velocity, temperature and density larger than the downstream velocity, temperature and density. The various upstream plasma modes are sketched: upstream waves, pulsations, shocklets and whistlers. On the downstream the plasma is flowing slowly and the the downstream turbulence is sketched. The particle crossing the shock to the downstream region looses energy because it overtakes the slow waves, but the energy loss is small and returning to upstream it is scattered a second time again gaining energy. [68]

The particle is now upstream and after the next shock crossing (going back downstream), the average energy will increase of the same factor; on first order the total energy gain after many shock crossings is

$$\bar{\epsilon} = \frac{4}{3}\beta \tag{1.8}$$

It is obvious that this acceleration mechanism is far more efficient than the second order Fermi mechanism since it depends only linearly from β. Yet in one single reflection cycle (from downstream to upstream and back downstream) the particle does notgain a large amount of energy and momentem: in order for the acceleration to be efficient a high number of crossing forward and backward the shock is required. Diffuse shock acceleration so depends on the scattering process, which is a stochastic process, and assumes that the scattering is elastic: the energy of motion of the particles is conserved but not dissipated in any ways, as excitation of instabilities. The only dissipational mechanism allowed is the dissipation of bulk motional energy, from where the few accelerated particles obtain their energy gain. [68].

1.2 Gamma ray sources

The sky gamma-ray emission can be seen in Figure 1.6, but the HE and VHE gamma-ray flux arriving to us from typical gamma-ray sources is low: as an example, from the direction of the GC (a fairly strong gamma-ray source) we get a flux of below 1 photon m^{-2} yr^{-1}. To better describe the different VHE emitters we will divide them according to the distance from

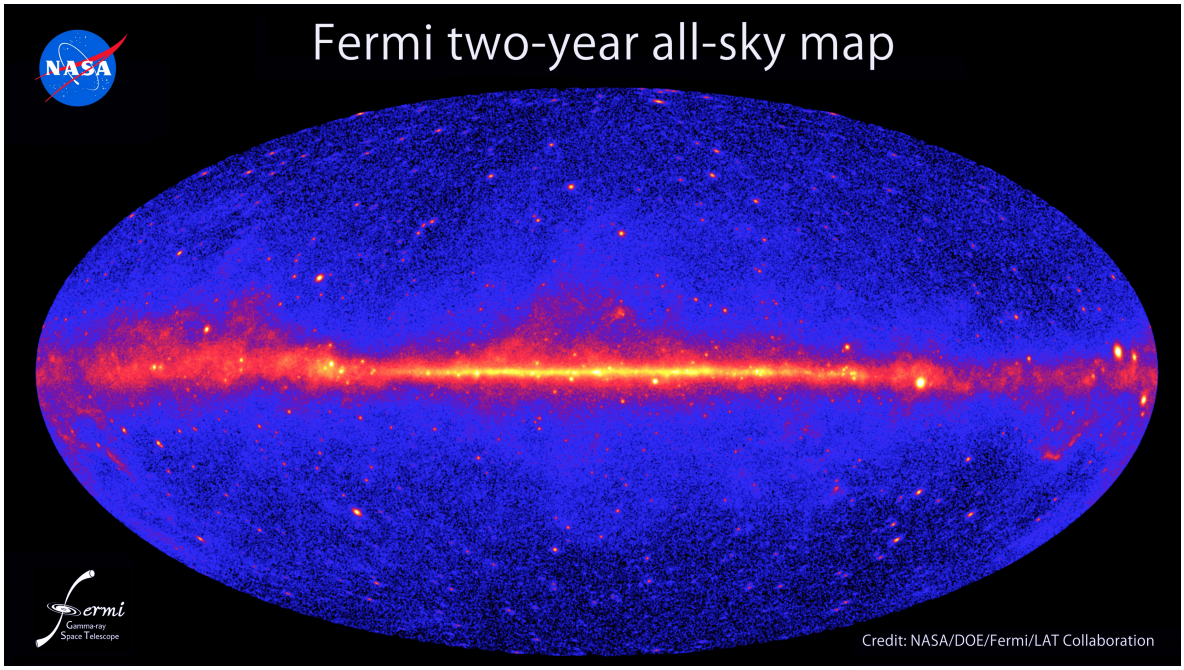

Figure 1.6: The all sky image above 1 GeV constructed from two years of observations by Fermi Gamma-ray Space Telescope. A diffuse glow fills the sky and a more intense strip is present along the galactic plane. Also discrete gamma ray sources can be seen, as pulsars or supernovae remnant. glowCredit: NASA/DOE/Fermi LAT Collaboration.

us, i.e. firs galactic and then extra galactic gamma ray sources and we will describe some of them.

1.2.1 Local Sources

Terrestrial gamma-ray flashes were first discover in 1990s by the Burst and Transient detector on board of the Compton Gamma Ray Observatory [38]; they are millisecond bursts of gamma-rays associated with thunderstorms and often also with lightning discharges (76% of the time [46]). The bursts tend to occur near the highest part of thunderstorms between 11 and 14 kms high and they are caused by lightning that stays within the storm cloud. Under the right conditions, the upper part of an interior lightning bolt disrupts the storms electric field so that an avalanche of electrons surges upward at high speed, with energies of tens of MeV and more. When these high energies electrons interact with air molecules they emit gamma rays by bremsstrahlung radiation with energies of at least of 2 MeV.

Also the sun emits gamma rays: solar flares (see Figure 1.7) are explosive phenomena that emit radiation from radio to gamma rays. This emission is a consequence of the reconnection of the magnetic field in the solar corona resulting in plasma heating and acceleration of electrons and ions to relativistic energies [37]. The emission consists of lines and continuum emission: the lines are produced by the de-excitations/acceleration of ions by interaction with the accelerated/ambient ions. The continuum emission comes from the interaction of

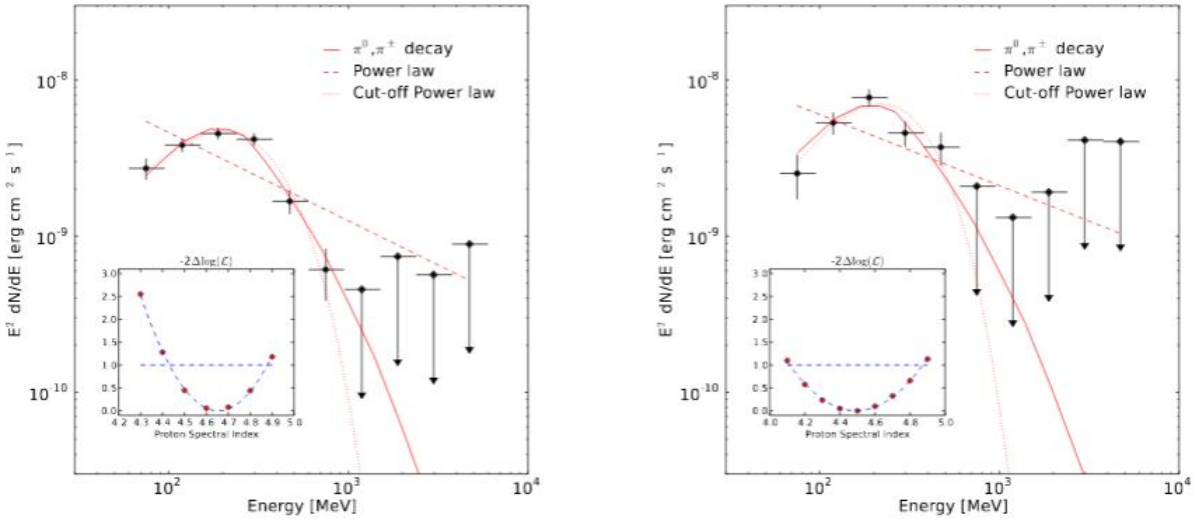

Figure 1.7: Reconstructed Fermi-LAT spectral energy distribution of the sun's flares of March 7 and June 7 2011. The vertical bars indicate 1σ statistical uncertainties, the solid, dotted and dashed lines represent respectively the pion-decay, exponential cut-off and power-law models. [37]

the accelerated particle with the solar atmosphere, which produces gamma rays through Bremsstrahlung, π productions and inverse Compton scattering.

1.2.2 Galactic Objects

The diffuse Galactic gamma-ray emission (see Figure 1.8) is mainly produced in the energy range between 20 MeV and 30 GeV by the interaction of Cosmic Rays (CR) with the interstellar medium mainly through inverse Compton, neutral pion decay from interactions of nuclei with gas, and Bremsstrahlung radiation from CR electron with the gas, from the Cosmic Microwave Background and from the interstellar radiation field. By modelling this diffuse emission it is possible to study CR origin and how they propagate in the galaxy and also to probe the interstellar medium content.

Supernovae Remnants (type II and type Ib and Ic) are the remnants of catastrophic explosion of stars of mass $M \gtrsim 5 - 8\, M_\odot$. At the end of the iron burning, there is an iron core and other nuclear reaction can not occur since they would require additional energy which is not produced because no other fusion processes are possible. At those temperatures two processes kick in: photodissociation and neutronization. With photodissociation the iron atom is dissociated in neutrons and alpha particles $Fe^{56} + \gamma \rightarrow 13\alpha + 4n$, taking away thermal energy and decreasing the internal pressure. Neutronization is inverse β-decay: $e^- + p \rightarrow n + \nu_e$; as a consequence the electron density decreases and so does also the contribution of pressure due to the electrons. The combination of these two processes causes the gravity to overcome the internal pressure, and so collapse has its onset. Due to the collapse the density increases, bringing the Equation of State to become stiffer: when the density of the collapsing core become equal as that of the atomic nuclei, the matter becomes incompressible and this brings the collapse to an end. The in falling layers bounce outward and so a shock wave is born, leaving a core composed of degenerate neutrons, a Neutron Star. A supernova remnant is the remnant of a supernova explosion, when the shock wave collides with the circumstellar gas: this accelerate particles with a diffuse shock acceleration mechanism, emitting gamma-rays.

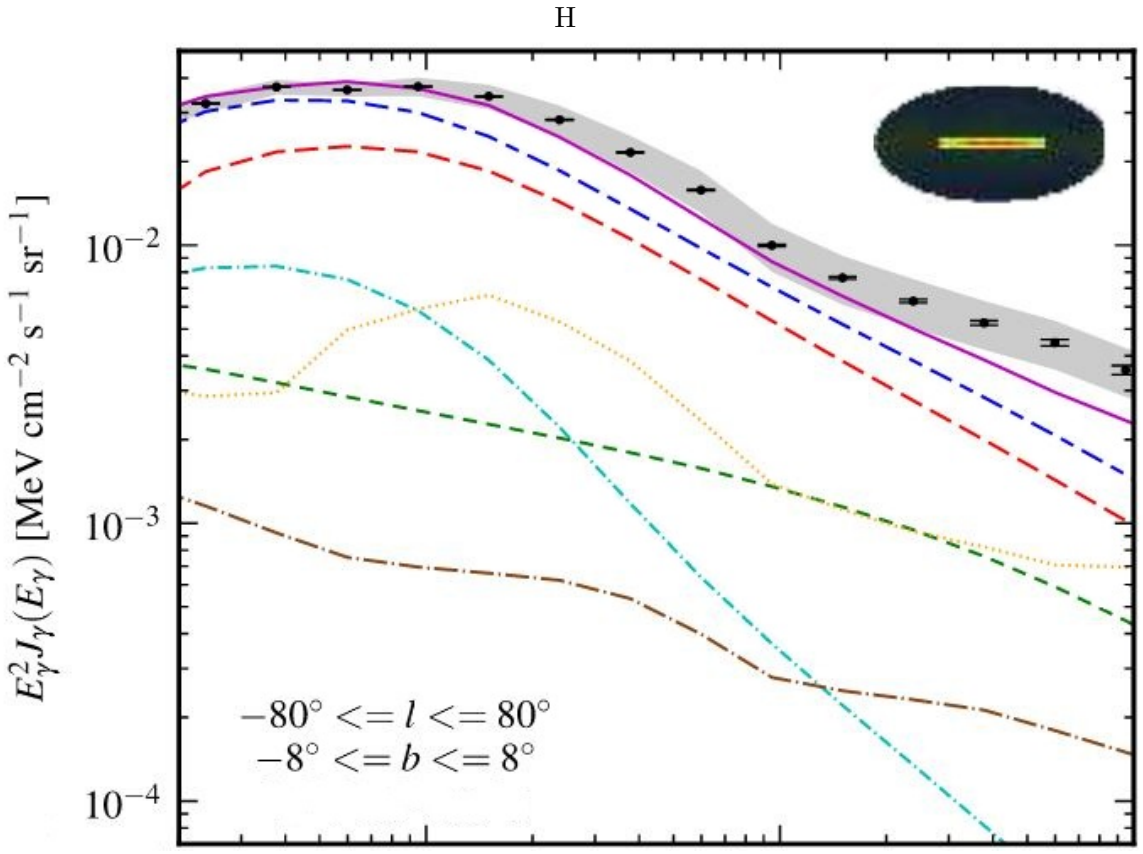

Figure 1.8: Spectrum of the Galactic diffuse gamma ray emission from the Galactic center region with $|l| \leqslant 80°$ and $|b| \leqslant 8°$ taken by the Fermi-LAT. The Fermi data are shown as point with the relative statistical error bars and the grey region is the statystical error of the Fermi-LAT effective area.The isotropic background is shown with the brown long-dash-dotted lines and the detected sources with the orange dotted lines. The model is composed mainly of three components: the π_0 decay with the red long dashed lines, the Inverse Compton with the green dashed lines and Bremsstrahlung with the cyan dash-dotted lines. The total diffuse emission is shown with the blue long dashed lines and the total emission including the sources and isotropic lines is shown with magenta lines. Credit: [**?**]

The neutron star retains the angular momentum of the progenitor star, and therefore continues to spin, now much faster than its progenitor star due to conservation of angular momentum: a Pulsar is born. Gamma radiation from pulsars can be produced through different mechanism in three physically distinct region [1]: the magnetosphere, the unshocked relativistic wind and the pulsar wind nebula as can be seen in Figure 1.9.

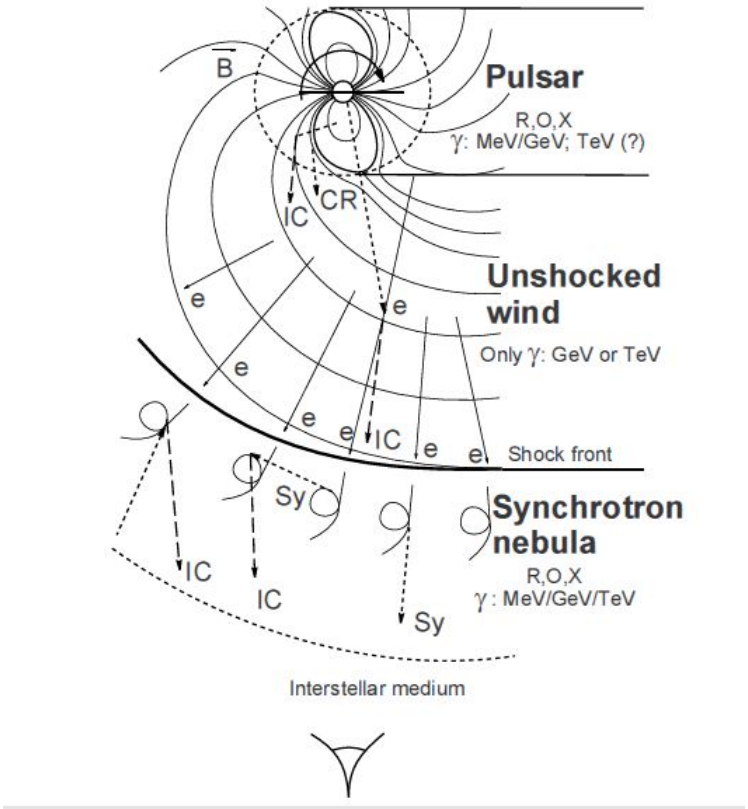

Figure 1.9: Sites and radiation mechanism of non thermal emission in pulsars: the region within the light cilinder, the unshocked wind and the synchrotron nebula. [1]

- To describe the emission in the magnetosphere we need to describe the pulsar: the simplest model is the oblique rotator magnetic dipole model characterized by two axes: the rotation axis and the magnetic axis. The particle on the surface will move along the magnetic lines: particles that are attached to closed magnetic lines will co-rotate with the star. The magnetic lines that pass through the light cylinder (at the distance where the co-rotation velocity equals the velocity of light) will be open: electrons will be accelerated along the magnetic lines, forming a radio beam centred along the magnetic axis and emitting in the radio band and a gamma ray-beam, not coincident with the radio beam, through inverse Compton scattering, synchrotron radiation and curvature radiation. The key issue of the physics of gamma-ray pulsars is the location of the γ-ray production regions, as can be seen in Figure 1.10: presently there are two models, the polar cap model and the outer gap model. The charge density in the pulsar magnetosphere is so high that it screens the electric field parallel to the B-field so that the co-rotation condition $E \cdot B = 0$ is verified everywhere except that in few locations.

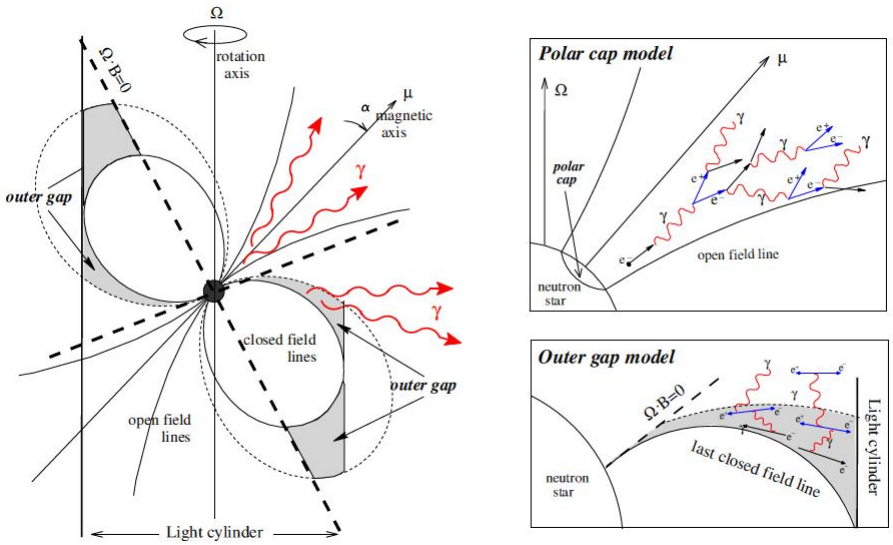

Figure 1.10: Pulsar's magnetosphere and polar cap and outer gap models.

These regions can exist close to the surface (polar cap model) or at distance close to the light cylinder (outer gap model) along the null charge surface defined by the condition $\Omega \cdot B = 0$, where Ω is the angular momentum.

This strong γ-ray emission is rapidly absorbed since it highly interact with the local magnetic field through pair production, so that it can be observed only below few tens of GeV.

- The unshocked wind (whose bulk Lorentz factor is believed to be 10^4-10^7) is magnetized but does not emit synchrotron radiation since the electrons are frozen into the plasma magnetic field. In this region inverse Compton emission is dominant because of the interaction of soft thermal photons from the surface of the neutron star with the ultra relativistic electrons of the shocked wind. The IC photons are expected to have energy between 10 GeV and 10 TeV depending on the wind's Lorentz factor.

- The pulsar wind terminates in the interstellar medium resulting in strong shocks, with cosmic rays accelerated up to 10^{15} TeV, which causes the formation of synchrotron and IC nebula around the pulsar. The synchrotron radiation is emitted both in γ rays and X-rays.

The Crab Nebula is the best know object belonging to this category of emitting objects.

X-rays binary systems consist of two objects interacting with an intense gravitational field, such as a pulsar or a black hole, and a companion star rotating around it. Some binary systems have also been observed emitting gamma-rays due to acceleration of particle, but the mechanism behind this emission is still unknown (see Figure 1.11) it might be originated from accretion energy released in the form of a relativistic jet (microquasar scenario) or from

collision of winds the(pulsar scenario), where the cometary tail of shocked pulsar wind material mimic a microquasar jet [33].

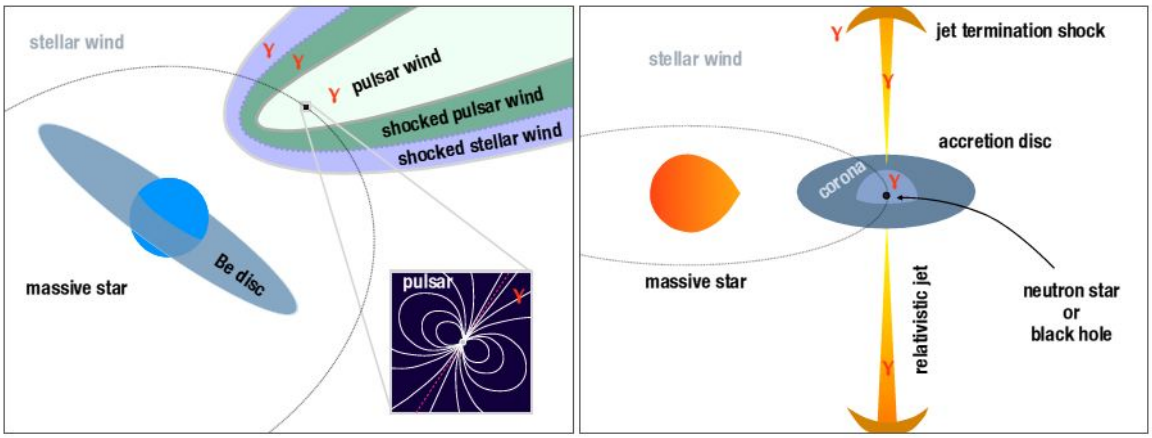

Figure 1.11: Possible scenarios for gamma-ray emission in binary sistems. Left: the relativistic pulsar wind interacts with the stellar wind of its massive companion. Gamma-ray emission can occur within the pulsar wind, near the pulsar or at the shocks terminating the pulsar and the stellar wind. Right: the accretion disk forming from infalling material from the star into the black hole or the neutron star. Gamma ray emission can arise within the jets, from the corona of the accretion disc or at the termination shock of the ISM with the jet. [33]

The Galactic Center gamma-ray emission will be discussed later.

1.2.3 Extragalactic Objects

γ-rays can not travel unimpeded in our universe: they interact with soft photons of the near-IR and UV background and form electron-positron pairs; for this reason we can not observe VHE gamma-rays from object at distance above $z \sim 1$ and photons with energy > 100 GeV have a really short mean free-path so that essentially extra galactic sources are undetectable above this energy. The main sources of extra galactic gamma rays are blazars, Gamma Ray Bursts and Starburst Galaxies.

- Starburst Galaxies take their names from the very high rate of star formation, resulting in more frequent Supernovae explosions (about ten times higher than that of normal galaxies). They emit in the infra-red because of the dust in the hot interstellar medium where the stars are forming and also gamma-ray emission is expected, produced by cosmic rays. The two prototype galaxies are M82 and NGC253 and have recently been observed in the γ-rays by Fermi-LAT [3].

- Active Galactic Nuclei (or AGN) are galaxies hosting super massive black holes of mass $10^8 - 10^9 M_\odot$ in their center and emitting a huge amount of energy over all the

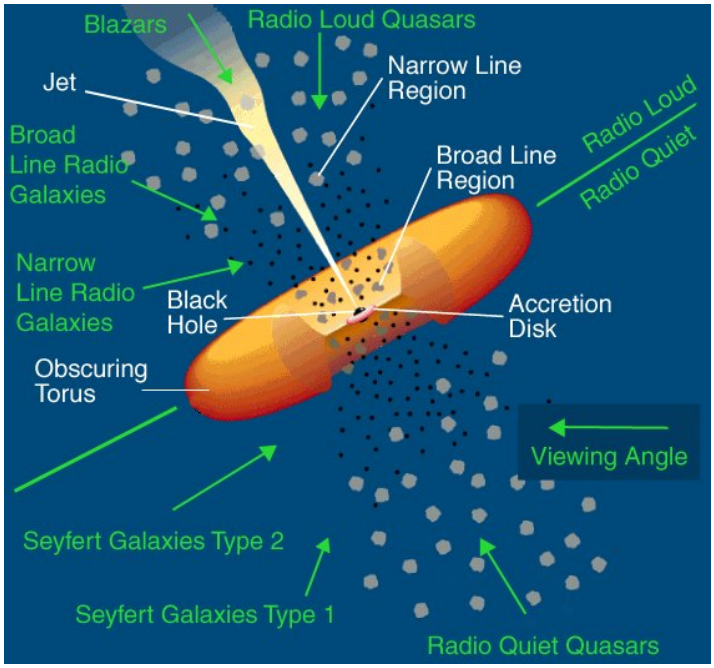

Figure 1.12: Unified model for AGNs explaining the different observed emission as a function of viewing angle. If the AGN is observed perpendicular to the direction of the jets, the torus obscures the black holes and the galaxies is seen either as radio loud or radio quiet. As the viewing angle decreases, also emission lines from the gas clouds are visibile; when the observed is aligned along the jets, their emission becomes the most dominant and the Doppler effect boosts the emission so that VHE gamma-rays are observed; this object is classified a blazar.

electromagnetic spectrum, produced from the infalling material, from the surrounding region, into the black hole. The main components are the super massive black hole, the hot accretion disk around it, two relativistic jets perpendicular to the accretion disk, the dust torus in the same plane as the disk but larger and the gas clouds distributed all around. As can be seen in Figure 1.12 different classes of AGNs can be explained by a single type of physical object observed from different viewing angles.
The jets are a consequence of the accretion disk, are highly collimated and emit in all wavelength from radio to gamma-rays; the mechanism leading to this kind of emission is still unknown but the most accredited one is the acceleration of electrons through inverse Compton and synchrotron radiation (leptonic model). Due to the variation of the infall material, also the intensity of the emission of jets can be boosted up in a short time-scale (flares). The emission of the flares do not necessarily occur simultaneously in the same wavelength nor the duration on the intensity is the same.

- The discovery of Gamma Ray Bursts (GRB) was serendipitous, as was the discovery of the pulsars, and both happened in 1967 (although the GRB discovery was not reported until six years later). GRBs are intense outburst of gamma-rays (with energy from 5×10^{52} erg to 3×10^{54} erg) lasting from milliseconds to ten of seconds, overshining the entire sky in γ-ray, and later followed by afterglows in the other wavelengths. As for AGN, the physic mechanisms behind the GRB are still unknown, but they might origin from a "relativistic fireball" born either by the merging of two compact objects or by the core collapse of a rapid rotating massive star with mass $M > 100\,M_{\odot}$. Since the time scale of the emission is so short, also the dimension of the emitting regions must be small, e.g. for a GRB of 3 ms we would need an emission region of 10^8 cm. In such a small space and such high density the photon pair production has such a large

cross section that it would be impossible for gamma-rays to escape, so the gamma-ray emission is expected to be beamed into two ultra relativistic jets of angle $\theta \sim 1/\Gamma$ with Γ the Lorentz factor of the accelerated particles, which is of the order of $10^2 - 10^3$. When there is a variation in the injection rate of particles in the jets, shell of relativistic material are formed and they interact with each other causing internal shocks, the origin of GRB. The afterglow is due to the external shock of the termination of jets with the interstellar medium (see Figure 1.13).

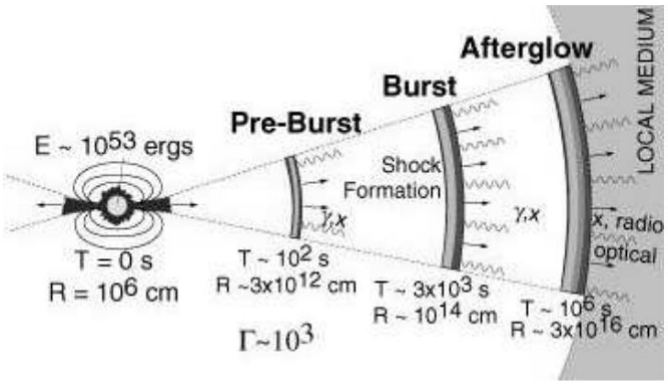

Figure 1.13: Jet structure of a GRB. The GRB origins from the shocks inside the jets while the afterglow from the interaction fo the relativistic shell with the interstellar medium.

Chapter 2

Cherenkov Telescopes and MAGIC

> It would be most satisfactory if physics and psyche could be seen as complementary aspects of the same reality.
>
> Wolfgang Pauli

As we already discussed in the previous chapter, the gamma-ray band covers many order of magnitude: to perform measurements on such a large energy range different instruments with different techniques are necessary. So since below 30 MeV the Compton process is the dominant interaction, Compton telescopes are used; in the HE and VHE range instead pair production is dominant.
HE gamma rays are detected by satellite-born instruments and due to the large cost and technical hinderances in lifting heavy weights in payloads, they have a small detection area but since the typical gamma-rays flux at in the core energy range of these telescopes is larger than at VHE, the small area is efficient to take data. The physical process behind the detection technique of these instruments is the electron positron pair-production in converter material and to estimate the energy of the gamma-ray an electromagnetic calorimeter is used. Currently AGILE (AstroRivelatore Gamma a Immagini Leggero) and the Fermi-LAT (Large Area Telescope, see Appendix A) have better angular and energy resolution due to a larger sensitive detector area than their predecessor EGRET (Energetic Gamma Ray Experiment Telescope).
VHE gamma-rays are detected by ground based telescopes through the detection of the secondary cascade particles produced in the interaction of the gamma-rays with the atmosphere. The technique at the core of this approach is the study of the cascade particles referred as atmospheric showers which can be of electromagnetic or hadronic nature; the secondary particles produces in the cascade radiate through Cherenkov emission (see Appendix B) low energy (visible to ultraviolet)photons.

2.1 Electromagnetic shower

Electromagnetic showers are produced by the interaction of gamma-rays with the electric field of atmospheric atoms and molecules through pair-production: since muon and antimuon are more massive and therefore the cross section is smaller, the channel of the pair production goes mainly into electron and positron $\gamma\gamma \rightarrow e^+e^-$; this process has a energy threshold of $E_{th} = h\nu = 2m_ec^2 \sim 1$ MeV and so VHE gamma-rays are involved. The electron and

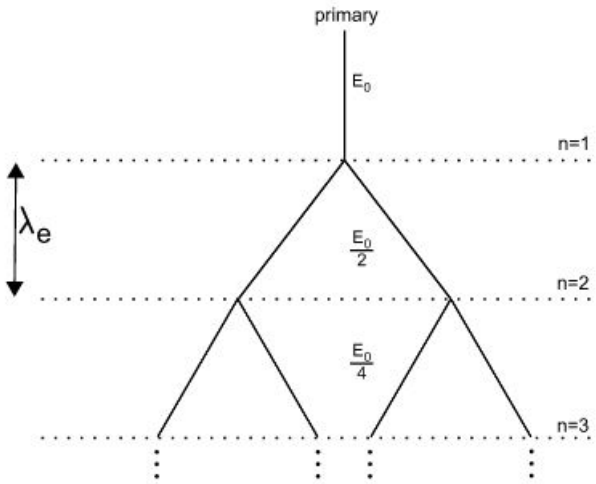

Figure 2.1: Electromagnetic shower as described by the Heitler model

positron so produced then radiate photons through Bremsstrahlung $e^{\pm}(\gamma) \rightarrow e^{\pm}\gamma$, leading to a cascade which grows through these two electromagnetic reactions (pair-production and Bremsstrahlung) and hence the name *electromagnetic shower*. While the shower so develops, the number of particles increase (and it can be seen that on average the shower consists of 2/3 positrons and electrons and 1/3 photons) and the energy of each particle decreases: when the mean energy is equal to the critical energy, which in air is $E_c \sim 84$ MeV, the shower reaches its maximum number of produced electrons. Below this energy, energy losses through ionization becomes dominant over energy losses through Bremsstrahlung and the cross section for photoelectric absorption and Compton scattering becomes dominant over pair production: at this point the number of particles gradually diminishes and the shower dies away due to the absorption of the atmosphere.
To describe the development of the shower, a simplified model that can be used is the Heitler model, which as can be seen in Figure 2.1, assumes that an electromagnetic particle with energy E interacts after one splitting length $\lambda_e = \ln 2 X_0$ (where $X_0 \sim 37\text{g/cm}^2$ is the electromagnetic radiation length, i.e. the mean distance a particle travels before its energy is reduced by a factor e) and the two particles produced have energies $E/2$. So the number of particles after each splitting length increases by a factor two, and after n splittings the number of particles is $N_n = 2^n$ and their energy $E_n = E_0/N_n$. So at the shower maximum, where the electrons have energies $E_c \sim 84$ MeV, the number of particles is $N_{max} = E_0/E_c$ and the position is $X_{max} = X_0 \ln(E_0/E_c)$: the number of particles at the shower particles is proportional to the primary particle energy E_0 and the depth of shower maximum depends logarithmically on E_0.

A more defined description was formulated by Rossi and Greisen [65]: they calculated the number of protons and electrons as a function of the atmospheric depth $t = X/X_0$:

$$N_e(t, E_0) = \frac{0.31}{\sqrt{\ln(E_0/E_c)}} \exp[t(1 - 1.5 \ln s)] \tag{2.1}$$

where s is called the age parameter and is 0 at the first interaction, 1 at the shower maximum and 2 where the shower dies out; this parameter is defined as

$$s = \frac{3t}{t + 2 \ln / E_0/E_c)} \tag{2.2}$$

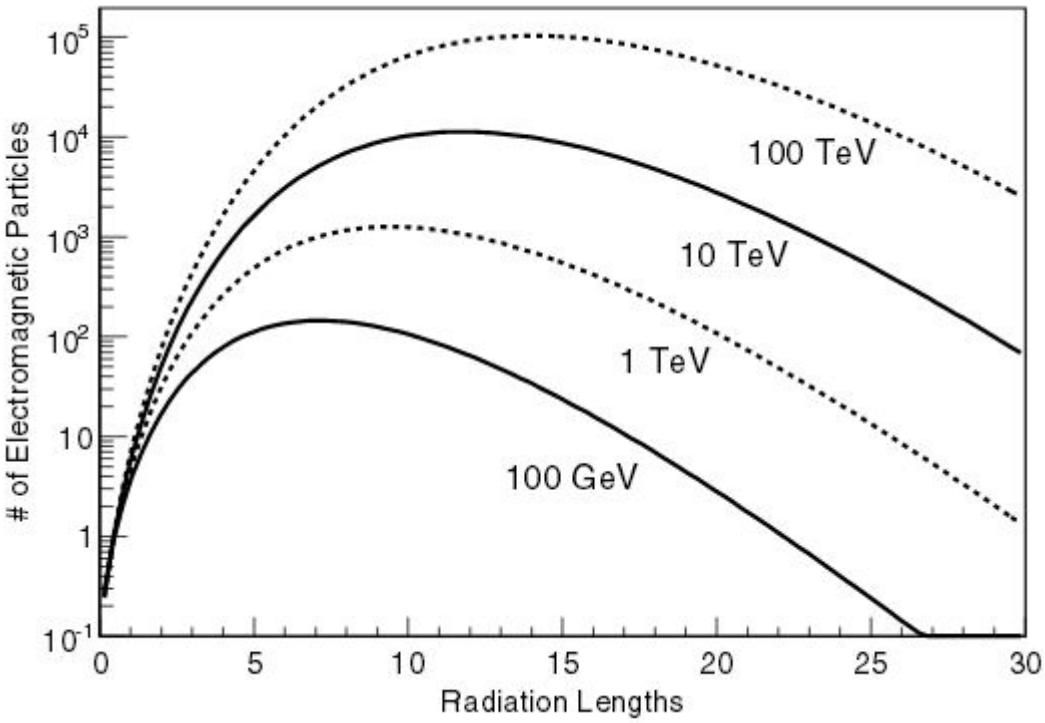

Figure 2.2: The longitudinal development of an electromagnetic shower for different primary gamma ray energies. The x axis is the atmospheric depth expressed in unit of radiation lengths: sea level is $\sim$ 28 radiation lengths, 2600 m a.s.l. is $\sim$ 20 radiation length and 4300 m a.s.l. is $\sim$ 16.5 radiation lengths, and 5200 m a.s.l. is $\sim$ 14.7 radiation lengths.. The y axis is the number of electromagnetic particles in the shower. [70]

So at the shower maximum results

$$N_e(max) = \frac{0.31}{\sqrt{\ln(E_0/E_c)}} \frac{E_0}{E_c} \tag{2.3}$$

For γ rays of energy from 20 GeV to 20 TeV the maximum number of shower particles is about 250 to 450 g/cm^2 corresponding to an atmospheric height of about 7 to 12 km above the ground. If we consider a 300 GeV gamma-ray, its shower maximum will be at 9 km on sea level and it will die out at 1 km on sea level. Gamma-rays of energy lower than $\sim$ 200 GeV will produce a shower which will die out before reaching the MAGIC telescopes, situated at $\sim$2200 at sea level.

The shower will be defined not only by the longitudinal momentum but also by the transverse momentum: this is connected to the multiple scatterings of angle θ that electrons and positrons suffers from the atomic nuclei, causing a dispersion from the central axis of the cascade. After the particles has undergone many scatterings at a distance x, the distribution of the scattering angles θ will be a gaussian centered at zero with a square root standard deviation

$$\sigma = \frac{14.1\text{MeV}}{E_e} \sqrt{\frac{x}{X_0}} \tag{2.4}$$

where the pedix e refers to the electron case. So after a a distance d the particle has acquired a transverse distance from the shower axis of $y = 1/\sqrt{3}x\sigma$

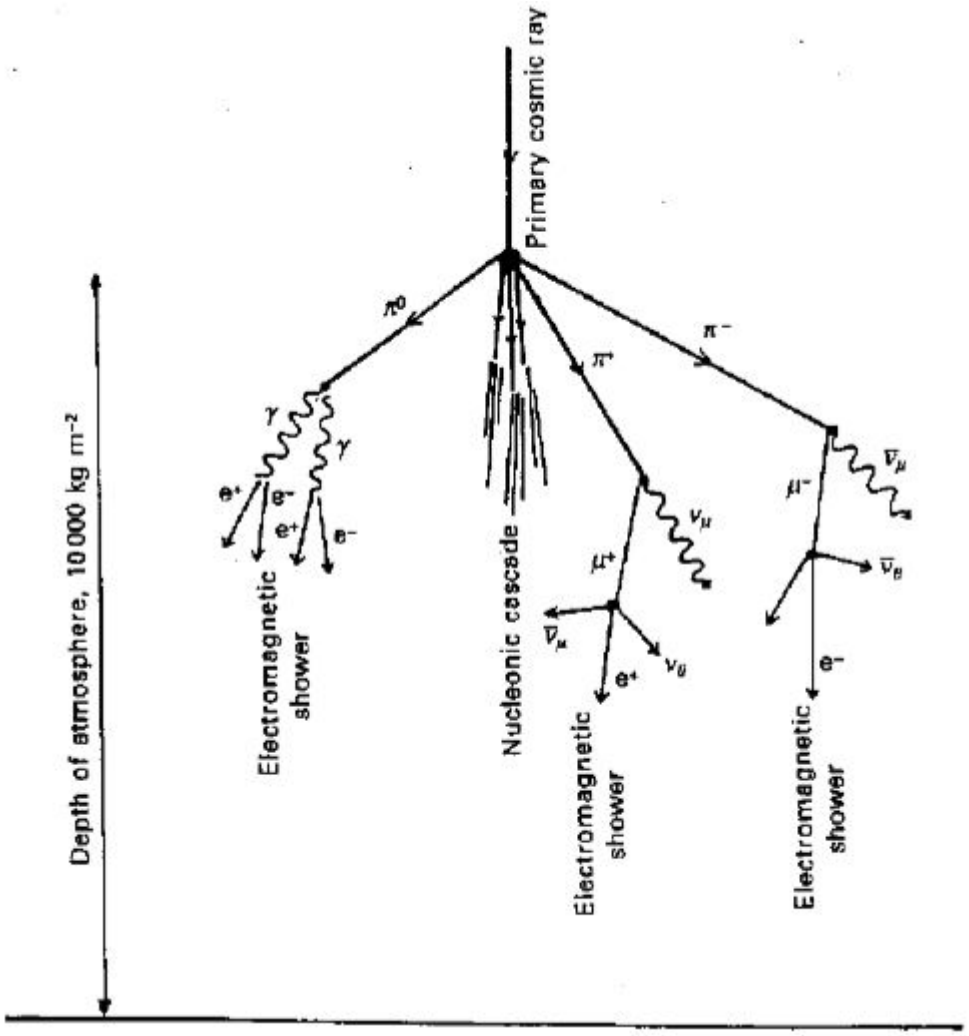

Figure 2.3: A schematic diagram of the developement of the interaction of a Cosmic Ray with the Earth's atmosphere [57]

2.2 Hadronic Showers

Hadronic showers are produced by the interaction of Cosmic Rays with the atmosphere. Cosmic Rays are high energetic particles, composed for the 98% of protons, helium and heavier nuclei and for the residual 2% of electrons and positrons. The hadronic showers are initiated mostly by protons interacting through the strong interaction with the atmospheric nuclei creating pions $\sim 89\%$, kaons $\sim 10\%$ and nucleons.

As can be seen in Figure 2.3, hadronic showers are characterized by three features:

- an hadronic core of secondary nucleons and charged pions who are energetic enough to perpetuate nuclear collisions until the energy per particle drops below that required for the pions production, at about 1 GeV

- a muonic component, formed by the decay of pions and kaons;

$$\pi^{\pm} \to \mu^{\pm} + \nu_{\mu}(\overline{\nu}_{\mu}), \tag{2.5a}$$
$$K^{\pm} \to \mu^{\pm} + \nu_{\mu}(\overline{\nu}_{\mu}), \tag{2.5b}$$
$$K^{\pm} \to \pi^{\pm} + \pi^{0} \tag{2.5c}$$

  The low energy muons have time to decay as follow

$$\mu^{\pm} \to e^{\pm} + \nu_{\mu}(\overline{\nu}_{\mu}) \tag{2.6}$$

  and then generate an electromagnetic sub shower; many muons are produced with very high energies and are slowed down only by ionisation through small energy losses, so they arrive amlost intact at the Earth's surface. More in details, muons' mean lifetime in their rest frame is 2.2×10^{-6} s, but to an external observer their mean lifetime is $2.2 \times 10^{-6} \times \gamma$ where γ is the Lorentz factor. Muons with $\gamma \geqslant 20$ survive intact to the Earth's surface. This muonic component sharply defines the difference between hadronic and electromagnetic shower, where the muonic component is absent.

- an electromagnetic component, due to the decay of pions into two gammas that then produce electromagnetic sub showers. Since neutral pions are one third of the total pions produced, about one third of the energy goes into this electromagnetic sub shower.

To describe hadronic showers the Superposition model can be used, which assumes that a nucleus of mass A and energy E_0 act like and independent nucleon with energy $E_n = E_0/A$; then the shower maximum can be expressed as

$$X_{max} = \ln(\frac{E_0}{AE_c})X_n \tag{2.7}$$

where X_n is the nuclear interaction length in air. So heavier nuclei are less penetrating and create showers which develops largerly. Since the nuclear interaction length is $\sim 100\,\mathrm{gr\,cm^{-}}2$, larger than the radiation length, the hadronic shower will have a larger transversal momentum.

Due to the different interactions involved, electromagnetic and hadronic showers show different features, as can be seen in Figure 2.4: since different kind of particles and many sub showers can develop, hadronic showers are more asymmetric than electromagnetic shower. In addition, secondary particles produced by hadronic shower acquire a bigger transverse momentum, so that hadronic showers feature a wider lateral spread than electromagnetic showers.

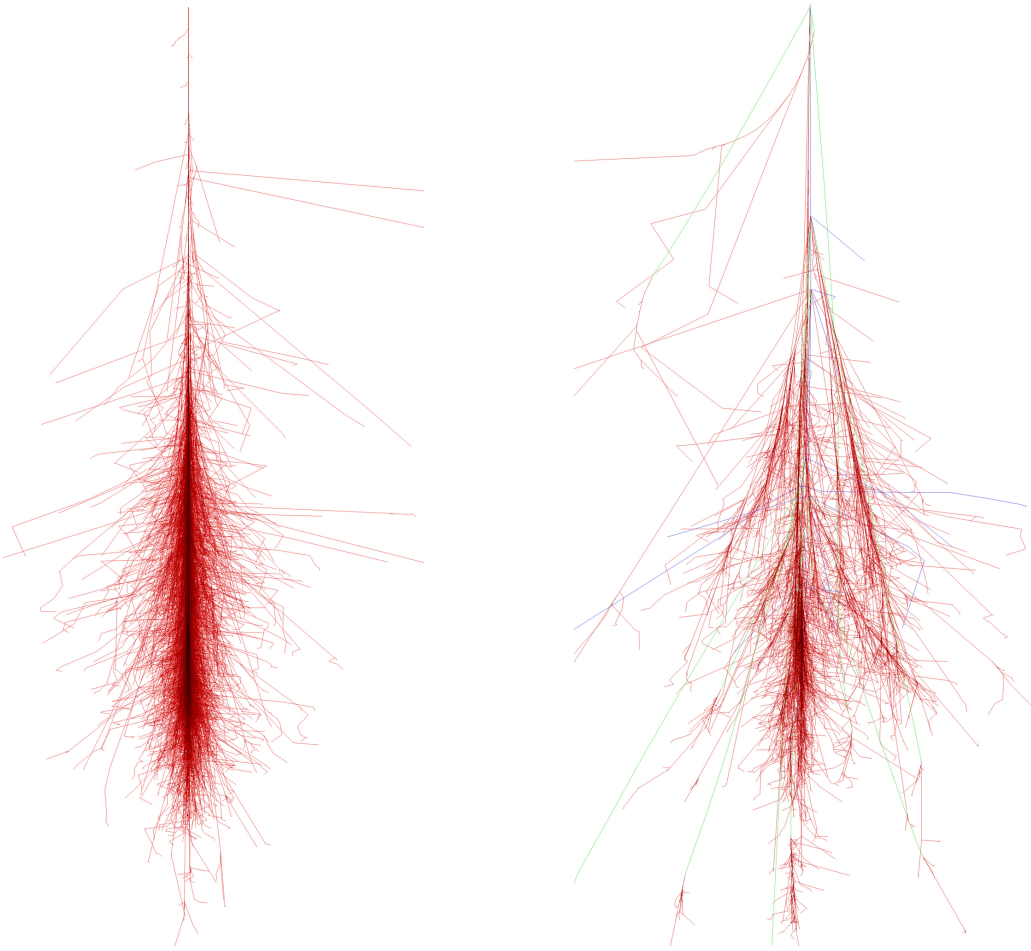

Figure 2.4: Simulated electromagnetic shower on the left and hadronic shower on the right produced by a primary particle with 100 GeV energy: the red shows the tracks produced by electrons, positrons and gammas while the green and the blue show the tracks produced by muon and hadrons respectively. The different features of the two showers can be seen: the left one is slender and at lowest approximation axially symmetric along the direction of the primary gamma ray; the right one is irregular and might contain electromagnetic subshowers [61].

2.3 Cherenkov Telescopes

The Cherenkov light is emitted by the secondary particles produced in the cascade, through the emission of low energy (visible to ultraviolet) photons in a ring of cone of light where the shower axis is the direction of the charged particle and the opening angle is the Cherenkov angle. Since this angle depends inversely on the refraction index (see equation B.1) which decreases as the altitude decreases, the lower the altitude, the broader the Cherenkov angle becomes, as can be seen in Figure 2.5.

The resulting emission is the superposition of these rings, which on the ground produces a rather uniformly illuminated Cherenkov light pool. Since the Cherenkov angle is on average 1^0 and the light is emitted at 10 to 12 km a.s.l., the radius of the light pool is $\sim$ 125 meters wide and the arrival time distribution is very short, of the order of nanoseconds.

[h!]

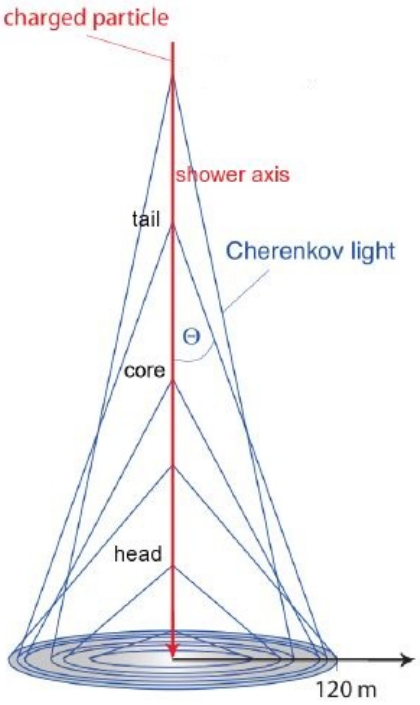

Figure 2.5: Cherenkov lightpool as a superposition of Cherenkov emission at different altitudes: due to the dependence of the rifraction index, the Cherenkov angle decreases as the altitude decrease: at 10 km a.sl. it is 0.66, at 8 km a.s.l. it is 0.74 and at sea level it is 1.4. The light is emitted at $\sim$ 10 km a.s.l. and then, depending on the altitude at which is emitted, the Cherenkov emission is divided into tail, core and head.

To detect and record the Cherenkov light produced by an air shower, three things are required: a mirror to gather and focus the light, a fast detector and a means to trigger/record the image.

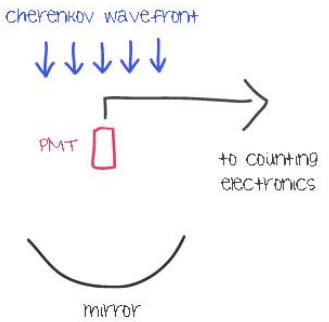

Apparently a Cherenkov telescope might seem a classical optical telescope, but the difference lays in the core of this type of emission: both telescopes are focused to where the photons are produced, but while optical telescopes are focused to infinity, Cherenkov telescopes are focused to where the secondary photons are produced i.e. to $\sim$ 10 km a.s.l.
First-generation atmospheric Cherenkov telescopes (ACT) were very simple: they consisted of a single light detector in the focal plane of a searchlight mirror, coupled to fast pulse counting electrons. This system though had problems: more than 99% of the events that trigger the camera are induced by background events and it was not possible to extract gamma-ray events from the overwhelming background. The background basically consists of hadronic showers, electron initiated showers, muons produced in hadronic showers, the night sky background (NSB) produced by all sources of diffuse light in the sky and light pollution.

The development of the Cherenkov imaging technique was the result to these problems, giving birth to IACT: Imaging Atmospheric Cherenkov Telescopes. In the focal plane of a large reflector there is an array of photomultiplier tubes (PMTs) which constitutes as a camera ad is used to record Cherenkov light picture of each air shower. When the camera is

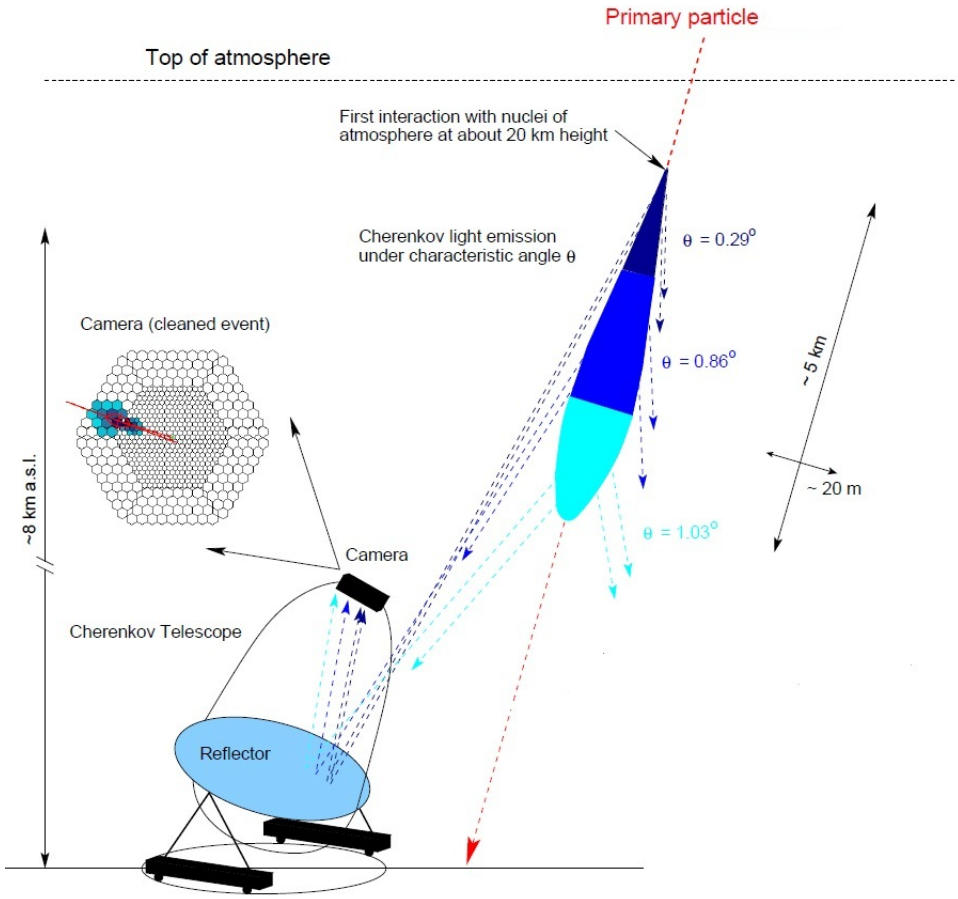

Figure 2.6: The primary particle interacts with the molecules in the atmosphere initiating atmospheric showers: the blue shows the head, the pale blue the core and the cyan the tail of the shower. The particles produced in the shower which exceed the speed of light emit Cherenkov radiation showed as the dashed lines. Then, if the Cherenkov telescope is placed into the light pool, it collects the photons and reflect them into a pixelized camera, forming an elliptical shape. Its center corresponds to the core of the shower while its extremities are the head and the tail of the shower. Its major axis is the projection of the shower axes into the plane of the camera.

triggered, using a trigger system, the light level in each pixel is recorded and later analysed offline. The implementation of IACT lay in the imaging part: the discrimination between hadronic and gamma events can be done by analysing the images produced by Cherenkov photons when they are focused on the camera and also the incoming direction of the primary particle can be obtained.
So let us follow the path of a γ-ray photon in Figure 2.6: it arrives at the top of the atmosphere and it interacts with the atoms and molecules, producing an atmospheric shower. The relativistic particles so produced emit Cherenkov light and if the telescope is in the Cherenkov lightpool, this photons are reflected by the mirror, focused on the camera where the signal is converted from electromagnetic to electronic, forming an image, which can be characterized by some parameters, called the *Hillas parameters*. As can be seen in Figure 2.7, the main Hillas parameters are the following:

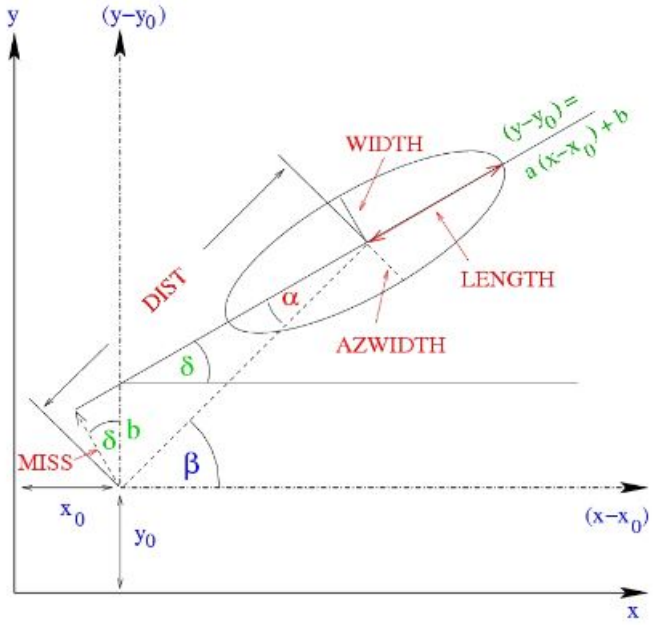

Figure 2.7: Illustration of the Hillas parameters.

size the total number of collected photons in the image;

lenght the major semi-axis of the ellipse; it is related to the longitudinal development of the shower;

width the minor semi-axis of the ellipse; it is related to the transversal development of the shower;

dist the distance between the center of the ellipse and the center of the camera;

alpha the angle between the major axis of the ellipse and the line connecting the center of the ellipse to the center of the camera;

number of islands number of spatially separated clusters of pixel.

As can be seen in Figure 2.8, one of the more immediate discriminator between hadronic and gamma events is the width: as already discussed, particles in hadronic showers acquire a larger transversal momentum than in gamma showers, resulting in a wider image, whose major axis is difficult to identify. Another clue is the time spread of the event: since strong interactions are involved, the interactions last longer, leading to a time spread of $\sim$ 10 ns for hadronic events against the $\sim$3 ns of the gamma events. Other differences can be seen in Figure 2.9.

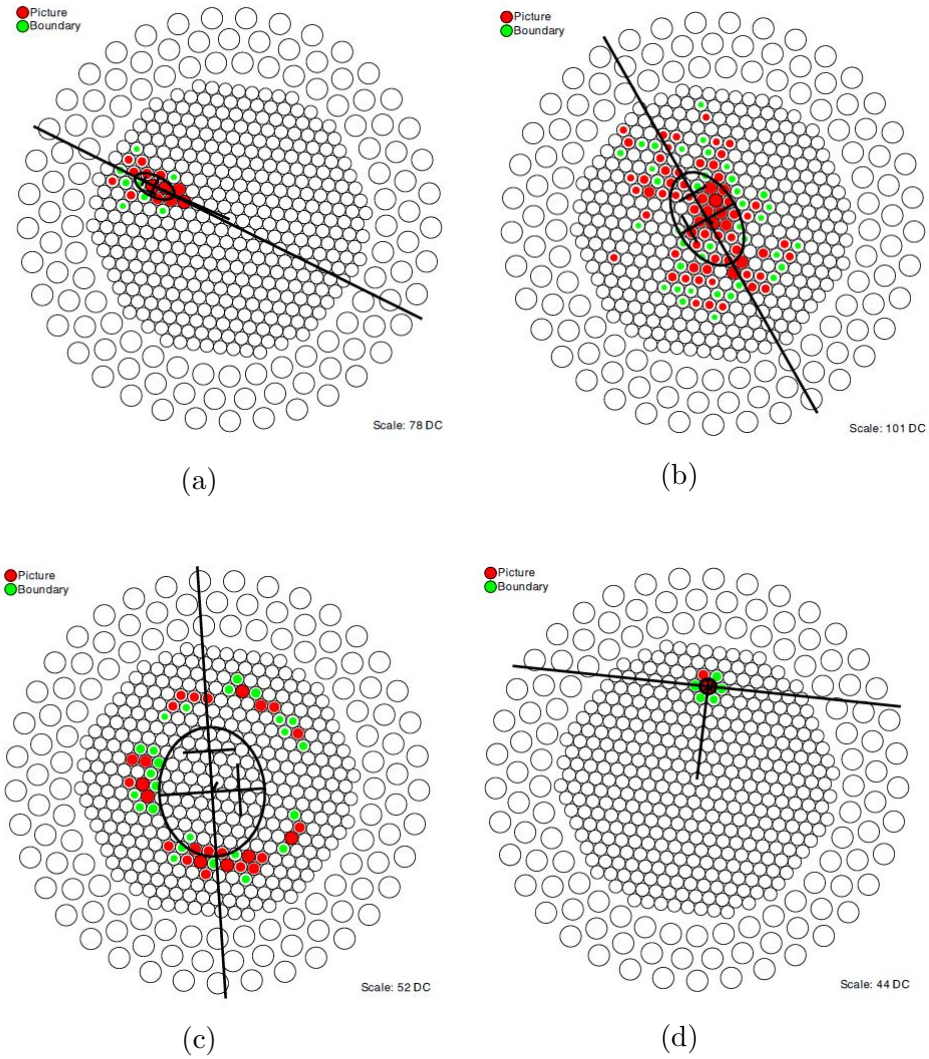

Figure 2.8: On top: example of an image in a camera as produced by a gamma shower (a) and by a hadronic shower (b). The gamma event has an elliptical very compact shape while the hadronic event hs a roundish fragmentated shape. On bottom: image produced by a muon event (c) and by a background night event (d). Since muons emit cherenkov light in a cone at a nearly constant angle as they propagate through the lower atmosphere, they produce a ring or an arc on the camera.

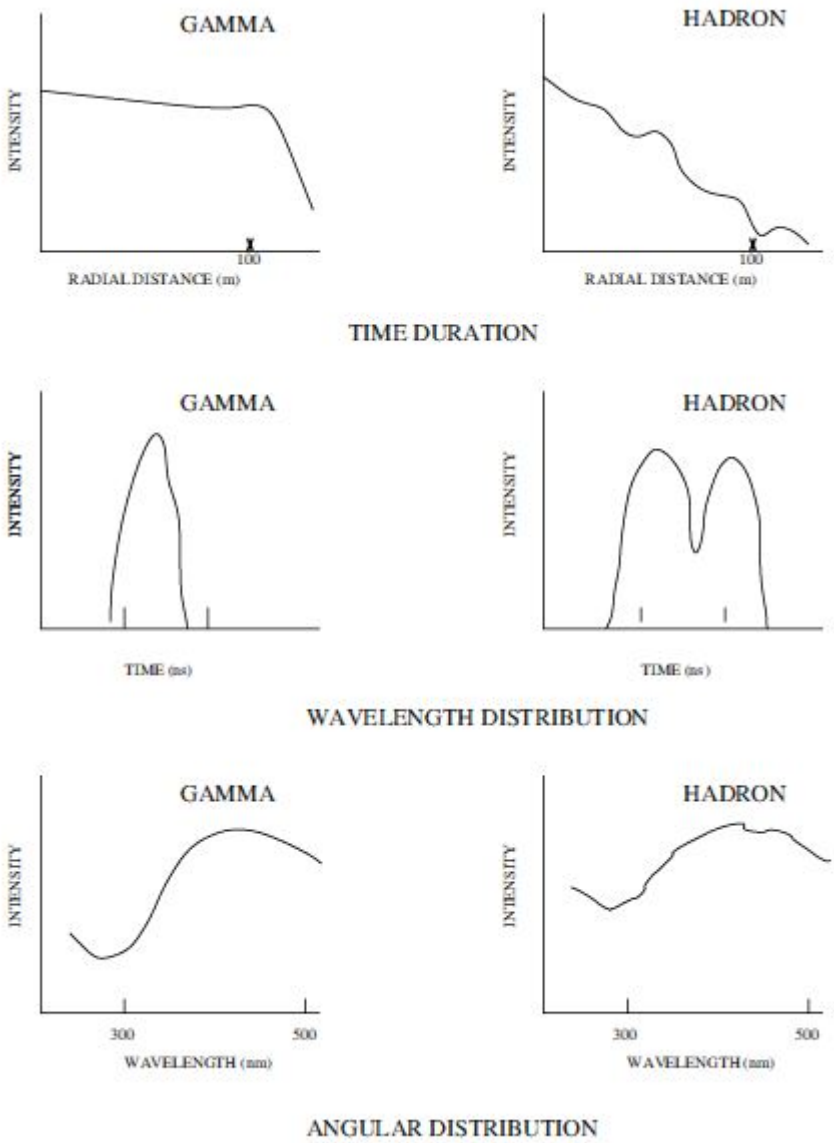

Figure 2.9: Different distribution of some parameters for gamma(left) and hadronic (right) showers. On top, the radial distribution of light intensity about the shower core at detector level: images produced by gamma events are more compact. In the middle, distribution of arrival times of the photons at detector: the time spread of the hadronic events is bigger than that of gamma evets. On bottom, the intensity of Cherenkov light as a function of wavelength. [75].

The atmospheric Cherenkov imaging technique is significantly improved by the use of an array of telescopes where the distance between each telescope is of the same order of the lateral spread of the Cherenkov light. This stereoscopic technique has many advantages: since multiple images of the same showers are obtained, the intersection point of the image major axes yields the shower direction and also the shower maximum can be obtained. In addition a coincident trigger between telescopes is used, reducing the energy threshold and improving the hadron-gamma discrimination and the angular resolution. The trigger also allows to suppress the muons events, since muons produce an image only in the telescope concerned.
Currently three IACT systems are operating: H.E.S.S., VERITAS and MAGIC and in the

next years CTA will be build.
H.E.S.S. (High Energetic Stereoscopic System) [29] [1] is a stereoscopic system situated in Namibia, near the Gamsberg mountain which operates in the energy range between tens of GeV to tens of TeV. As can be seen in Figure 2.10 it constitutes of five telescopes, four with a mirror of 12 meter in diameter segmented into 382 round mirror facets of 60 cm in diameter and the fifth with a 28 meters mirror in diameter segmented into 875 hexagonal facets of 90 cm in diameter. The field of view of the camera is 5 degrees. The initial four telescopes (Phase I, which became operational in December 2003), are arranged to form a square whose side lenght is 120 meters (approximately the diameter of the lightpool); the fifth telescope (Phase II, which became operational in July 2012) is situated in the center of the array to increase the telescopes performance.

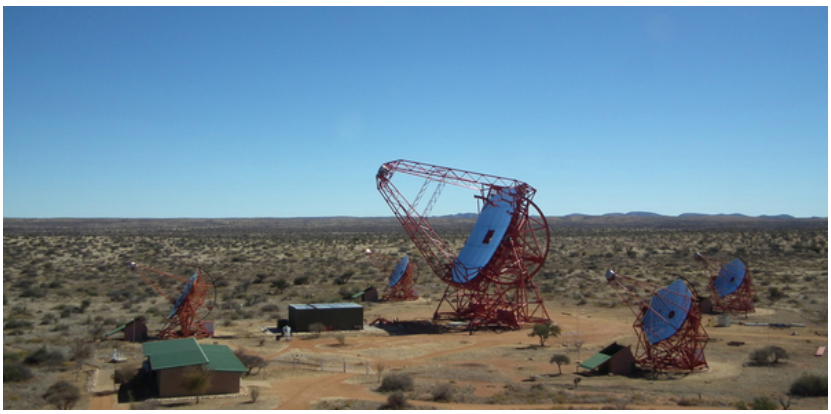

Figure 2.10: The HESS telescopes situated in Namibia. [29]

VERITAS (Very Energetic Imagin Telescope Array System) [28] is situated at the Fred Lawrence Whipple Observatory (FLWO) at Mount Hopkins, in South Arizona, USA and operates in the energy range of 50 GeV to 50 TeV. It constitutes of four 12 meters telescopes segmented in 350 hexagonal facets, with a camera with a 5^{o} in diameter and became operational in April 2007.

Figure 2.11: The FLWO basecamp and the VERITAS telescopes situated in Arizona. [28]

CTA (Cherenkov Telescope Array)is a next-generation project for very high energy (GeVs to TeVs)ground-based gamma-ray Cherenkov Telescopes which will be operative in a few years [18]. It is a collaboration of more than 1000 scientists from 28 countries. CTA will consist of two arrays of tens of telescope, situated one in the Northern Hemisphere with the main goal to observe the Extragalactic sky, and one on the the Southern Hemisphere, devoted

[1] This acronym was chosen in honour of Victor Francis Hess, an Austrian-American physicist who receive the Nobel Prize in 1936 for his discovery of cosmic rays.

to observe the central region of our Galaxy. Three different types of telescopes will be used: for the lowest energies (20 GeV- 1 TeV) a small number of Large Size Telescope (LST) will be constructed, for the 100 GeV-10 TeV energy domain 20-30 Medium Size Telescopes (MST) and tens of Small Size Telescopes (SST) in the southern hemisphere for the highest energies, from few TeVs up to hundreds of TeVs. This configuration will allow a wide energy range (from tens of GeVs to hundred of TeVs!), with a sensitivity about a factor 10 better than the current IACTs. Due to the location in both the hemispheres, the FoV will result of $\sim 10^{o}$ and an improved angular resolution of 0.1^{o}. It will open new possibilities of discovery potential in fundamental physics and astrophysics.

We will see the MAGIC in the next section.

2.4 The MAGIC Telescopes

Figure 2.12: The MAGIC telescopes situated in La Palma at the Roques de los Muchachos: MAGIC-I is on the left and MAGIC-II on the right. Picture taken before the start of the shift.

The Major Atmospheric Gamma Imaging Cherenkov Telescopes can be seen in Figure 2.12: they are situated in the Canary Island of La Palma, at the Roque de Los Muchachos, at 2235 m a.s.l. and at a longitude of $17^{o}53'33''$ and at a latitude of $28^{o}45'25''$. It constitutes of two telescopes, $\sim$ 85 meters apart, with a 17 meters diameter mirror and they operate in the energy range of 55 GeV to tens of TeV. The two telescopes, MAGIC-I and MAGIC-II, were built respectively in 2004 and in 2009 with different cameras, triggers and readout system. In 2011-2012 they underwent an upgrade program to unify and improve the telescopes performances.

2.4.1 Structure frames and reflectors

Both the reflectors have a parabolic shape and are 17 meters wide in diameter and constitutes of fragmented mirrors of squared shape in order to minimize the empty regions and to ease

the production process. MAGIC-I has 964 square mirrors of 0.45 meter side made of aluminium and MAGIC-II has 247 square mirror of 1 meter side of which 143, collocated in the central part, are made entirely of aluminium sandwich and 104 are made of glass-aluminium sandwich (see Figure 2.13). Although the reflector shape is parabolic, the mirrors have a spherical curvature which varies from 34 cm to 36.5 meters to match the overall parabolic curvature. The telescopes are equipped with an active mirror control (AMC): behind each facets there are motors controlling actuators that can move forward or backward each facet. There are two kind of actuators: single-cardanic and double-cardanic; a third leg in each facet allow a correct movement of the mirrors. These motors correct for sagging of the camera and deformations of the dish due to the varying gravitational load.

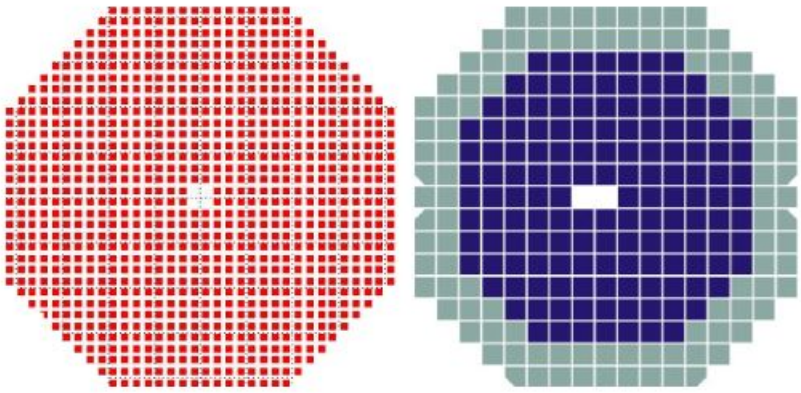

Figure 2.13: Left: MAGIC-I reflector surface, whic constitutes od 964 mirrors. Right: MAGIC-II reflector surface, constituting of 143 alluminium mirrors and 104 glas mirrors.

The optical support consists of a space-frame made of carbon fibre and steel tubes; the light material (for a total weight of the structure of less than seven tons) is necessary to allow fast movements in case of Gamma Ray Bursts. A tubular arch of aluminium support the camera which is at the focus of the reflector (i.e. at a distance of 17 meter above the reflector) and it is stabilized against oscillation by steel cables attached to the main frame. The telescopes have an alt-azimuth mount: the azimuth drive ring is 20 meters in diameter and is made from a railwail rail where the telescope can slide. For the elevation axis, sliding bearing are used. [17]

Figure 2.14: Frame of the MAGIC telescopes: the arch supports the camera, which in the picture can be seen resting on the pillar while in parking position, to lighten the load of the weight to the structure and to improve the stability of the telescope structure during impervious weather conditions as storms, strong winds and snow.

2.4.2 Camera

Figure 2.15: Camera of MAGIC-I. The picture was taken in daylight with the lids closed since the electronics were shut down.

The camera of both the telescopes has an hexagonal shapes and is protected by movable lids, which can be closed during the day, during bright nights or in case of intense light flashes. To stabilize the temperature of the camera electronics, two cooling plates are used, where cooling liquid runs. After the upgrade, both cameras have 1039 pixels of 0.1° diameter: because of the short duration of light flashes produced by air shower, extremely fast and sensitive light sensors are required so each pixel is equipped with a photomultiplier.

Every seven pixels are grouped in a hexagonal configuration to form a cluster, to allow a easier control and maintenance of the camera. Since the photocatodes of PMTs have a spherical shape, which would mean to have dead area between pixels, hexagonal light collectors are placed on top of PMTs to optimize the collection area.
Summing the counts over a certain time, a rough signal charge per channel is obtained which is then translated into number of photons on the camera plane. To convert the number of photoelectrons (phe) produced in the PMT to photons a calibration process is necessary: the relative calibration and the absolute calibration. For the firts, a calibration box situated

approximately at the center of the reflector is used . It illuminates the PMT with well-characterized light pulses of different intensity (to mimic the Cherenkov flashes of the light showers), producing phe. It is then possible to obtain the factor of conversion between number of phe produced in the photocatode and collected by the first dynode of the PMT and the measured number of ADC (Analogue to Digital) counts from the digitized signal. From here the absolute calibration is needed to convert from the number of phe produced in the first dynode and the number of incident gammas. The conversion is obtained using the PDE (Photo Detection Efficiency), which depends on the Quantum Efficiency of the PMT, which is the probability that an incident photon generates a phe, and the CE (collection efficiency) which is the probability that a phe produced in the cathod reaches the first dynode.

2.4.3 Trigger system

From the PMT, optical fibres $\sim$ 162 meters long transmit the analogue signals to the readout and the trigger electronic situated in the control house. There the readout system is responsible to sample the signal with 2 Gsamples/s; this fast sampling of the signal is required both to increase the S/N(signal over noise ratio) by reducing the total duration of the registered signal and therefore the spurious contribution of the NSB, and to keep up with the short duration of the Cherenkov light flash. This sampled signals, which will later be acquired by the DAQ [2] need to be selected so that only the events of interests are recorded. To reject background events (see Figure 2.8), a trigger is used: the most general concept of trigger is a decisional system which select the gamma events when a preset number of PMTs detect a light level above a set treshold within a short integration of time. Both the cameras have a Field of View of 3.5^o and the trigger region embrace only the inner 547 pixels for a 1.25^o radius, since the camera performance decrease as the distance from the center of the camera increases. The MAGIC trigger has four levels: Level 0, Level 1, Level 3 and the sum-trigger.

L0 trigger This trigger is the most basic one: for each pixel is possible to set a *discrimination threshold* (DT) which is automatically adjusted by the *Individual Pixel Rate Control* (IPRC). When the signal of the pixel is bigger than the DT, a digital trigger is generated.

L1 trigger The next step is based on the next-neighbour (NN) pixels: it triggers the signal when a group of NN=2,3,4,5 compact pixels received the L0 in a short window of time.

L3 trigger It is also known as stereo trigger: when events trigger both the telescopes in a tight time coincidence, the event is recorded.

Sum-trigger The signal of a group of neighbouring pixels (a macrocell) is summed and the discrimination threshold is applied to the summed signal. The structure of the macrocell can be seen in Figure 2.16: the macrocells are distributed in the trigger region and overlap each other. This trigger is expected to lower the energy threshold to 25-30 GeV. [40]

[2] Data Acquisition system

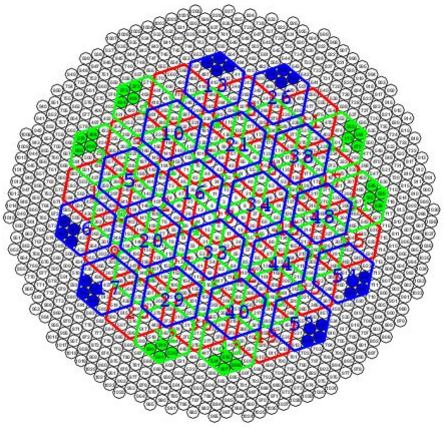

Figure 2.16: The macrocell structure of the Sum-Trigger in the camera. Through Monte Carlo simulation, it was found that 19 was the optimized number of pixels in the macrocell. The shape and the number were chosen in order to guarantee an angular symmetry and a symmetrical overlap.

If only the DT was used as a trigger, high DT would be required to reject accidentals, NSB, the after-pulse of the PMTs and muon rings. Adding other methods to rejects background events, such as the NN technique, the time coincidence in the stereo-mode observations and summing the signal of macrocells, permit to lower the DT, and as a consequence to lower the energy threshold of the telescopes.

So the calibrated files, obtained separately for each telescope, need to pass the trigger and then the Hillas parameter are calculated for each event; these files with individual image parameters are then merged into a stereo file, called Superstar, from where the energy and direction reconstruction, as well as the gamma/hadron discrimination can be performed.

Chapter 3

The Dark Matter

> Science progresses best when observations force us to alter our preconceptions.
>
> Vera Rubin

3.1 Dark Matter Evidences

There are three main historical evidences of dark matter existence, which come from the rotation curves, the gravitational lensing and its imprint on the CMB (Cosmic Microwave Background Radiation).

3.1.1 Rotation curves

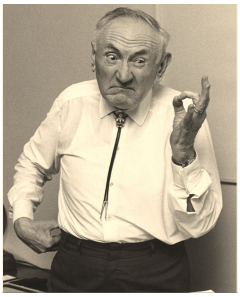

Figure 3.1: The swiss astronomer Fritz Zwicky.

In 1933 the swiss astronomer Fritz Zwicky was the first to infer the existence of *dunkel Materie*, dark matter, by studying some galaxies in the Coma Cluster: he found that the gravitational mass of this cluster (obtained by the velocity dispersions of the galaxies) was at least 400 times larger than the luminous mass. But it was not until 1970 that the astronomers Vera Rubin and Kent Ford, observing the Andromeda Galaxy, convinced the scientific community that there was more to the eye: the type of approach was the same applied by Zwicky, the only difference that he was observing galaxies in a galaxy cluster, Vera and Kent were observing the gas components in a galaxy.

By measuring the Doppler shift of the spectra produced by HII regions and assuming circular motion, they obtained the velocity dispersion rotation curve and they noticed that at large radii the velocity dispersion remained approximately constant. This did not agree with the theoretical expectations: if we consider an infinitesimal mass dm at a certain distant r from the center of the rotating galaxy, it feels both the gravitational force and the centrifugal force. If we want for this element dm neither to collapse or runaway, the sum of these two forces needs to be equal to zero (i.e. the system is virialized) , and this needs to be satisfied until a certain radius R that we define to be the radius of our galaxy. Assuming

the galaxy has a spherical shape and that the gas is on circular orbits, the gravitational force is $F_{gr} = GM(r) \times dm/r^2$ and the centrifugal force $F_{cent} = v^2(r) \times dm/r$, which gives $v(r) = \sqrt{GM(r)/r}$. So if we consider the mass as formed by only the visible matter, the mass would increase as $M(r < r_{gal}) \sim r^3$ inside the galactic disk (with radius r_{gal}) and as $M(r > r_{gal}) \sim 0$ outside of it, resulting in a rotational curve which increases linearly with the radius inside the disk (as can be seen in Figure 3.2 for radius $r \lesssim 5$kpc) and then decreases as the square root of the radius outside the disk. To explain the observed constant velocity at large radius, the existence of an "invisible" matter was needed. As can be seen in Figure 3.2, if we consider only the contribution of the disk, the observed velocity shows a discrepancy and including the gas contribution does not solve this problem. It is necessary to consider the presence of a dark matter halo.

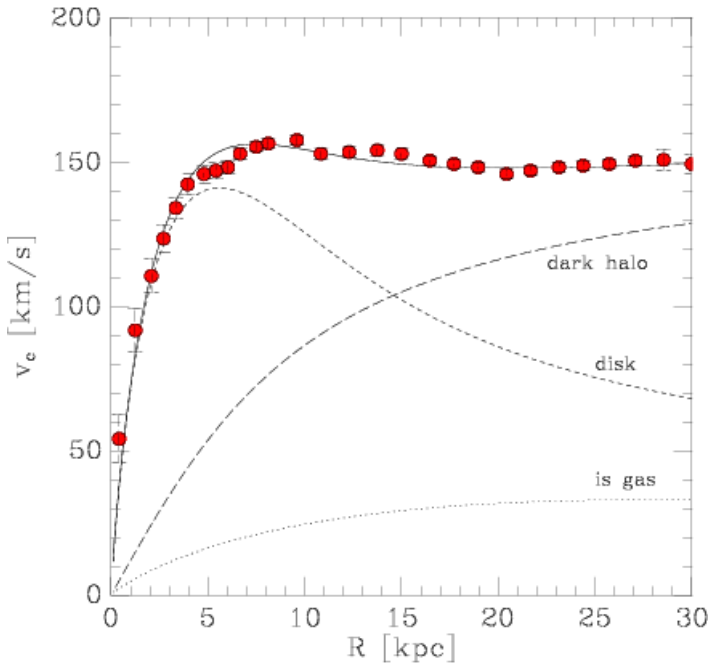

Figure 3.2: Rotation curve of NGC3198 spiral galaxy: the red dots are the actual velocity of its outer parts and the line denoted as disk are the expected velocity. A dark matter halo is necessary to substain the velocity in the outer parts. Credit: Van Albada et al.

3.1.2 Gravitational Lensing

In 1704, on the conclusion of his treatise on Optics, Newton posed some questions to inspire further search to future scientists. The first of these was the following: *Do not Bodies act upon Light at a distance, and by their actions bend its Rays, and is not this action strongest at the least distance?* It took two centuries to get an answer, and it came from Einstein's General Relativity Theory. The energy-matter density tells the space how to curve, the space answers back regarding how to move so that light travels along geodesics (the equivalent of a straight line for a free-falling object in a flat space). A light ray arriving to the Earth from far away has a high probability of passing close to a massive object, and as result it will be deflected, so that the object's shape from which it came will be distorted, and might form ring or multiple arcs. In 1919 Eddington was the first to observe this effect and in 1970

Fritz Zwicky actually predicted that also galaxy clusters might be the source of gravitational lensing.
Since dark matter interacts gravitationally, it can also behave as a gravitational lens and the "smoking gun" can be seen in the *bullet cluster*, the merging galaxy cluster 1E0657-558 which consists of two primary galaxy concentrations 0.72 Mpc away from each other. Both concentrations shows an X-ray emitting plasma and on the western side a prominent bow shock can be seen (the "bullet"), indicating that the subcluster is moving away at $\sim$ 4700 km/s from the main cluster. Since the line of sight velocity component between these two is $\sim$ 600 km/s, the cores passed through each other $\sim$ 100 Myr ago [25]. During a merger of two clusters, the X-ray emitting plasma dissipates energy because of the baryonic friction, and tends to agglomerate, in contrast with galaxies, who behave as collisionless particles. The same behaviour is not expected by DM: since it's only gravitationally interacting it is frictionless. In the absence of dark matter, the gravitational potential would trace the dominant visible X-ray plasma component. On the other hand, if the mass of the galaxies is dominated by DM, the potential would trace its component, which is expected to be spatially coincident with the collisionless galaxies. The gravitational potential is derived by studying the lensing map, which reveals a dark matter clump lying ahead of the merging clusters, and not coincident with the observed mass, as can be seen in Figure 3.3

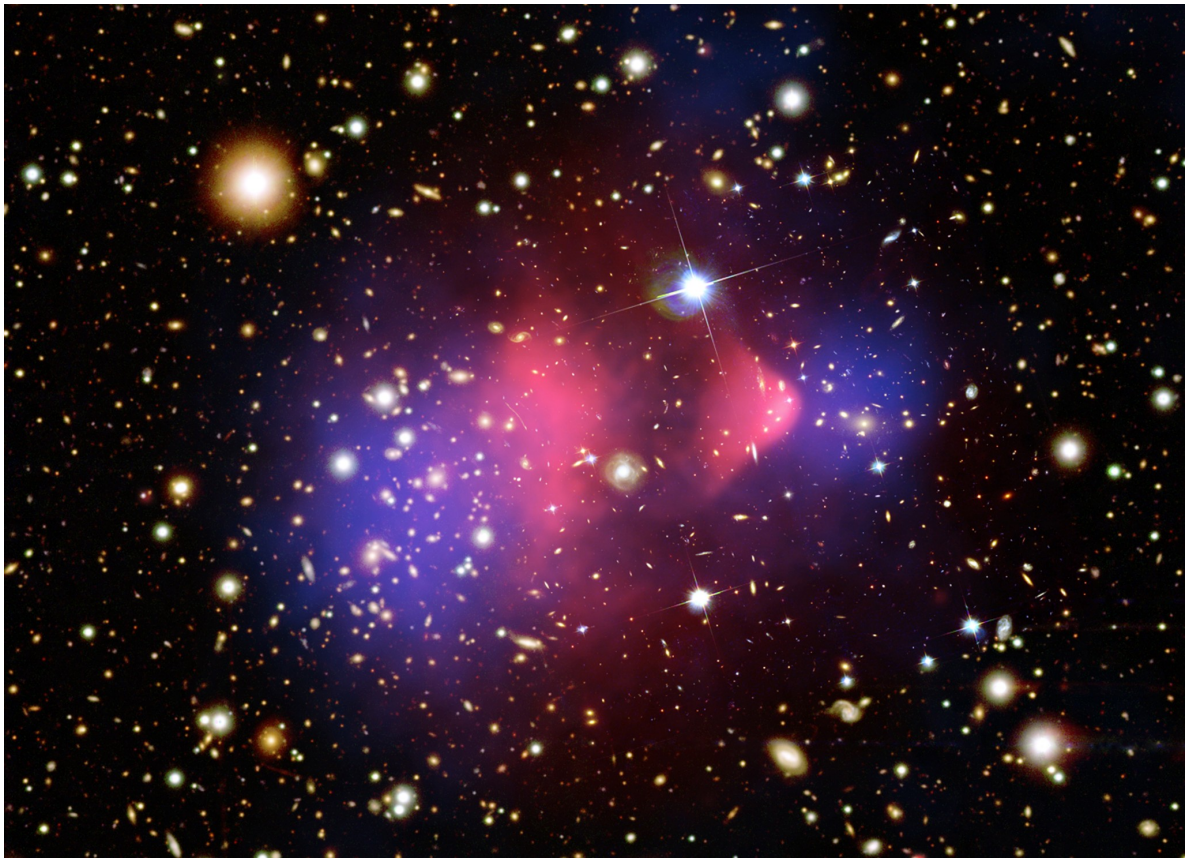

Figure 3.3: Composite image of the Bullet Cluster. The red shows the X-ray gas component, the blue shows the mass component as reconstructed from strong and weak gravitational lensing observations; the two components do not even overlap, due to the dark matter invisible component. Credit: NASA/CXC/CfA/ M.Markevitch et al.

3.1.3 Imprint on the CMB

In 1948 George Gamow predicted the existence of a Cosmic Microwave Background radiation (CMB) as proof of the Hot Big Bang Theory, but it was not until 1965 that the physicist Arno Penzias and Robert Wilson actually observed it: a perfect black body spectrum in the microwave, corresponding to a temperature of 2.7 K.
The Standard Model of Cosmology is the "concordance model" which well describes the evolution of the universe since the Big Bang and necessitating only six parameters: the scalar spectral index n_s, the curvature fluctuation amplitude Δ_R, the reionization optical depths τ_{reion}, the baryon density Ω_B, the dark matter density Ω_{DM} and the dark energy density Ω_Λ, where $\Omega_i = \rho_i/\rho_c$ is the energy density of the i component respect to ρ_c, the energy density for a flat universe with null vacuum energy density. The Cosmological Standard Model predicts that after the Big Bang, the primordial plasma (a quark-gluon plasma where due to the high temperatures all particles are relativistic) is in a situation of thermodynamic equilibrium and in a state of continuous expansion; in order for the various particles to stay in equilibrium with this fluid, their rate of interaction Γ_i must be greater than the expansion rate of the universe, which corresponds to the Hubble parameter at that epoch H. While the universe expands, its temperature cools down, making it more difficult for some reactions to occur which decreases the interaction rate, resulting in $\Gamma_i < H$ and so the the i-particles decouple (or freeze out) from the fluid and do not efficiently interact with it any more.. At $E \sim 0.26$ eV , the *re combination* era, the electrons survived to annihilation begin to recombine with atom nuclei (mostly protons and α particles); as a result the rate of interactions of radiation and matter decreases, becoming smaller than the rate of expansion of the universe: photons starts travelling freely through space from the last surface scattering. This is why the CMB has a perfect black body spectrum and it brings to us the precious information of the last interactions between matter and photons. The CMB, though, shows intrinsic temperature anisotropies in its angular distribution, which can be described using a power spectrum, which can be seen in Figure 3.4. Its peaks (called acoustic peaks)are caused by the collapse of density fluctuations of barions, photons and dark matter, so that from the position and the width of the peaks the amount of barionic and dark matter can be measured.

More in general, by making accurate measurement of the CMB fluctuations, it is possible to measure the six free parameters of the Standard Cosmological model; the values obtained from the latest Planck analysis are these [6]:

- $\Omega_B h^2 = 0.02222 \pm 0.00023$
- $\Omega_{DM} h^2 = 0.1197 \pm 0.0022$

where $h = H_0/100\mathrm{km\,s^{-1}\,Mpc^{-1}}$ and H_0 is the Hubble parameter and its value measured by Plack $H_0 = 67.31 \pm 0.96$

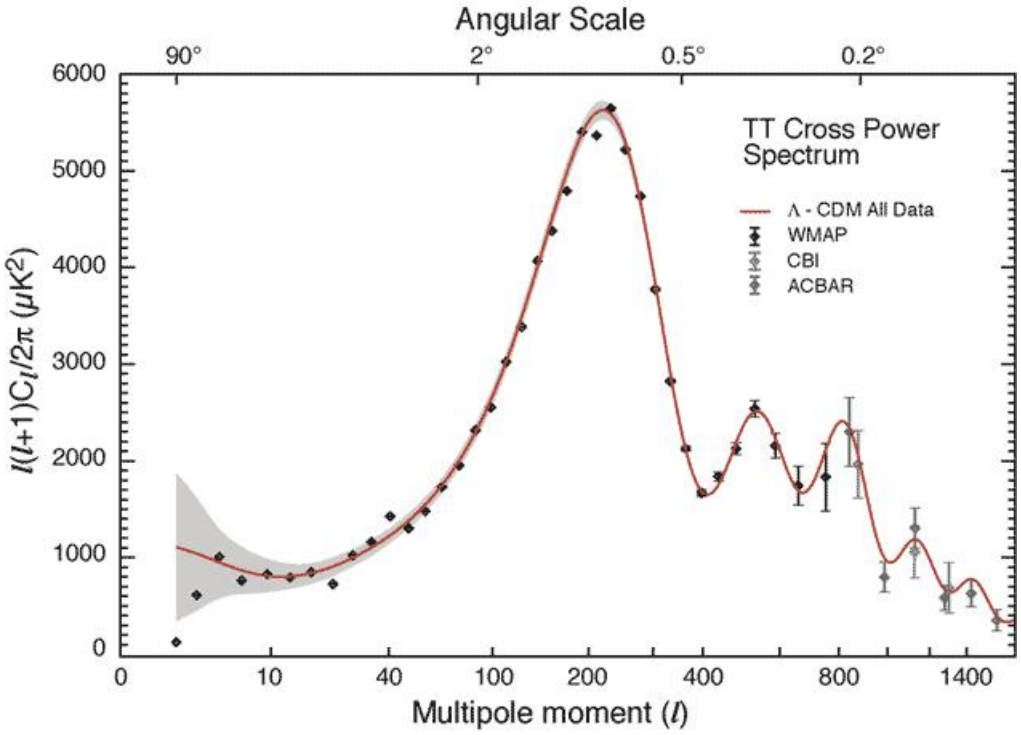

Figure 3.4: The power spectrum of the CMB. The Multipole moment l is proportionally inverse to θ, the polar angle i.e. the angular scale; on the y axis there is the power spectrum, which is the quadratic average of the coefficients of the harmonic spheric decomposition of the temperature fluctuations. Credit:NASA/WMAP Science Team

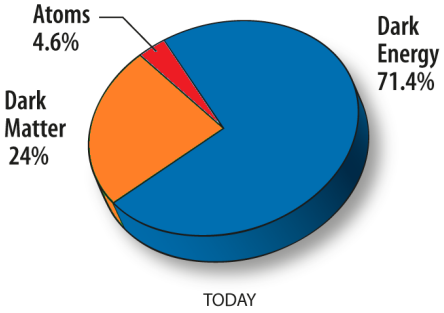

So today barionic matter constitutes 4.6% of the universe, while dark matter is almost one fourth of the universe composition and the rest 71.4% is given by Dark Energy.

3.2 Dark Matter candidates

Let's now follow Ariadna's ball of thread in the Minothaur's labyrinth: what we can infer about dark matter from observations is not much but it's crucial. Since dark matter interacts gravitationally and through the weak interaction, is stable on the cosmological time scale and not charged (not colour charge nor electromagnetic charge), also the dark matter particle candidate (which from now on we will indicate with the χ appendix) need to satisfy these properties. Other restrains are obtained by the imprint on the CMB (as described in the previous paragraph), which requires $\Omega_\chi \sim 0.24$ and from the observations of the Large Scale Structures. A particle is defined either as "hot" or "cold" depending on its velocity during the freeze-out from the thermal background: if it's a relativistic particle it's referred as a "hot" particle , otherwise it's a "cold" particle, so we can have either a hot dark matter (HDM)

with temperature in the order of TeVs or a cold dark matter component (CDM) with temperature in the order of eVs); warm dark matter (WDM) is in between the HDM and the CDM with temperature in the order of GeVs. After the decoupling of the photons, the pressure they provided is missing so due to the fluctuations in density the first structures started to aggregate, but how they aggregated depends on the velocity of dark matter. In case of hot dark matter, since the particle is relativistic, it would kill the density fluctuations on scale smaller than super clusters. Only when it becomes non relativistic the matter aggregation can begin, following a "top-down" process, with structures on the scale of clusters forming first in flat pancake-like sheets and later by their fragmentations and instabilities also smaller scale structures as galaxies could begin to form.

This so called "pancake" non linear collapse has some frictions, the main being that simulations and studied predicted supercluster collapse to occur recently ($z < 2$); however from studies of stellar population and globular cluster, the formation of galaxy set the limits at $z \sim 3$ [62]. This end up ruling out the hot dark matter hypothesis.

In case of cold dark matter, since the particle is not relativistic, the small scale density fluctuations are not dumped and structures began forming hierarchically ("bottom up" process), with small scale structures forming first and then, by the process of clustering, began to assemble into larger scale systems. This is the process which led to the formation of dark matter halos; these then attracted the barionic matter which, collapsing, lost energy through dissipative processes leading to formations of stars an gas clouds. This *hierarchical clustering* well describes both the Large Scale Structure we observe and the CMB density fluctuations. The difference of the Large Scale Structure predicted with HDM, WDM and CDM can be seen in Figure 3.5. Of course the dark matter component can be a multi component, a mixture of hot, cold and warm dark matter.

Amongst the Standard Model particles, only the neutrino is not charged, stable and has mass, but since it was relativistic when it freezed out, it is ruled out as the only component of dark matter, but it still might contribute in a multi component scenario. A possible candidate is the axion, a light particle introduced in the Standard Model to justify the CP (charge conjugation and parity) violation problem. It is expected to be extremely weakly interacting, meaning that they were not in thermal equilibrium at the Early Universe. From laboratory searches, luminosity function of white dwarves and the dynamic of supernova 1987A axion mass seem to be very small ($\lesssim 10^{-3}$eV [64]). Since the production mechanism of axions is still unknown, the calculation of its relic density is still uncertain, but it is possible to find a certain range for which the axion satisfy the requirement to be a dark matter candidate.
Another class of candidate are the WIMPs, Weakly Interacting Massive Particles. Since they're stable their interaction rate is only defined by annihilation, the Ω_χ; supposing that their mass is in the 100 GeV range and that the decoupling temperature $T_D \sim 1/20\, m_\chi$, the Ω_χ obtained by calculation corresponds to the one extrapolated by CMB observations: this is the first success of the WIMPs. They also predict a thermally averaged velocity cross section $< \sigma v >$ of $3 \times 10^{-26}\,\mathrm{cm^3 s^{-1}}$.
To find WIMPs it is necessary to extend the Standard Model beyond a new physics. In the Standard Model there is a fundamental division amongst particles: while gauge bosons mediate the interactions, fermions are the constituent of matter. So a natural question arise concerning whether a symmetry connecting interactions and matter exists. Answering this

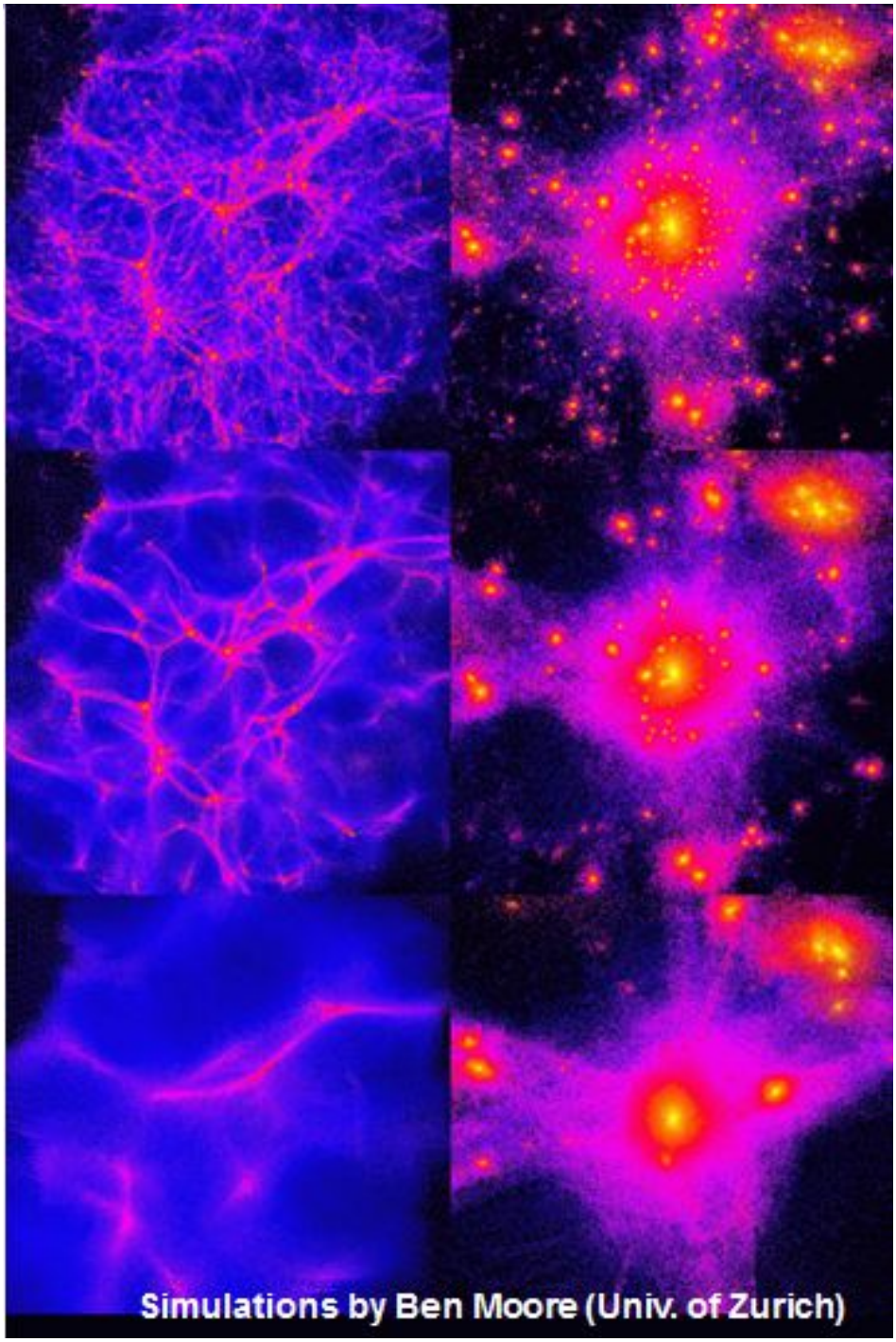

Figure 3.5: From the top simulations of Cold Dark Matter (WIMPs), Warm Dark Matter (mostly CDM with some neutrinos as well) and Hot Dark Matter (neutrinos). Small scale structures are predominant in the CDM scenario and lacks in the HDM scenario. Credit Ben Moore, University of Zurich.

question is SUSY (SUperSYmmetry), a theory of particle physics which proposes a new symmetry: every fermion of the Standard Model has a boson supersymmetric particle (superpartner)and viceversa. The superpartners also have the same quantum numbers (except

for the spin) and the same mass of the Standard Model particles, but since we didn't find as many particle as sparticles, SUSY must be a broken symmetry.
A possible SUSY model is the Minimal Supersymmetric Standard Model (MSSM), minimal because it contains the smallest number of fields to obtain all the fields of the Standard Model. As a result, the superpartner of fermions (i.e quarks and leptons) are boson particles (*squarks* and *sleptons*). Similarly the fermion superpartners of the gauge fields, gluons, $W^{\pm}$ and B, are *gluinos* $\tilde{g}$, *winos* $\tilde{W}^i$ and *binos* $\tilde{B}$. Also another Higgs field has been introduced and their superpartners are spin 1/2 *Higgsino* 3.6. Another symmetry is also introduced, the R-parity, with all Standard Model particles have $R = +1$ and their superpartners have $R = -1$. As a consequence, no sparticle can decay in particles without including also an odd number of sparticles as decay product. Thanks to this symmetry, the lightest supersymmetric particle (LSP) is stable, and can only annihilate, becoming a perfect WIMP candidate.

Standard Model particles and fields		Supersymmetric partners			
		Interaction eigenstates		Mass eigenstates	
Symbol	Name	Symbol	Name	Symbol	Name
$q = d, c, b, u, s, t$	quark	$\tilde{q}_L$, $\tilde{q}_R$	squark	$\tilde{q}_1$, $\tilde{q}_2$	squark
$l = e, \mu, \tau$	lepton	$\tilde{l}_L$, $\tilde{l}_R$	slepton	$\tilde{l}_1$, $\tilde{l}_2$	slepton
$\nu = \nu_e, \nu_\mu, \nu_\tau$	neutrino	$\tilde{\nu}$	sneutrino	$\tilde{\nu}$	sneutrino
g	gluon	$\tilde{g}$	gluino	$\tilde{g}$	gluino
$W^{\pm}$	W-boson	$\tilde{W}^{\pm}$	wino	$\tilde{\chi}^{\pm}_{1,2}$	chargino
H^-	Higgs boson	$\tilde{H}^-_1$	higgsino		
H^+	Higgs boson	$\tilde{H}^+_2$	higgsino		
B	B-field	$\tilde{B}$	bino	$\tilde{\chi}^0_{1,2,3,4}$	neutralino
W^3	W^3-field	$\tilde{W}^3$	wino		
H^0_1	Higgs boson	$\tilde{H}^0_1$	higgsino		
H^0_2	Higgs boson	$\tilde{H}^0_2$	higgsino		
H^0_3	Higgs boson				

Figure 3.6: The particles and relative sparticles Zoo. [15]

Amongst the possible LSP candidate in the MSSM model there are sneutrinos, gravitinos, axinos and neutralinos, which are the lightest mass eigenstate of the matrix which mix binos, winos and higgsinos. Sneutrino is ruled out because its theoretical cross section with nuclei is much larger than the limits found by dark matter experiments. Gravitinos and axinos can not be excluded a priori, but they exist only in a subset of supersymmetric scenario and because of their very weak interactions, would be difficult to detect. Therefore neutralinos remains the best dark matter candidate.
The problem with MSSM is that it requires 124 free parameters, so various approach have been developed to solve it. Historically the first idea was to use specific mechanism for SUSY breaking to reduce the number of parameters; an example is mSUGRA (minimal SUper GRAvity) which assumes that Supersymmetry is broken by gravity and that some of the MSSM parameters obey a set of boundary conditions at the Grand Unification scale. Such approach are somehow phenomenologically limiting and some of them are at discrepancy with the experimental data as a result of insufficient parameter freedom.
Another possible approach is the pMSSM (phenomenological MSSM) which makes use of the esperimental constrains to obtain 19 free parameters (or 20 if as possible role for LSP we also consider the gravitino, which is the spartner of graviton, the hypothetical particle which mediates the force of gravitation in the quantum field theory framework). The 19 parameters are the ten sfermion mass, three gaugino masses, three trilinear couplings and

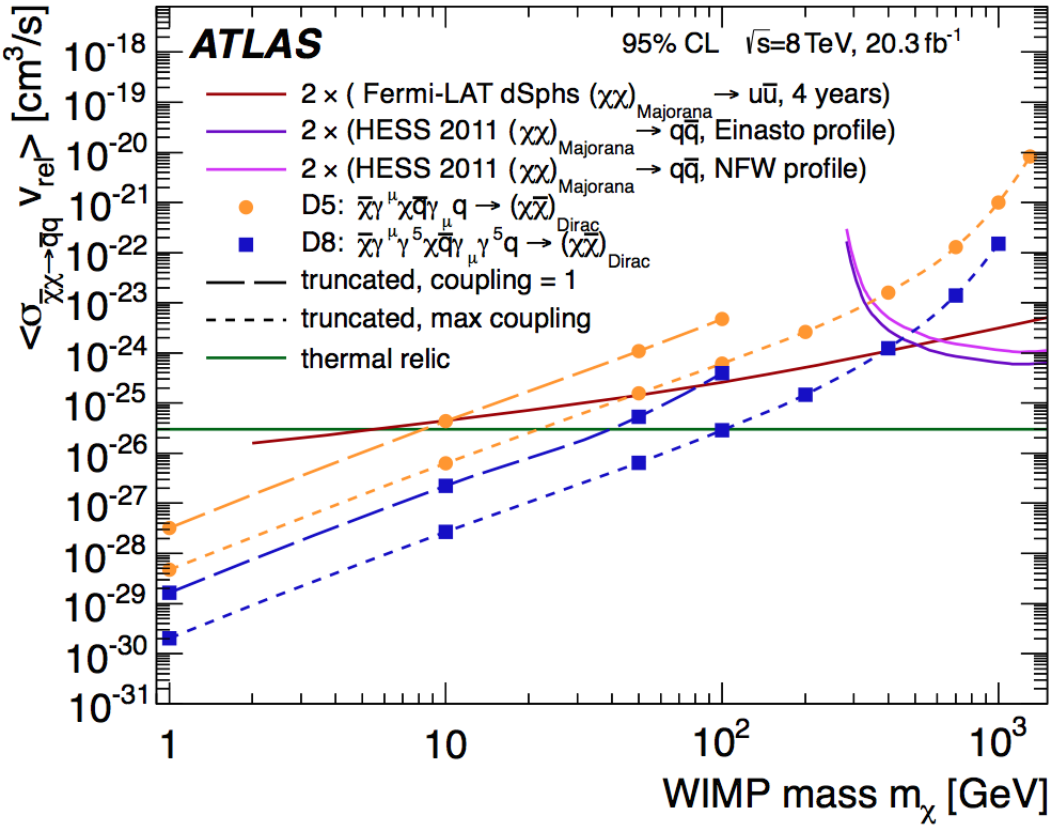

Figure 3.7: The graphic shows upper limits for WIMP annihilation cross section as a function of the WIMP mass as obtained from the ATLAS monojet analysis. The interaction between WIMPs and SM particles is described as a contact interaction with and effective field theory: the interaction is mediated by a single new heavy particle (or particles) with mass too large to be produced at LHC. D5 corresponds to an effective field theory where the WIMP is a Dirac particle interacting through a massive spin-1 vector particle. D8 corresponds to an axial-vector interaction. The thermal relic poses an upper limit, so that for instance in the D5 max coupling scenario the maximum mass allowed is of $\sim 11\,GeV$. In the graph there are also illustrated the astrophysical searches for WIMP annihilation as obtained by HESS and FERMI-LAT. [2]

three Higgs/Higgsino parameters. The most recent results regarding the neutralino are from the ATLAS (A Toroidal LHC ApparatuS) experiment at the Large Hadron Collider at CERN. It accelerates and collides protons with energies in the centre of mass ($\sqrt{s}$) of 7, 8 and 14 TeV; after the collision two jets are formed. Two LSP are at the end of the decay chains and can be "seen" as missing transverse energy. The results of the first LHC run (2010-2012) can be seen in Figure 3.7.

3.3 Dark Matter Annihilation spectrum

The products resulting from dark matter annihilation are strongly model dependent: typical channels are annihilation into quark-antiquark pairs, gauge and Higgs bosons ($W^{\pm}$, Z, H) and charged leptons (e^+e^-, $\mu^+\mu^-$, $\tau^+\tau^-$). The hadronization and decay of these particles produce in general only three type of emissions: γ-ray photons, high energy neutrinos and relativistic electrons and protons with their respective antiparticle. Also primary low energy

photons can be produced from the interaction of these relativistic electrons with the magnetic field through synchrotron radiation, with insterstellar material through bremsstrahlung and with the stellar radiation fields and CMB through inverse Compton scattering.

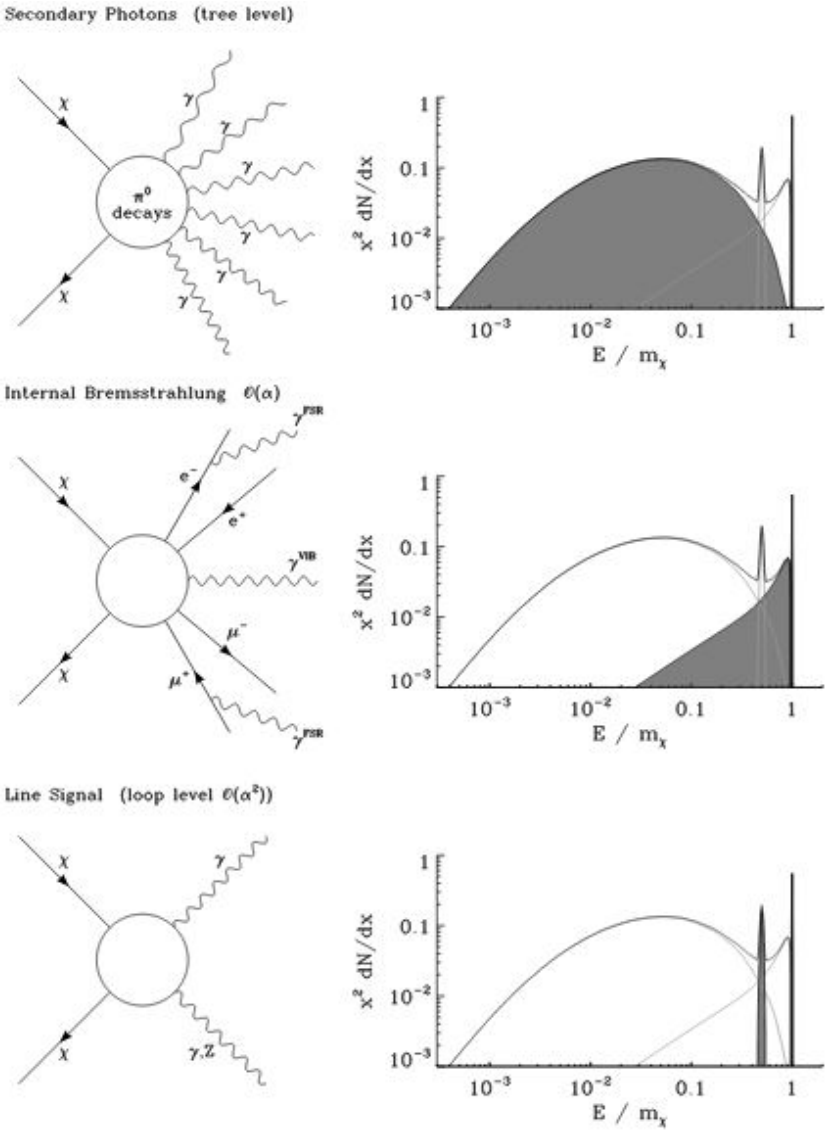

Figure 3.8: The three different sources and energy distribution of γrays production by WIMP annihilation. On the top, the primary photons production mechanism ; in the middle internal bremsstrahlung photons production mechanism : photons can be produced either from virtual internal bremsstrahlung (VIB) or from final state radiation from external legs (FSR). On the bottom, the production of mono energetic photons. [51]

Since γrays have likely a stronger signal from Galactic DM structures, we will focus on them; they can be produced in three different ways: from line signals, from internal bremsstrahlung and from primary photons, as can be seen in Figure 3.8 [66]. The line signal derives from mono-energetic photons produced in final states such as $\gamma\gamma$, γH or γZ, but since DM is neutral, there is no direct coupling to photons and γrays are a result of loop-level diagrams and so they are loop suppressed ($\mathcal{O}(\alpha^2)$) and are expected to produce far fewer events, for which reason they can not be easily detected. Internal Bremsstrahlung (internal as it does not require an external electromagnetic field) is present every time dark matter annihilate into charged final states at $\mathcal{O}(\alpha)$. Its spectrum has its peak at $E \sim m_\chi$ and shows a sharp cut off. Primary photons comes as products of "jets". In MSSM neutralinos dominantly annihilate to hevy fermions $b\bar{b}$, $t\bar{t}$, $\tau^+\tau^-$ or bosons; then along the cascade mesons are generated (especially π^0 which then decay into $\gamma\gamma$). In this way WIMP annihilation can produce several tens of γ-rays and the result is a broad spectrum with a cut off around m_χ.

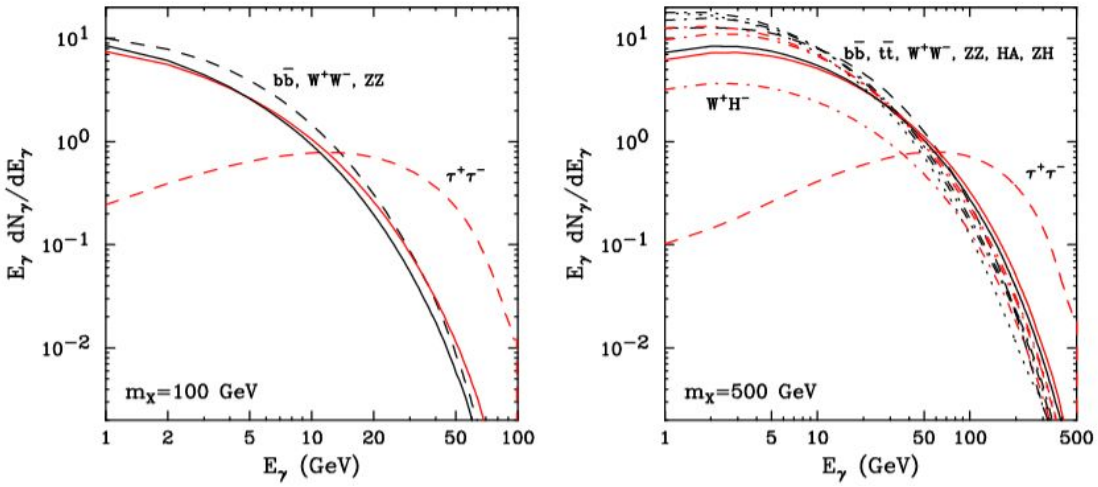

Figure 3.9: On the left, the annihilation spectra for a 100 GeV WIMP, on the right for a 500 GeV WIMP, for different annihilation modes. [66]

As can be seen in Figure 3.9, these annihilation modes give degenerate photon spectra, except for the $\tau^+\tau^-$ channel, which shows a harder spectrum.

3.4 Dark matter annihilation flux

The probability for two dark matter particles to annihilate depends on to the thermal averaged annihilation cross section times the relative velocity $< \sigma v >$ and on the local particle dark matter number density $n_\chi^2 = (\rho_D M/m_\chi)^2$, so dark matter annihilation processes are predicted to occur in regions with a large dark matter density, and this is why we look at the Galactic Center (see the following chapter). The observed flux of γ-rays will depend on the probability (where the dark matter density squared will have to be integrated along the line of sight connecting the GC to the observer), on the spectrum of the secondary particles (for us photons) produced dN_γ and on the solid angle Ω around the direction of the galactic center. Thus the observed flux from a solid angle $\Delta\Omega$ for a given energy can be written as

$$\frac{\mathrm{d}\Phi_\gamma(,\mathrm{E},\Delta\Omega)}{\mathrm{dE}} = \frac{<\sigma v>}{2m_\chi^2}\frac{dN_\gamma}{dE}\frac{1}{4\pi}\int_{\Delta\Omega}\mathrm{d}\Omega\int_{\text{line of sight}}\rho^2_{\mathrm{DM}}(\mathrm{s},\Omega)\,\mathrm{ds} \tag{3.1}$$

Chapter 4

The Galactic Center

> Results! Why, man, I have gotten a lot of results. I know several thousand things that won't work.
>
> Thomas Edison

4.1 The Milky Way

For millennia, people all over the world had marvelled at the hazy luminous strip in the night sky that we called the Milky Way and still now we marvell at it, just looking through the "ocular" of telescopes, thanks to which we aquired more knowledge. Nowadays our galaxy is known to be a spiral barred galaxy; it is structured as a disk (containing the spiral arms), the halo and the central bulge.
The disk contains most of the stars and the dust; in its four spiral arms the star formation rate has its peak [71] , so that the disk contains most of young stars (blue stars). The disk is surrounded by a spherical halo of old stars, globular clusters which in turn is thought to be embedded into a dark matter component. Towards the center there is the bulge, from where the flat long bar extends with dimensions $7.8\,\mathrm{kpc} \times 1.2\,\mathrm{kpc} \times 0.2\,\mathrm{kpc}$. [54]. In the bulge the population of the stars consists mostly of old red stars.

4.2 Morphology of the Galactic Center

Our Sun is located $\sim 8\,\mathrm{kpc}$ away from the center of our galaxy, in the disk region. Due to this location, when looking towards the Galactic Center our line of sight intercedes the highly dense Galactic dust of the disk region, therefore most visible light coming from the Galactic Center is absorbed by this dust. Because of this interstellar extinction, only observations in radio, infrared, X-rays and γ-rays are possible.

The central region ($\sim 500\,\mathrm{pc}$) contains a complicate morphology with a variety of strong radio sources, as can be seen in figure 4.1: photon and matter fields interact with each other and the emission is mostly dominated by non-thermal synchrotron radiation due to the presence of accelerated electrons up to energies possibly of few TeVs. There are many

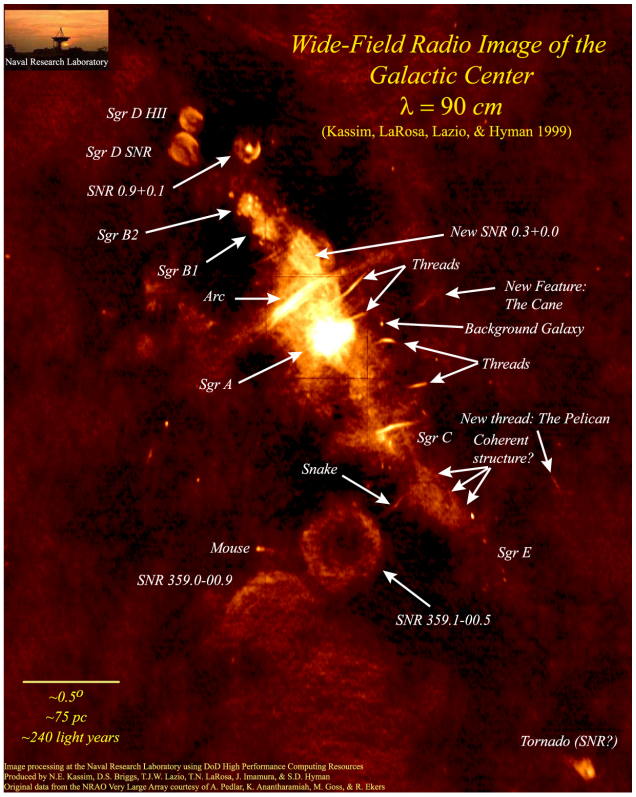

Figure 4.1: Radio image of the GC from the VLA at $\lambda = 90cm$. Around the SgrA complex lay many giant molecular clouds as SgrB1, SgrB2 and SgrC. See the text for further details. [48]

Supernovae Remnants, and at least inside the Supernova Remnants G 0.9+0.1 also a Pulsar Wind Nebula is clearly visible; the regions Sgr B1, Sgr B2, Sgr C and Sgr D contains large concentrations of ionised molecular material, with densities up to more than $10^4 \mathrm{gr/cm}^{-3}$. Also an "arc" feature is visible, which consists of linear, parallel filaments [76] and extensive "threads", both oriented perpendicularly to the Galactic plane and exhibiting highly polarised radio emission with no line emission. This emission concentrated along the Galactic plane, extended about 300 pc in Galactic longitude, is known as the Central Molecular Zone. At the center of it there is the Sagittarius A complex, the dynamic center of the Milky Way Galaxy. This last one consists of three main structures, as can be seen in Figure 4.2, which are the SgrA East, the SgrA West, the PWN G359.95-0.04 and the SgrA*.

The Eastern and the Western regions distinguish themselves because of the characteristics of the emission.The SgrA West shows a three-arm spiral structure (as seen from the Earth) and this is why is dubbed is "Minispiral". It is composed of ionised and atomic gas and dust with temperatures ranging from 100 K(in the dust component) to 10^4 K (in the plasma component). The minispiral exhibits a thermal radio spectrum, rotates around the GC and is thought to be connected with the circumnuclear disk of molecular gas. [52]. SgrA East is a shell-like non thermal structure, emitting mainly in X-rays and radio (due to synchrotron radiation from relativistic electrons) and possibly embedding SgrA West and SgrA*. Because of the type of emission, SgrA East is thought to be the remnant of an explosion of a supernova (a Supernova Remnant) which happened about 10.000 years ago. Through the spectral

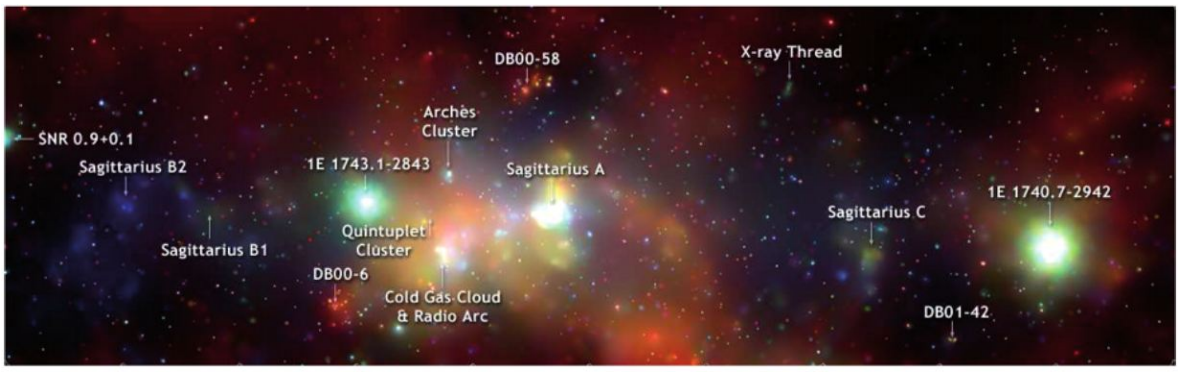

Figure 4.2: Chandra X-ray map in Galactic coordinates of a $2^o \times 0.8^o$ region around the GC. The emission of the keV photons (red: 1-3 keV, green: 3-5 keV, blue: 5-8 keV) traces extended regions where relativistic electrons produce Bremsstrahlung or synchrotron radiation and high energy phenomena of the start and end of stellar life, as particles acceleration by stellar wind shocks or by intense magnetic fields of pulsars. Credit: [72].

analysis, an over abundance of heavy elements is observed, suggesting a supernova type II explosion, whose progenitor star had a main-sequence mass of $13 - 20\, M_\odot$ [55]. This hypothesis is corroborated by the observation of an off-set and point like X-ray source, which is thought to be the neutron star left from the supernova explosion.
In 2004 three X-rays threads filaments associated with non-thermal highly polarized radio filaments were detected [74]. The radio emission is connected with synchrotron radiation of relativistic electrons and positrons and if the X-ray emission is also produced by synchrotron acceleration, it must be produced by particles accelerated in situ: a possible origin of these particles is a Pulsar Wind Nebula, denominated PWN G359.95-0.04. It is separated from SgrA* by only 8.7 arcseconds, which corresponds to a projected separation of 0.32 pc. It shows a cometary shape, a luminosity of $10^{34}\mathrm{erg\,s^{-1}}$ in the 2-10 keV band and hard non-thermal X-ray spectrum which gradually softens when going away from the head of the comet, where the pulsar is believed to be located. This shape of the spectrum is an indication that the non-thermal electrons are cooled by synchrotron radiation.
SgrA* is a compact radio source which was discovered in 1974 by Bruce Balick and Robert Brown using the Green Bank radio link interferometer operated by the National Radio Astronomy Observatory [44] and since then there was the hypothesis that it was linked to a supermassive black hole. This hypothesis is corroborated by the observations of the proper motions of stars close ($< 0.3\,\mathrm{pc}$) to SgrA* [34]. By these observations it was found there is a $\sim 10^6\, M_\odot$ dark mass core located within $< 0.015\,\mathrm{pc}$ of SgrA*. It is relatively bright at radio frequencies and a faint emitter in X-rays, and there is a parsec scale jet originating from SgrA*. The supermassive black hole in Sagittarius A* experienced periods of higher activity in the past, whose effects are observed in the molecular material surrounding it. However the reconstruction of its light curve is difficult because the clouds distribution along the line of view is not well constrained. The emission from these molecular clouds is produced by Compton scattering and photo-ionization of neutral iron atoms, caused by an intense x-ray radiation from putative past flares [24]. Its relative quiescent state might have been caused by the shock of the SNR about 10,000 years ago: this shock compressed the dust, sweeping it over the black hole and leaving no material nowadays for accretion. [55] [24].

4.3 The G2 Gas Cloud

In 2012 Gillessen et al. [41], thanks to the VLT instrument, discovered a gas cloud moving on a highly eccentric orbit toward the galactic center. This cloud of $\sim 3\ M_\odot$ consists of dense, dusty and ionized gas, with a dust temperature of 550 K and a gas temperature of order 10^4 K, relatively cold compared to the diffuse $10^8\ K$ central galactic gas. [19]. They predicted a pericenter passage in September 2013 (which actually happened some months later) at 2000 R_s, $\simeq 6$ pc distance from the black hole [42]. As G2 feels more and more the gravitational potential of the BH, it develops a cometary bubble, which becomes increasingly elongated as it approaches the pericenter because of the tidal forces. These were supposed to tear apart the cloud and disperse it along its orbit, feeding some of this material into the black hole and causing a sudden flaring, and a predicted possible emission of gamma-rays. Another effect of G2 moving towards the black hole at a supersonic speed, is that it drives a bow shock into the interstellar medium, whose electrons, crossing this bow shock, are accelerated and emit synchrotron radiation.
This event was of course of big interest, since it constituted a free laboratory to study interactions between a gas cloud and a black hole close by. Many expectations developed around this event, but few if any did actually happen: the spectrum of SgrA* from radio to submillimiter wavelengths remained remarkably stable, showing no affection for the "flirty" approach of G2 [16]. This can be used to obtain some constrains regarding the properties of this gas cloud: two hypothesis were developed. G2 could be a pressure-confined, non-self-gravitating gas cloud [41]. Alternatively, G2 could contain a very faint stellar core that loses gas as it falls towards SgrA* [14]. In the cloud model the radio flux of the forward shock is predicted to be much larger than the quiescent radio flux of SgrA* and therefore should already have been detected. In the other scenario, the radio flux lies well below the quiescent radio flux of SgrA* and will be difficult to detect [31], as can be seen in figure 4.3.

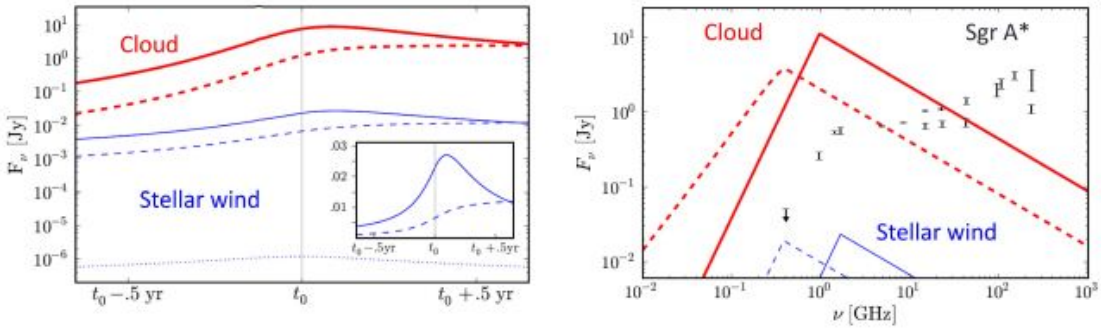

Figure 4.3: Cloud model and shocked stellar wind model for the G2 cloud. The red lines are for the cloud model, the blue lines are for a shocked stellar wind. The flux is calculated at 1.4 GHz around pericenter passage of the forward shock t_0) On the right the data points are radio fluxes measured during period of inactivity of SgrA* [31].

Recently NASA declared another discovery [58]. On Sept. 14, 2013, NASA's scientists detected an X-ray flare from Sgr A* 400 times brighter than its usual, quiet state. But since astronomers estimated that G2 was closest to the black hole in the spring of 2014, this flare was about a hundred times closer to the black hole, making it unlikely related to G2. There are two main theories to explain such big eruption: the first is that an asteroid came too close to the BH and was torn apart by gravity, becoming very hot and emitting energy in X-rays. The second theory is that the magnetic field lines of G2 could be tightly packed and

become tangled, and may occasionally reconfigure themselves and produce a bright outburst of X-rays.

On March 26th, 2015 VLT observations confirmed that G2 had survived its closest approach to the black hole, and is actually a compact object [35], as can be seen in figure 4.4.

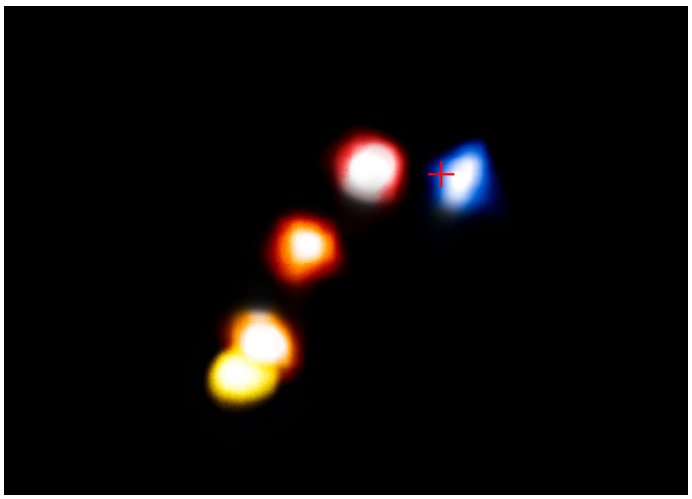

Figure 4.4: Images from infrared light coming from glowing hydrogen of the G2's orbit.The different colours indicate the motion of the cloud, red is receding and blue approaching. The cross marks the position of the supermassive black hole. Credit: ESO/A. Eckart

For sure all these mysteries behind this gas cloud are of great interest, but still not the main concern of this thesis, for which reason we'll have to leave this discussion in the good hands of Christian Fruck and thus we continue discussing other aspects of the GC. We have to remember though that the observation of the G2 is the main reason for which we have these MAGIC data of the Galactic center to analyse.

4.4 The Fermi Bubbles

In 2010 the Fermi-LAT gamma-ray satellite instrument made a discovery: a pair of gigantic gamma-ray emission regions, the so called Fermi bubbles [67]. These lobes are shaped symmetrically above and below the Galactic Center, extending till $|55^o|$ in Galactic latitude($\sim 8\,\mathrm{kpc}$) and are $\sim 40^o$ wide in Galactic longitude. They were reported to have a hard spectrum, which scale as E^{-2} between 1 GeV and 100 GeV, well defined edges and without significant spatial variation in the spectrum or gamma-ray intensity between the north and the south lobes and within the bubbles [5]. The origin of the Fermi Bubbles is unknown, but most likely they were created by large energy injection in the GC , such as a starburst activity in the last 10 Myr or a past flaring events of the central massive black hole. [67].
The discovery of the Fermi lobes was made because Fermi scientists were looking for a gamma-ray counterpart to the Wilkinson Microwave Anisotropy Probe (WMAP)haze, which is the residual microwave emission around the Galactic Center that remains after subtracting synchrotron, free-free, thermal dust, and cosmic microwave background components from the WMAP data. The bubbles are spatially correlated with the WMAP haze and their edges also line up with feature in the ROSAT X-ray maps at 1.5-2 KeV [67], as can be seen in figure 4.5.

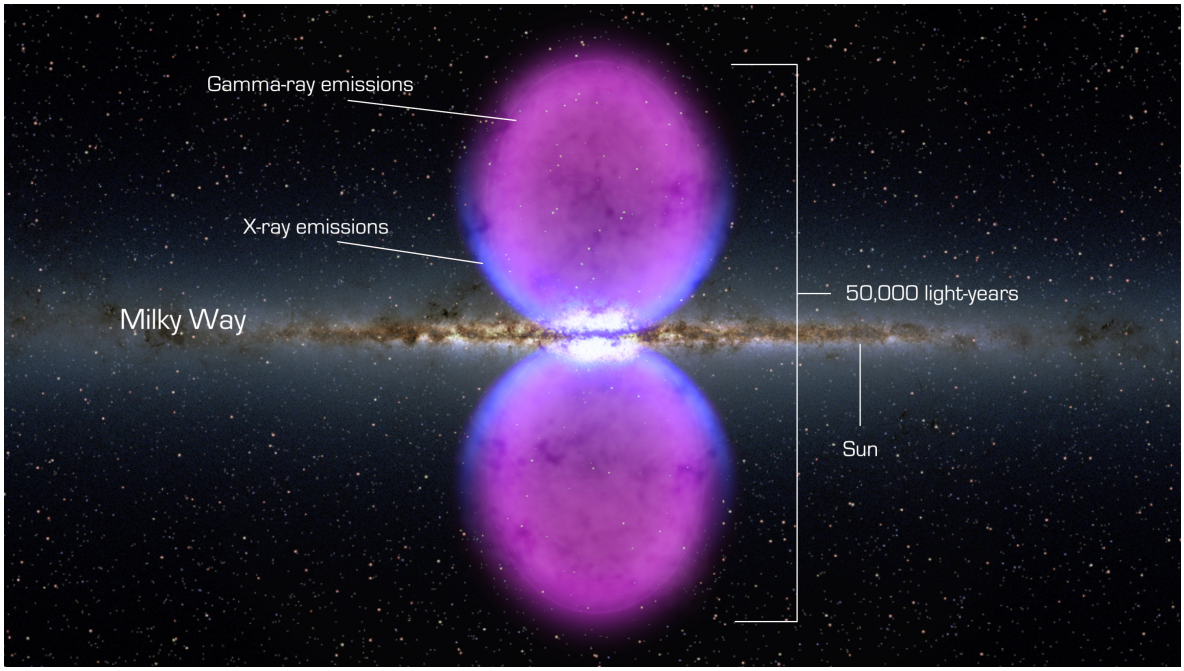

Figure 4.5: Fermi Bubbles' image. Hints of their existence were first observed in X-rays (blue) by ROSAT, a German-led mission operating in the 1990s. The gamma rays mapped by Fermi (magenta) extend much further from the galaxy's plane.Credit: NASA's Goddard Space Flight Center.

The Fermi Bubbles also associate with two giant polarised radio lobes discovered by S-PASS survey, which extend up to $\sim |60^o|$ Galactic latitude. All these three different type of non-thermal phenomena might be explained if the bubbles contain, at the height of some kpc above the nucleus, giant reverse internal shocks, whose signatures are found both in the north and south lobes [30]. Under this assumption, also the existence of a freely-expanding nuclear outflows is required (energetically matched by GC star formation), which equilibrates the thermal pressure of the shocked plasma. These shocks reheat and reaccelerate the thermal-equilibrium plasma and the cosmic rays of the nuclear outflows; the reaccelerated electrons emit synchrotron radiation, which well explains the spectrum, vertical extent and morphology of the S-PASS Lobes and of the WMAP haze. Downstream the shocks piles up, forming a shell which corresponds to the Bubble's edges and which condenses into filaments and dense clumps and then forms a fountain which flows back to the Galactic plane. On the other hand, the reaccelerated hadrons, escaping the shocks, are adiabatically compressed inside this shell and collide with the denser gas, explaining in such a way the γ-ray emission of the Fermi Bubbles.

4.5 Dark Matter halo

The dark matter halo is a component of a galaxy which extends well beyond the gas disk and whose presence is assumed observing indirectly its gravitational effect. The dark matter halo in our galaxy seems to have the shape of an oblate spheroid extending to $\sim 50\,\mathrm{kpc}$ and maybe more, with a mass $\sim 10^{12}\,M_\odot$, more than 90% of the total mass of the Milky Way [56].
According to different models, the dark matter density has it peak at the Galactic Center and decreases while going further away from the center of our galaxy. Many measurements

results reported a local dark matter density of $\sim 0.4\,\mathrm{GeV/cm^3}$ [60] [20]. The model of dark matter density of galaxies can either be obtained numerically or inferred experimentally.

Figure 4.6: Navarro, Frenk and White profile in 2008.

In the early 1990s the first numerical simulations of dark matter halos became available (Navarro, Frenk and White [59]) which can be seen in figure 4.6.Their model is based on simulations of N-body collisionless heavy particles set in a grid at a distance form each other of $\sim 100\,pc$. The system is slightly perturbed and then let evolve under the hypothesis of only gravitational interactions. This model is well fitted by the equation 4.1

$$\rho_{NFW}(r) = \frac{\rho_i}{(r/R_s)(1+r/R_s)^2} \tag{4.1}$$

where ρ_i is related to the density of the universe at the time of the collapse of the halo and R_s is a scale factor. At small radii ($r < R_s$) the slope of the density goes as $\rho \propto r^{-1}$, at large radii ($r > R_s$) the density goes as $\rho \propto r^{-3}$, changing slope at $r = R_s$. The profile has a divergent (cuspy) central density, as can be seen in Figure **??**, which is clearly an effect of numerical simulations.

Experimentally, the density profile of dark matter can also be obtained observing the rotational curve of spiral galaxies: the velocity dispersion was measured at different radii from the galaxy's center, but it didn't decrease, as was expected, at large radii, remaining instead approximately constant. The mass required to sustain such high rotational velocities in the outer part was at odd with the luminosity mass, implying that the rotation there must have be caused by some "dark" material, whose density profile (at large radii) closely resembles that of an isothermal sphere, i.e. $\rho \propto r^{-2}$. In the inner parts of galaxies, the rotation velocity associated with dark matter is found to rise approximately linearly with the radius, suggesting the presence of a central core in the dark matter distribution.
This big discrepancy at small radii between the cuspy NFW profile and the core isothermal profile is known as the "core-cusp" problem. At first glance it might seems that data provide good evidence for core profile, but there are some systematic effects which have to be taken into account [32]: firstly, the isothermal profile come from the assumption that the tracers move on circular orbits. If for some reasons the orbits are elliptical or the motion is distrubed somehow, this will lead to an underestimation of the slope. Since at small radii orbits are usually not circular, models obtained experimentally can not precisely investigate how the density profile behaves near the center of a galaxy. The second reason is connected to mis-spointing problems of the telescope's slit: if there is a small offset between the slit position and the central dynamical position, the "cusp" region might be missed.

On the other hand, there are also some drawbacks in the estimation of the DM profile via N-body simulations: they don't keep under consideration the baryonic interaction, which is non dissipationless, whose effect on the profile is still unknown. Because of the presence of baryons, the mass density would increase, so would the gravitational field, ending up amplifying the DM content at small radii. On the other hand, including baryons would imply including star formations activities, such as supernovae explosion, whose shock wave would push further away the matter, dumping the density profile at small radii.
Another model which fits well the data is the Einasto profile, which has an additional parameter compared to the two parameters of the NFW profile and is described by equation 4.2

$$\rho(r) = \rho_{-2} \exp -2n[(r/r_{-2})^{1/n} - 1] \tag{4.2}$$

where r_{-2} is the radius at which the logaritmic slope of the density distribution has a value of -2,ρ_{-2} is the corresponding density value, and n is the additional parameter. Depending on the value of n, this model can solve the central divergency of the NFW profile, as can be seen in figure **??**.

4.6 The MeV/GeV point source

In 2004 three different imaging atmospheric cherenkov telescopes, the Whipple, the Cangaroo-II and the H.E.S.S Telescopes, detected almost simultaneously a VHE γ-ray signal coming from the GC [50], [69], [8]. The source showed a point-like emission with no flux variability, and it was called HESS J1745-290. As can be seen in Figure4.7, the spectrum is well described by a Power law with exponential cut-off [7]:

$$\frac{dN}{dE} = \phi_0 \times \left(\frac{E}{1\text{TeV}}\right)^{-\Gamma} e^{-\frac{E}{E_c}} \tag{4.3}$$

where $\phi_0 = (2.4 \pm 0.10) \times 10^{-12}\,\text{TeV}^{-1}\text{cm}^{-2}\text{s}^{-1}, \Gamma = 2.10 \pm 0.04$ and $\text{E}_\text{c} = (14.70 \pm 3.41)\,\text{TeV}$

Coincident with the position of the GC, a HE gamma-ray source named 2FGL J1745.6-2858 has been observed by the Fermi-LAT [23]: its spectrum does not show any flux variability and is well described in the energy range between 0.3-100 GeV by a broken power law with spectral indexes of $\Gamma = 2.20 \pm 0.04$ below the break energy of $E_b = 2\text{GeV}$ and $\Gamma = 2.68 \pm 0.05$ above the break energy. As can be seen in Figure 4.8 the spectrum at its high energy is steeper than that of HESS J1745-290, but overall the fluxes of the two sources match well, suggesting a common origin of this gamma-ray emission.

The mechanism hidden behind both the emissions at HE and VHE has not yet been fully understood, also it is not entirely clear if the emission measured by the Fermi-LAT and the ground-based cherenkov telescopes is produced by the same astrophysical object. Assuming the same object is behind this emission, models need to explain these properties:

- no flux variability on time scales of minutes or years;
- the emission region of HESS J1745-290 is point-like and coincident with the position of SgrA* while 2FGL J1745.6-2858 shows a hint for a moderate extension;
- the spectrum between 100 MeV and 30 TeV is a hard power law with breaks and cut off at various energies ($\sim$ 2GeV, $\sim$ 20GeV, $\sim$ 10TeV).

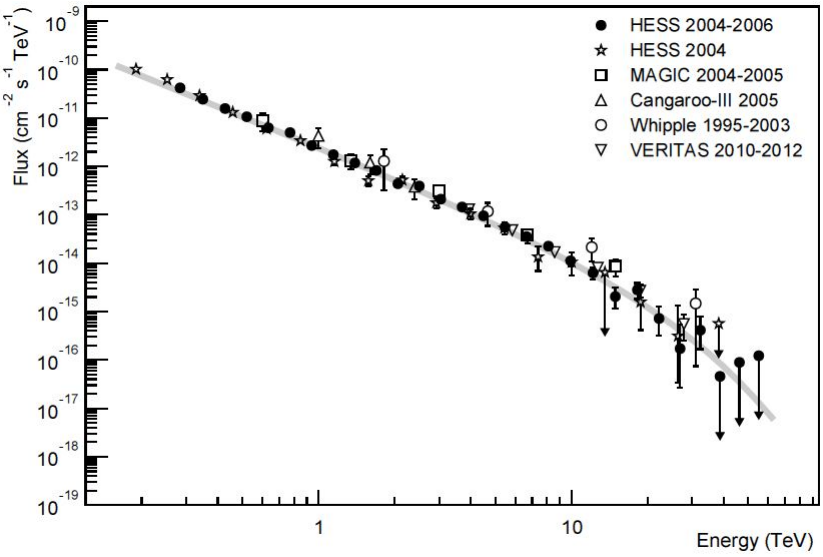

Figure 4.7: Gamma-ray spectrum of the GC source HESS J1745-290: a power law with exponential cut-off is used to fit the data obtained with HESS, MAGIC, Cangaroo-II, Whipple and Veritas telescopes.

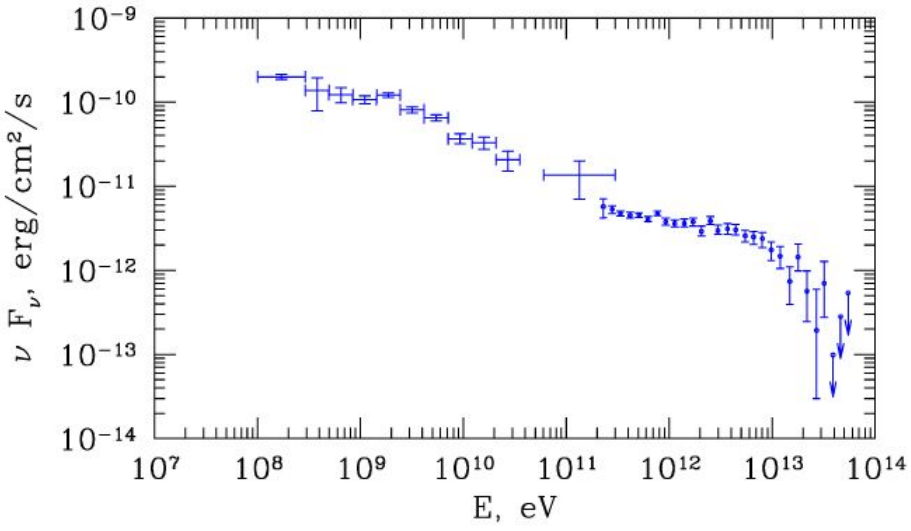

Figure 4.8: Spectral energy distribution of Fermi-LAT source 2FGL J175.6-2858 up to energy of $\sim$ 100 GeV and of HESS J1745-290 from HESS telescope above 100 GeV. [73]. Due to different flux integration regions connected to different angular resolution of the insturments and systematic uncertainties connected to hadronic background and diffuse emission, how to connect the two curves has still some uncertainties, but overall the energy spectra match well, suggesting a common origin of the emission.

4.6.1 Origin of the signal

The connection of this emission with SgrA* is compelling, but in the vicinity of the black hole there are also other astrophysical objects candidated for this emission: the nearby objects SgrA East and the recently discovered PWN G359.95-0.04.

SgrA East Since SgrA East is a supernova remnant, it is a good candidate for VHE gamma-ray emission, due to synchrotron radiation. It needs to be verified if the position of SgrA East is compatible with the emission region of VHE gamma rays: although the angular resolution of gamma-ray instruments is not good, point-like sources can be localised quite precisely because the uncertainty of the position of their centroids roughly scales as $\theta/\sqrt{n}$ where θ is the angular resolution and n is the number of detected gamma-rays. So for long time exposure and/or point-like sources, if systematic uncertainties are under control, the measurement of the centroid location can be obtained on a arcsecond scale.

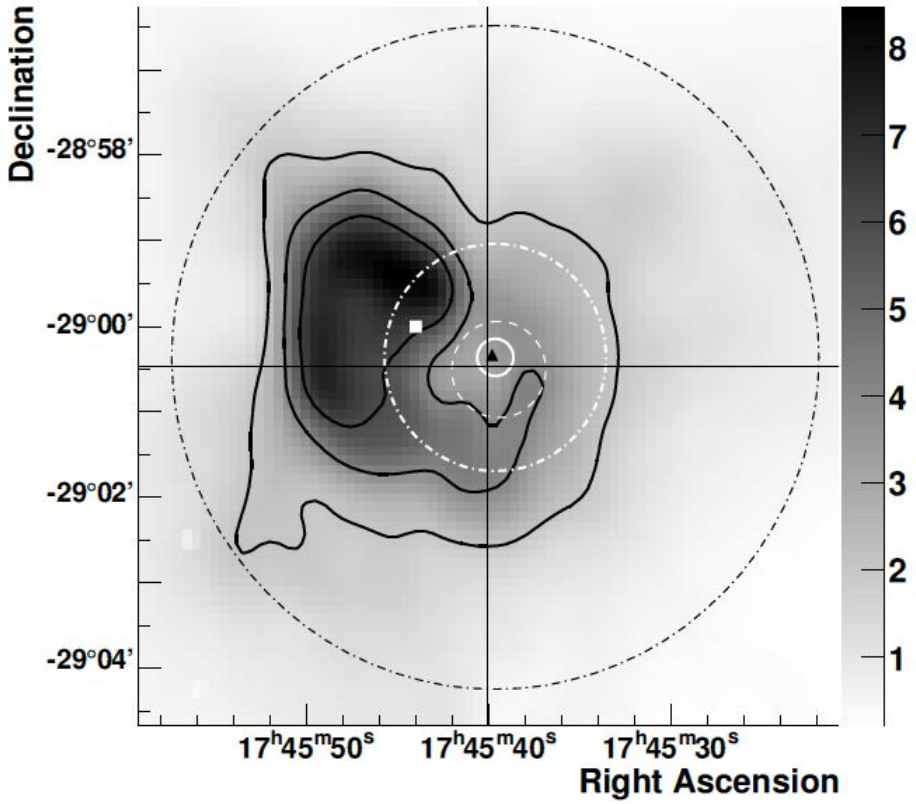

Figure 4.9: Map of the 90cm VLA radio flux density of 20 pc around the GC coming from the SgrA East as a shell like structure surrounding SgrA* in projection. The black contours shows the radio flux levels of 2,4 and 6 Jy/beam. The white square denotes the center of SgrA East, the black triangle denotes the PWN position, and the cross hairs denotes the SgrA* position. The white circle shows the 68% CL total error of the best-fit centroid position of HESS J1745-290. The white dashed-dotted line shows the 95% CL upper limit contour of the gamma-ray source extension and the black dashed-dotted line shows the 68% containment region of the HESS PSF. [73]

As can be seen in Figure 4.7, precise measuremens of the centroid of HESS J1745-290 shows that SgrA East is disfavoured for being the main cause of the VHE emission [4].

PWN G359.95-0.04 As we previously saw, the PWN G359.95-0.04 is very close to SgrA* (a projected physical distance of 0.32 pc), making impossible to distinguish between these two objects by the observation of HE and VHE gamma-ray emission. As we already discussed, the non-thermal electrons are cooled by synchrotron radiation, but calculations show that a population of non-thermal electrons from PWN can account both for the X-ray and VHE gamma-ray emission: the far IR photons are up-scattered by inverse compton to VHE

energies and despite the strong synchrotron cooling a large enough number of gamma rays survive to account for the VHE emission. The defect of this model is that it underestimates the emission at MeV and GeV energies, since a power law shape is observed when the model predicts a spectral shap due to IC, which shows a peak-like structure. Therefore the PWN scenario does not describe the emission observed if we assume that HESS J1745-290 and 2FGL J1745.6-2858 are driven by the same mechanism.

SgrA* SgrA* is the only candidate which survives: the production might be either of astrophysical origin, through particles acceleration mechanism but also through dark matter annihilation.

Hadronic and leptonic models A multitude of processes can produce populations of relativistic particles leading to γ-ray energies up to several TeV and possibly beyond, but the problem is to find a model which fits both the GeV and TeV observed emission. Depending on the type of particles involved in the acceleration process, we have leptonic models or hadronic models.
A possible hadronic model [23] considers that a significant fraction of the protons of the CR accelerated near the black hole may penetrate the surrounding dense gaseous environment and emit gamma rays through neutral pion production which then decay into gammas. The injection spectrum of these protons has a power-law spectrum with a spectral index $\Gamma \sim$ -2 and an exponential cut-off at 100 TeV. The efficiency of this process and the energy spectrum of the resulting γ rays depends on the time spent inside the region of dense material, on its density and on the injection rate of the protons. At energy below 100 MeV a cut off is expected, due to the π^0 production limit. The low energy injected protons will diffuse slowly and the time spent inside the dense region is of the order of the timescale of activity of the particle accelerator. Therefore their spectral shape will mirrow the spectral shape of the injected protons. For high energy injected protons, the diffusion is faster and they start to travel almost undisturbed through the emission zone and therefore again mimicking the injected spectral shape. Injected protons with intermediate energy have a much steeper diffusion-processed spectrum, representing the transition between the two extremes. As previously said, the observed gamma emission also thepends on the injection rate of the protons. It can be modelled, as can be seen in Figure 4.10, through three different scenarios: a proton flare occured 300 years ago of 10 years duration , a constant source that switched on 10^4 years ago and the superposition of the two.

Under these assumptions, the protons produced in the 300 years old flare influences only the GeV part of the spectrum, since only the protons from the flare still trapped in the dense region produces pions. At energy of the order of TeV, most of the protons of the flare have already flown away. The TeV part of the spectrum is explained by a steady proton source.
Another hadronic model describes the MeV and TeV emission through two different emission region [36], using a numeric simulation of the diffusion of CRs through turbulent magnetic fields. The surrounding environment of the black hole is described as a torus of dense material with an inner radius of 1.2 pc and thickness of 1 pc embedded inside a wind zone of lower density and of 10 pc in diameter. The density distribution in the wind zone is connected to the interactions of winds from the surrounding young stars. The injected mildly relativistic protons are assumed to come from the extremely high energy tail of the thermal distribution near the black hole. These protons random-walk in the medium until they collide with an

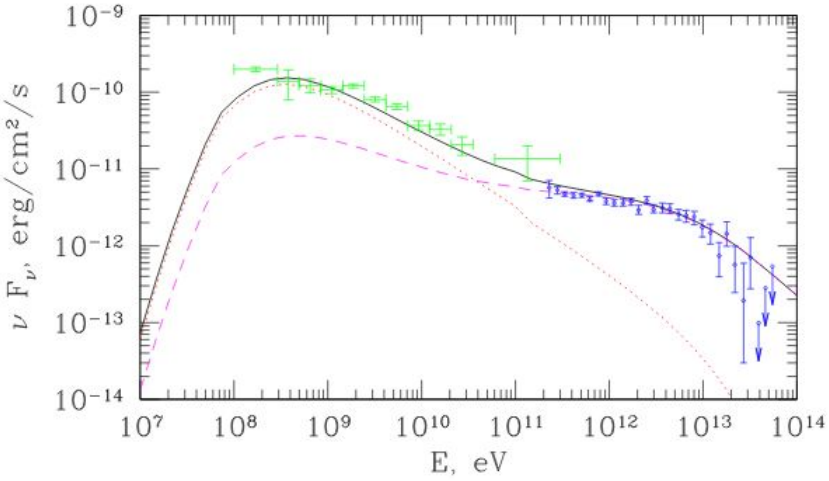

Figure 4.10: Fit of the Fermi and Hess data points for a hadronic model requiting a time variability for the protons production. The green points shows the Fermi data while the blue points show the HESS data. The magenta dashed line shows the emission resulting in a proton flare happened 300 years ago with a 10 years duration, the red dotted lines shows the constant proton source which switched on 10,000 years ago and the black line represents the superposition of these two cases, which represents a good fit of the data. The size of the emission region is considered to be of 8 pc. [23]

ambient proton in the torus or in the wind zone, producing neutral pions which then will produce gammas. As can be seen in Figure 4.11, the torus contains mainly low energy protons that in the high density material have a high probability of interaction, contributing mainly to the peak observed in the Fermi region of the spectrum. TeV protons have a higher probability to interact in the wind zone, producing the high energy part of the spectrum. These model properly describe the observed spectrum from GeV to TeV without requiring any time variability of protons production.
Leptonic models have problems in accounting for both the HE and VHE emission at the same time. A possible leptonic scenario [53] considers a model where the high energy electrons come from the flare events that occur near the central black hole and interact via inverse compton scattering with the soft photons produced by the dusts and the dense population of stars inside the central few parsecs of the GC. By changing the parameters, this model can either describe the HE or VHE emission, but not both.
Another possible scenario is a hybrid model of leptonic and hadronic scenarios [45]. The leptons and hadrons cosmic rays were accelerated simultaneously during past activity of GC and then diffused outwards, interacting with the interstellar gas and the background radiation field. With the fast cooling of the radiation field, the electrons cool down and radiate GeV photons through inverse Compton scattering off the soft background photons, synchrotron radiation in the magnetic field and bremsstrahlung radiation in the Interstellar Medium. On the other hand, collisions between the hadrons with the gas is responsible for the TeV emission. The total observed emission, as can be seen in Figure 4.12 depends also on when the cosmic rays were injected: the younger the injection is, the higher the energy of the electrons is and the relative fraction of low energy electrons is smaller due to the slower propagation, resulting in harder spectra. Similarly also the protons evolve with time: the older the injection, the more high energy particles diffuse out of the inegral region, resulting in a softer spectrum.

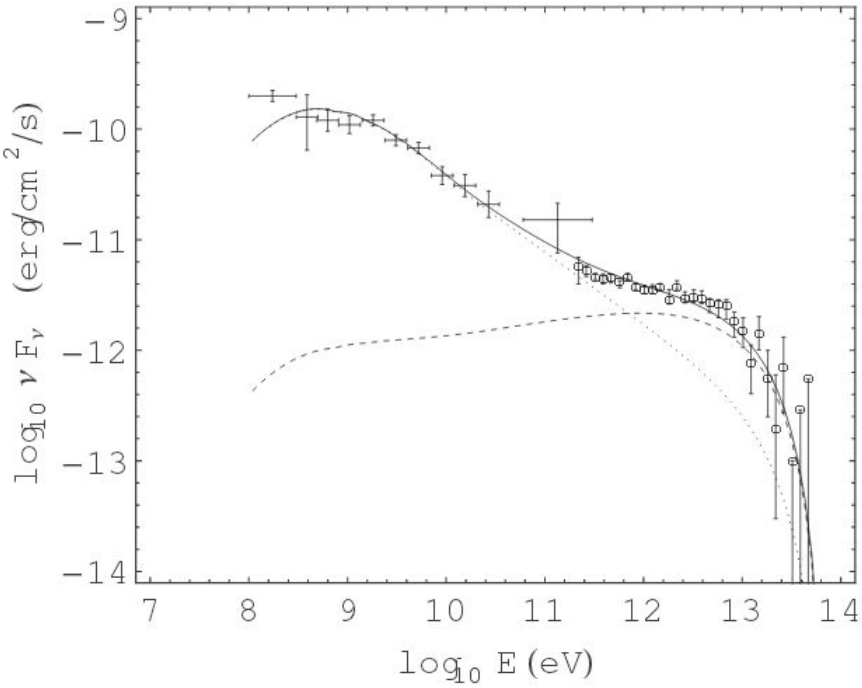

Figure 4.11: Fit of the Fermi and Hess data points for a hadronic model without requiring any time variability of protons production. The dotted line shows the spectrum produced by scatter in the torus and the dashed lines show the spectrum produced by particles that scatter in the torus. Both the spectra are normalized to the Fermi and Hess data points. [36]

DM annihilation Let us now inquire about the DM origin of the signal: since the Dark Matter density profile is expected to be peaked towards the center of galaxies, the VHE gamma-ray emission might be originated from annihilation of TeV-mass DM particles. Since HESS J1745-290 shows a point-like feature, it would need a rather cuspy DM density profile, otherwise a more extended emission would be expected. In addition, the HESS J1745-290 spectrum would need to mimic the typical spectrum produced by DM annihilation. As we will see in the next chapter, such spectra tend to be strongly curved as the energy approaches the DM particle mass. But as we previously discussed, the HESS J1745-290 spectrum shows a power law over most of its range, showing a cut off at energies of tens of TeV, disfavouring the DM annihilation hypothesis as the only source of the VHE gamma-ray emission and suggesting that this might be produced mainly by astrophysical processes. However, based on spectral fits, a contribution of 10% of DM annihilation to the signal can not be ruled out [9]. Under this hypothesis and considering a Navarro-Frenk-White profile, 99% CL upper limits on the velocity weighted annihilation cross section $< \sigma v >$ are obtained and result to be of the order of $10^{-24} - 10^{-23}\,\mathrm{cm^3 s^{-1}}$ which is at least two orders of magnitude above the thermal relic cross section, and so do not put any further constraints on the DM model.
Another possibility is considering the combined emission of HESS J1745-290 and 2FGL J1745.6-2858 as originated from DM annihilation into various particles on top of a power law background of astrophysical origin [21]. This model requires that the innermost part of the DM halo is even more compressed that the NFW profile, as expected from the point-like morphology of the emission. Also, no good fits are found for annihilation of DM into leptons; in Figure 4.13 can be seen the results obtained for a final annihilation state of $W^{\pm}$: a DM mass of ~ 52 GeV is obtained and a underlying background spectrum with spectral index of

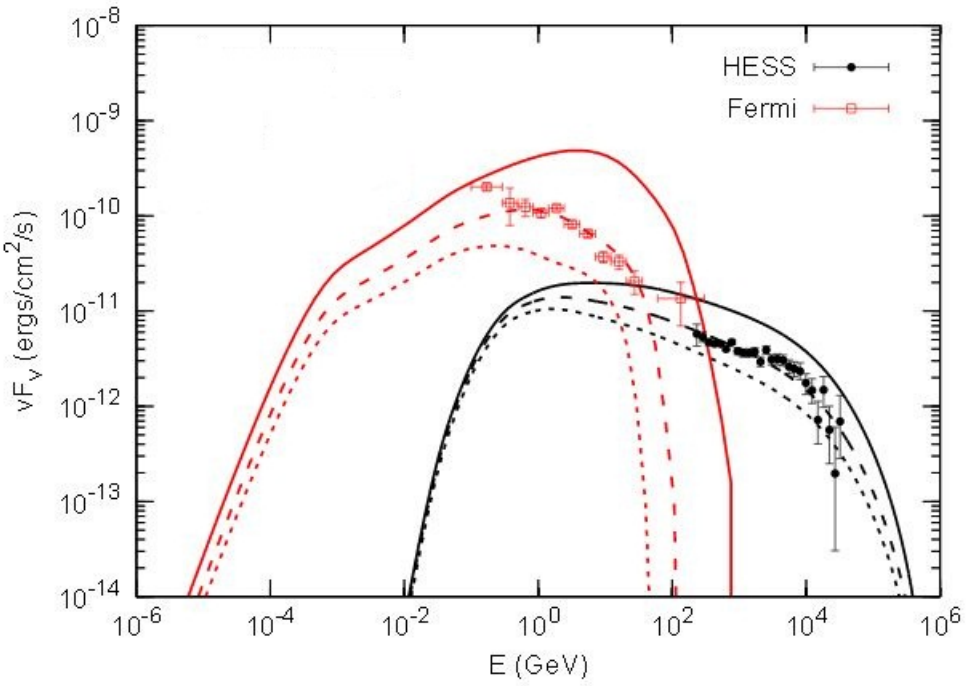

Figure 4.12: The calculated spectra produced in the hybrid model: the red lines show the emission produced by electrons, while the black line shows the emission produced by protons. Different lines show the effect of observational time (dotted=100 yrs, dashed=200 years and continues 300 years after the injection happened) [45]

$\Gamma \sim 2.6$ is required.

Analysing only the Fermi data another possible dark matter interpretation can be obtained [43]. The background is considered as composed of the diffuse gamma emission and the the TeV HESS point source. While the latter was obtained by an extrapolation of the measured power law to lower energies, the former was obtained by observing the emission fom $3^o < |l| < 6^o$ and modelling it as an exponentially function which falls off away from the disk. Additionally, the halo was modelled with a NFW profile with a scale radius of 20 kpc and normalized so that the solar dark matter density at coincide with the one observed: this request, after the subtraction of the background to the observed data, implied a steeper profile of γ=1.1 than the NFW (with γ=1 for the NFW profile); this steeping might be caused by adiabatic contractions of the gas due to baryonic gas. As can be seen in Figure 4.14, assuming an hadronic channel decay into $b\bar{b}$, the best fit of annihilating dark matter suggests a dark matter mass of 25-30 GeV and an annihilation cross section $< \sigma v > \sim 9 \times 10^{-26}\,\mathrm{cm^3 s^{-1}}$, a factor about three times larger than the one predicted for a thermal relic.

The dark spot of this approach lays in the background: an astrophysical background, for example produced by pion decay into gammas in a spherical region around the Galactic Center, would produce a similar spectrum and morphology to the one produced by annihilating dark matter particles, making it difficult to discriminate amongst the two.

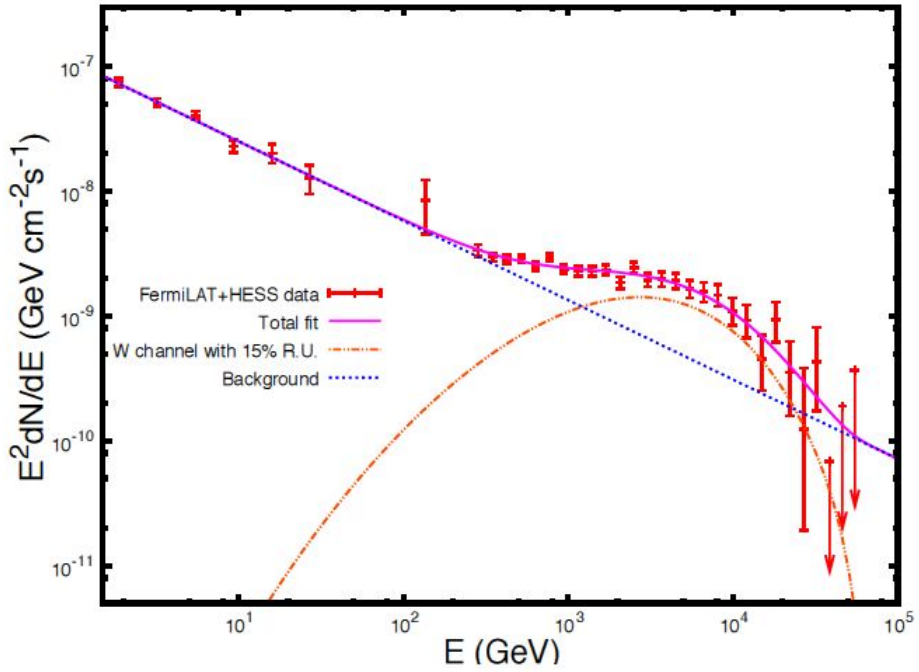

Figure 4.13: The full pink line shows the total fit to the spectral energy distribution of the Fermi-LAT at HE and HESS at VHE GC source. The dashed dotted line shows the DM annihilation into final state composed of $W^{\pm}$ on top of a blue dotted power law shaped background. [**?**].

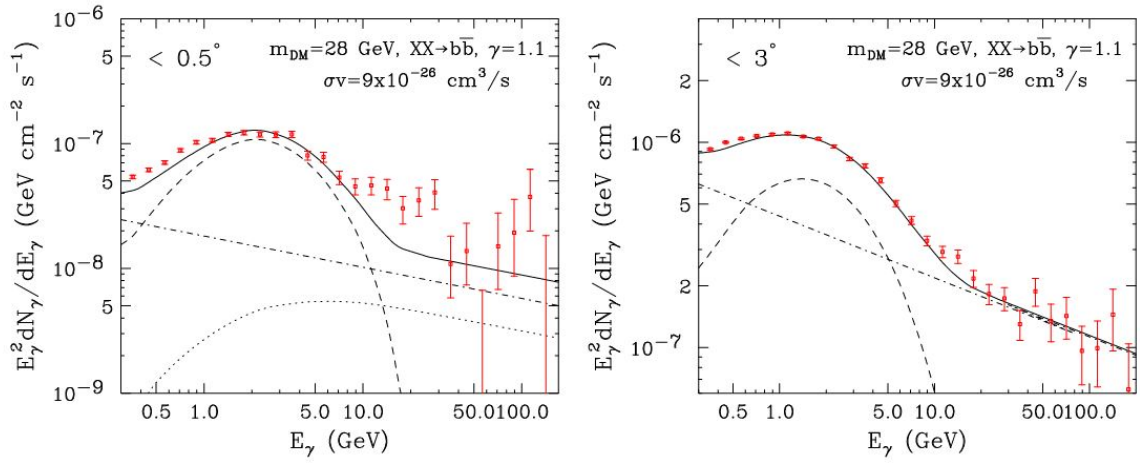

Figure 4.14: Measured spectrum of the Galactic Center within 0.5° on the left and 3° on the right. The dot-lashed line denotes the diffuse background and the dotted line the HESS spectrum extrapolated to lower energies: below 1 GeV the Fermi data do not appear to contain significant emission from this source so it was suppressed. At last, the dashed line denotes the dark matter annihilation spectrum to $b\bar{b}$, assuming a dark matter halo profile slightly more cusped than the NFW profile ($\gamma = 1.1$): it shows a bump-like feature at 1-5 Gev which can be produced by a dark matter particle with mass between 25 and 30 GeV. [43]

Chapter 5

MAGIC Data Reconstruction and Analysis

> A page from a journal of modern experimental physics will be as mysterious to the uninitiated as a Tibetan mandala. Both are records of enquiries into the nature of the universe.
>
> Fritjof Capra

5.1 Data Reconstruction

The core of the MAGIC data reconstruction and analysis is a set of libraries and programs gathered into a software package dubbed MARS (Magic Analysis and Reconstruction System) [77], which is developed and maintained by the MAGIC collaboration. It is written in C++. The reconstruction and analysis chain is depicted in Figure 5.1. The upper dashed box represent the basic event building steps, which consists of gathering all information related to the event in one structured file. These includes camera pixel-wise information (number of phe, arrival time, etc) with instrument-related information (temperature, humidity, pointing position, etc). At the end of this preliminary step, *"superstar"* files (the name is conventional), contain already stereoscopic image information such as size, length, width of the shower images in the camera. In normal analysis, this is the starting point, however, in some non-standard analysis, data can be handled at previous level, where pixel-wise information are available, before they are combined into global event parameters. In this analysis, we use as basic event the standard stereoscopic information of the superstar files. The steps illustrated in the bottom dashed box of Figure 5.1 are discussed below.

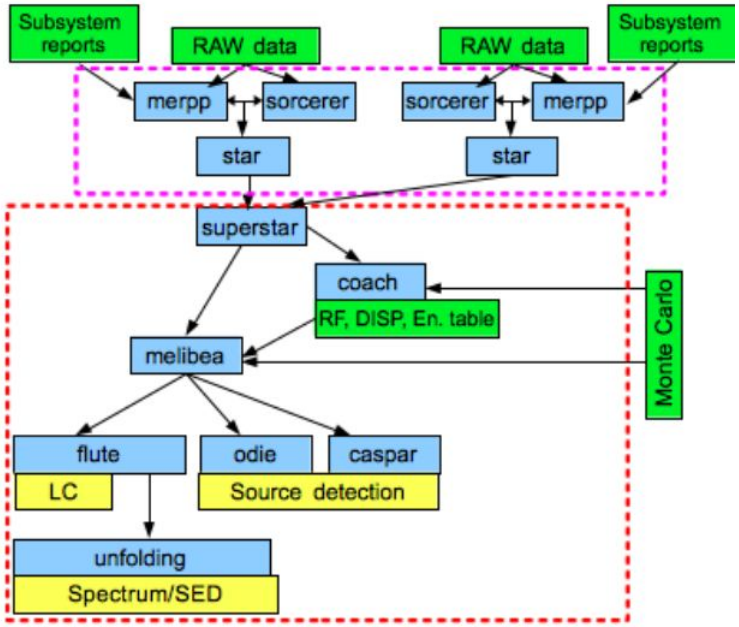

Figure 5.1: Representation of the MARS analysis chain: the dashed magenta lines shows the automatic processes, while the dashed red line shows the analysis performed manually. The blue indicates the programs and the yellow their interesting output [77].

The data reconstruction is the result of the combination of the proper source data set, i.e., those taken pointing the actual target of interest which in this work is the Galactic Center data, as well as additional data that are necessary to actually reconstruct the primary gamma ray information, as well as perform a powerful background discrimination. These additional inputs are: a) data taken observing sky regions where no gamma rays are expected to be used as seed for the Random Forest (see later) for the separation between gamma-like and hadron-like events; b) Background Control data, taken directly within the same FOV of the target source, and used to statistically estimated the putative number of excess events from a certain sky direction; c) the MonteCarlo data which are used to have a reference well known data sample. On-Target and Background Control data need to be taken under similar observational conditions: similar altitude (Zenith Angle), similar instrumental setup, similar sky quality conditions, and possibly close in time

Galactic Center data For our analysis the source data are the Galactic Center data (*on data*). For this work, we selected a subset of the whole data samples available on the Galactic Center, corresponding to an instrument setup called ST0303. Using data from different periods would have implied a non-negligible extra amount of work that anyhow was outside the main goal of thesis, which is the demonstration of a reconstruction algorithm for dark matter searches. At the MAGIC telescopes site, the Galactic Center culminates at high zenith angle, $\sim 58^{o}$ Zd. As can be seen in figure 5.2, the Zd range of our data sample goes from about 58^{o} Zd to about 70^{o} Zd, and covers a period from March, 11th 2013 to July, 7th 2014 for a total of 77.4 hours of effective time.

A preliminary step in the data reconstruction consists on an initial selection of data based on quality check (actually done by a MARS executable called *quate*) is done.This program, besides very basic consistency checks, select data according to two very fundamental parameters:

1. the median camera illumination level

2. the atmospheric transparency

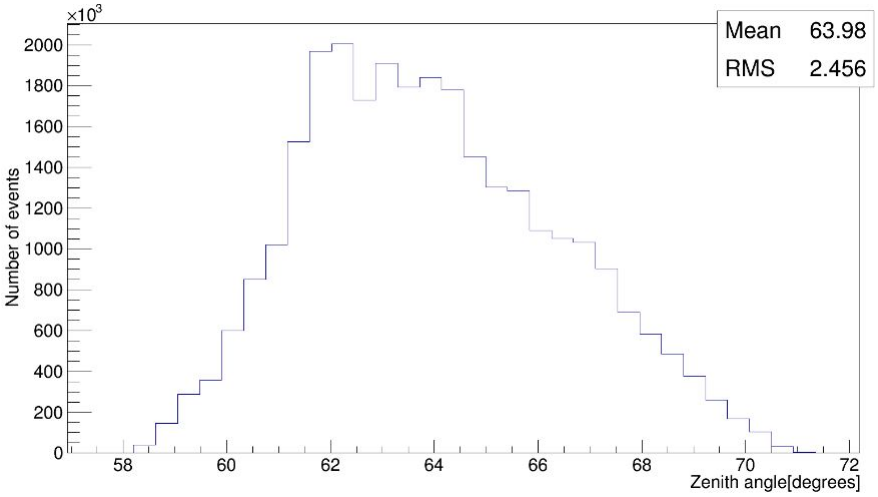

Figure 5.2: Representation of the zenith angular distance distribution of the data: on the x axis there is the pointing position of MAGIC telescopes, on the y axis the number of events of the data; the mean angle is 63.98°.

.

These cuts select data as shown in Figure 5.3.

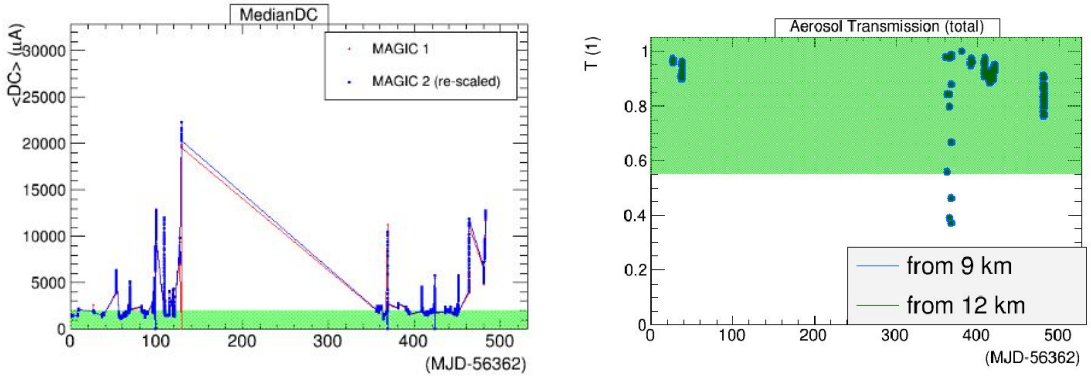

Figure 5.3: Left: DC as a function of Julian days; the bright green region indicates the data which survived to the DC cuts; the blue colour shows the MAGIC-I DC and the red colour shows the MAGIC-II DC re-scaled. . Right: Transmission as a function of Julian days. Large aereosol components in the atmosphere scatter the Cherenkov light, making it difficul to identify and reconstruct the image on the camera.

The median DC is the median current of the PMTs produced by the light incident on the camera, which is a combination of electronic noise and the NSB (composed of photons coming from stars and/or from the moon). The higher cut on the median DC is necessary to select data taken in "dark sky" conditions. The reason is that data taken with high median DC level (larger than 2μA) needs to be analysed with non-standard reconstruction algorithm, because the presence of strong illumination determines an increase of signal in the camera that, if not treated properly, produced strong systematics. The analysis of high-DC data is possible of course, and will be performed in further analysis of this source, but it is out of the scope of this thesis. We notice in fact, that a large fraction of observation time on the GC

was taken during "moon" nights.

The atmospheric transparency is also an important quality factor. The relation between photon density at ground and primary gamma-ray energy depends in fact on the atmospheric transparency, which rule the absorption of Cherenkov photons from the emission point to the ground. In case of different optical transmission (as it is in the presence of a cloud) this relation should be adjusted. This is done in MARS automatically making use of information retrieved with a instruments called LIDAR: a laser is shot in the close-by direction to which the telescopes are pointing; the light is reflected and scattered in the atmosphere by molecules through the Rayleigh scattering and by particles through the Mie scattering. The atmosphere transmission is then calculated from the intensity and arrival time of the reflected light and it assumes value from 0 to 1. We cut the data with transmission above the value of 0.55, as can be seen in Figure 5.3. We notice however that only few data have transmission below 0.55.

Background Control data The Background Control Data are data taken in sky regions where no gamma signal is expected in order to be sure that the events observed were triggered only by hadronic showers and are later used to train Random Forests. In Figure 5.4 the Zenith angular distributions of these dark regions can be seen. It is important that this distributed encompass the same zenith angle range than that of the GC. The executable *quate* is also run on these data for the quality check with the same settings of the GC data (see Figure 5.5).

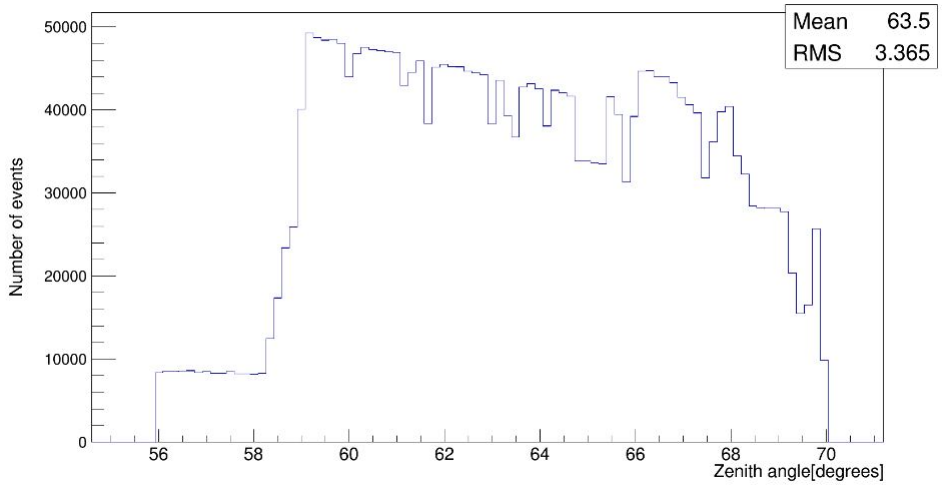

Figure 5.4: Angular distribution of the Off data.

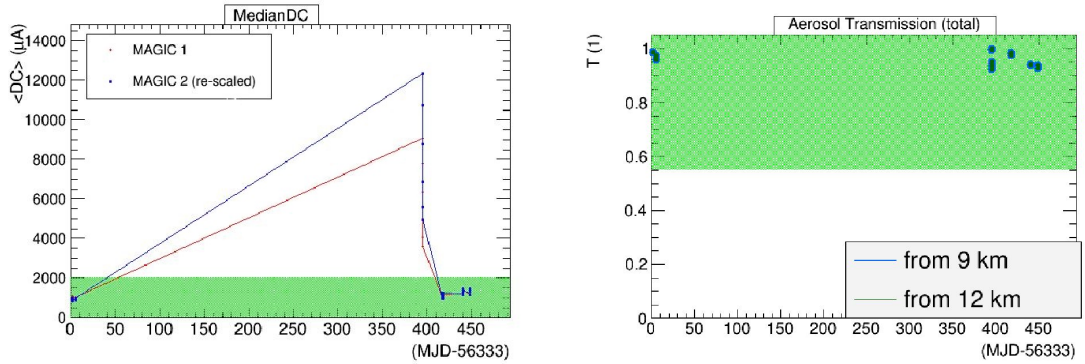

Figure 5.5: Left: DC as a function of Julian days; the bright green region indicates the data which survived to the DC cuts. Right: Transmission as a function of Julian days.

Off data The Off data are used to estimate the background, which is of great importance in the analysis since it has to be subtracted from the On region to obtain the number of observed gamma rays. In order for the background subtraction to be realistic, the Off data need to have the same Zenith and Azimuth angle of the source data and to be simultaneously taken: different Zd angles imply different atmosphere depths and therefore different absorption of the shower. The dependence on the Az angle arises because of the asymmetry introduced by the geomagnetic field; in addition if the Off data are taken at a different time, the atmospheric conditions changes and so does the telescopes performances. There are two approaches for the Off data: the On-Off mode and the wobble mode.

- With the On-Off mode the source data and the Off data are two separated regions in the sky to where the telescopes point alternatively. The source is situated at the center of the camera and the data are taken with the same Zd and Az distributions. This technique, though, has some disadvantage, the first of which is the time difference and the inefficiency since for half the time the source is not observed.

- For this reason the Wobble mode is mostly used amongst IACT, since the On and Off data are taken simultaneously, i.e. the Off data are taken by selecting an Off region in the same data where the source of interest is observed. The telescopes point alternatively every 20 minutes to two or more (usually four) sky regions around the source of interest with an offset of a small angle (0.4° for MAGIC); the Off data can then be selected either simultaneously or from the wobble partner. In the first case, the Off positions are regions of the sky with the same offset of the source from the center of the camera. The position symmetrical to the source with respect to the center of the FoV is called *anti-source*; more Off regions can also be selected symmetrically around the anti-source as can be seen in Figure 5.6.

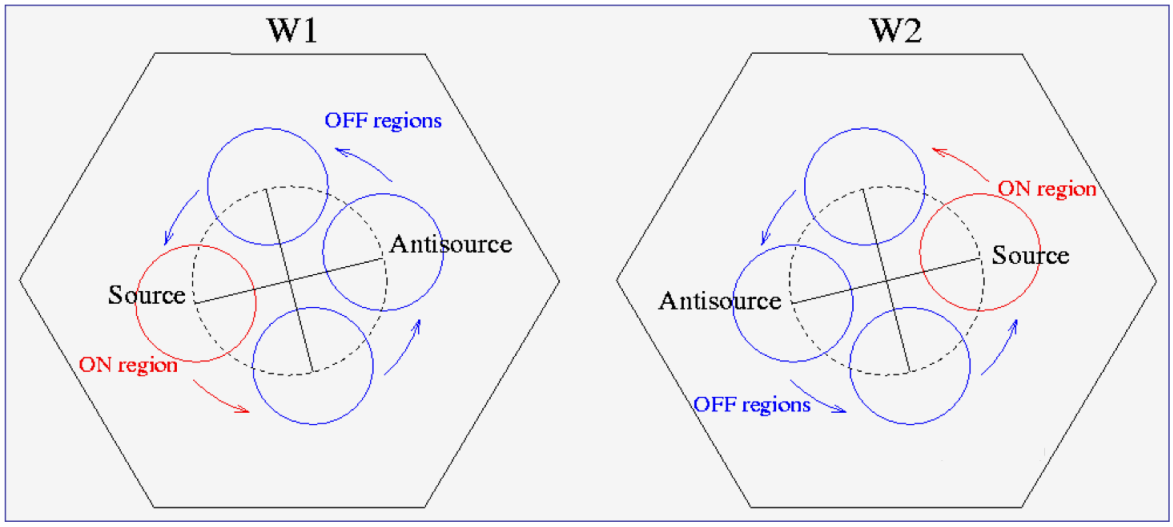

Figure 5.6: Wobble mode in case of two wobbles: the red indicates the On region and the blue the possible candidates for the Off regions. The telescopes point at two different sky regions with different Zd and Az and therefore the source is located in different regions of the camera.

The On and Off regions have a slight difference in Zd and Az and this has an impact on the acceptance of the camera; however using several wobbles, the position of the On and Off regions in the FoV of the camera change periodically, reducing the possible differences of the acceptance. The Off from the wobble partner method solves the previous problem: for each source data taken in a wobble pointing - for instance W1 there is, in another wobble pointing, an Off position which follows approximately the same path on the FoV that the source follows in W1.

MC data The MC data are samples of simulated gamma showers, which are later used to separate hadronic and gamma events in the source data and to estimate the energy of the observed gamma events. The MC data need to be simulated with the same Zenith angle, and we will use two samples, between 50 and 62 Zd and between 62 and 70 Zd. The MC simulations need to be as close as possible to the real gamma showers, following it step by step, using MonteCarlo programs. First CORSIKA (COsmic Ray SImulation for KAscade) simulates the gamma shower until it reaches the MAGIC telescopes, and contains informations such as the arrival time, the incoming direction and the energy. Then the software REFLECTOR simulates the absorption of the atmosphere and the reflection into the camera, also keeping into account the PSF (Point Spread Function) of the system. At last, CAMERA simulates the camera, the triggers and the readout. In the end the MC data have the same format as the raw MAGIC data. Since the GC is an extended source, diffuse MC have been used for this analysis .

Starting with these sets of data, the first step is to find a way to estimate the likeliness to be a gamma-ray event: this is done by the MARS program *coach*, which uses Random Forest (RF) methods [10] confronting the pure gamma events (the MC data) with the pure hadronic events (the Dark Patches). The RF are optimized decisional trees built by using a set of discriminating parameters (the Hillas parameters and some other more, specially the height of the shower maximum, a parameter easily produced with stereoscopic information). The output of *coach* are RF matrices for the gamma/hadron separation, for the energy estimation and for the stereo *disp* estimation (see Appendix C). These matrices are then used by the MARS program *melibea* which assigns to each events those parameters produced by the

RF: the *disp* value, an energy estimator and a "hadronness" value to each event, where the hadronness is connected to the probability that an event is of hadronic origin, for which the maximum value is 1, or of gamma origin, for which is zero. It is virtually impossible to determine with absolute certainty whether an event is of electromagnetic or hadronic origin, specially because every hadronic shower has always sub-electromagnetic showers which are exactly similar to gamma-ray induced showers. However, in the ON region, in case of significant flux from a source, there is an *excess* of events with very low hadronness with respect to the the events taken in the OFF region. This fact is used to asses the detection of a source. In this case, a *cut* in the hadronness parameter is optimized in order to maximize the signal to noise ratio, and therefore the significance. Too strict cuts normally select too few signal events, too lose cuts normally select too much background. The optimization is normally tested on a reference source (e.g. the Crab nebula) and must be done carefully in order not to bias the result, but to maximise the sensitivity.

5.2 Data Analysis

From the *melibea* output, the most important products of the reconstruction can be produced: sky-maps, spectral energy distributions (SEDs) and theta-square plots (detection plots). Thanks to the MARS program *odie*, theta square plots can be obtained: they are basically histograms where for each bin of θ^2 (which is the angular distance from the source) the number of excess events is estimated by comparing ON and OFF distributions, after selecting the size of the expected *signal region*. This region has an angular extension that is at minimum the size of the Point Spread Function of the telescope (for point-like sources), but can be extended if the target expected emission is instrinsically larger than the PSF. The total number of events will include both the gamma events and the background, which is given from the Off data. The output so obtained can be seen in Figure 5.7: the total hours of observations after the cuts in our GC sample data are 42.2 hours and the significance (calculated with the Ly&Ma formula) is almost 14 σ. This means that our data sample clearly report a strong detection of the emission from a region located close to the Galactic Center. The origin of this emission was discussed in previous part of this text and thus far cannot be associated with absolute certainty to a precise emission region. However, the gamma-ray emission from the central black hole seems to be the most likely candidate.

Using the MARS program *caspar* we can obtain skymaps, an example of which as can be seen in Figure 5.8.

MARS encompass a high level analysis program called *flute* which can perform several tasks. One is to calculate the differential energy spectra and SEDs (Spectral Energy Distribution). The differential energy spectra, is defined as $d\phi/dE = dN/(dEdtdA_{eff})$ where ϕ is the gamma-ray flux, which is the rate of gamma rays per unit area and per unit time $\phi = N/(A_{eff}t)$ defined in unit of $\mathrm{cm}^{-2}\,\mathrm{s}^{-1}$; the SED is defined as $E^2\dot{d}\phi/dE$ in unit of $\mathrm{TeV}\,\mathrm{cm}^{-2}\,\mathrm{s}^{-1}$. The flux is calculated by counting the number of gamma-ray events obtained for each bin of energy an then divided by the effective observation time and the effective collection area of the same energy bin, where the effective time is the total time elapsed for observation minus the dead time introduced by the readout system, which for MAGIC is 10^{-26} s per event. The effective collection area is calculated from MC simulations as a function of the true energy E_{true}; however the number of excess are calculated in bins of estimated energy E_{est} since the true energy is unknown. The differential energy spectra and spectral energy distribution produced by flute ignore this discrepancy and the flux is calculated dividing the excess rates in bin of E_{est} by the collection area in the same bin of E_{true}. However the true

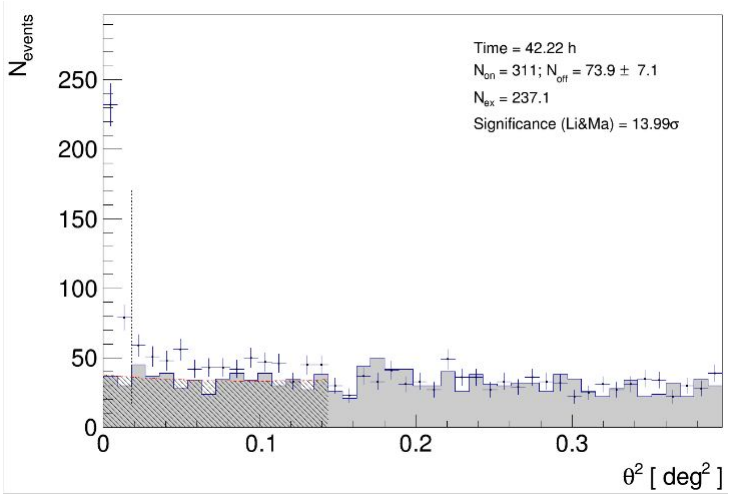

Figure 5.7: Theta-square plots of the GC: in the x axis there is the theta square, where theta is the angular distance from the source expressed in degrees, and on the y axis there are the number of events. The grey area indicates the estimated background while the crosses are the events of the On source.

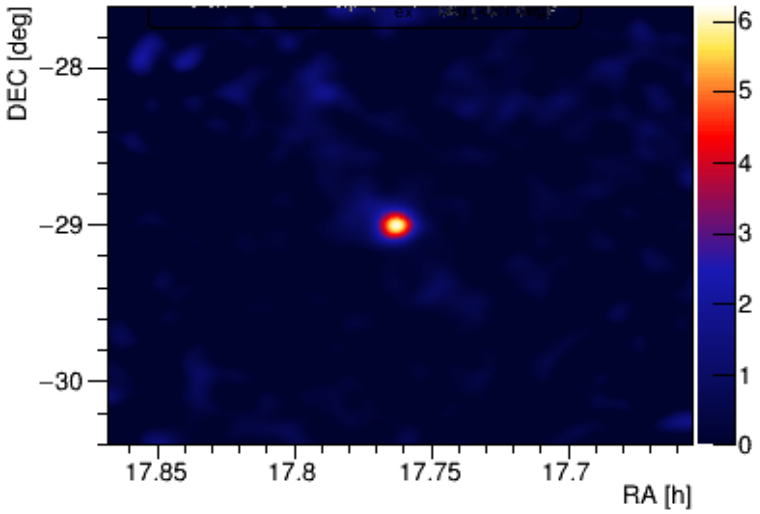

Figure 5.8: Skymap of the GC with the relative flux of the On and Off region. On the x and y axes there are respectively the Right Ascension and Declination of the GC; the colours indicates the values of this ratio.

energy is different from the estimated energy since the estimation of the energy is imperfect: some events with true energy in a certain bin $E_1<E_{true}<E_2$ might not be contained in the corresponding bin of estimated energy $E_1<E_{est}<E_2$ and they *spill over* or *migrate* into the higher or lower energy bin. Therefore the *migration matrix* is produced by *flute*, as can be seen in Figure 5.9, which correlates bins of true energy and bins of estimated energy. Another useful tool produced by *flute* is the hadronness cuts as a function of the estimated energy can be seen in the same Figure.

The MARS program *CombUnfold* uses the migration matrix to obtain a more precise SED which can be seen in Figure 5.10 based on several unfolding methods .

The analysis described above with the flute program is the standard MAGIC analysis but to obtain the results aimed with this thesis we need to follow a slightly different procedure: to search for an excess of the gamma-ray signal produced by dark matter annihilation, we

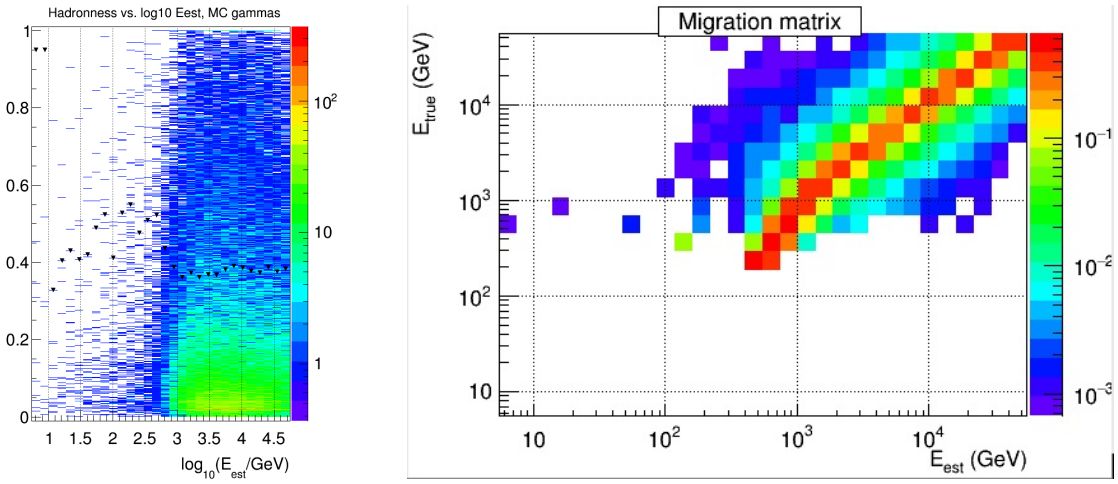

Figure 5.9: Left:Hadronness cuts as a function of Estimated energy produced by flute. Right: Migration Matrix for the GC calculated by MC simulated events by *flute*. If there would be an unitary correspondance between the true energy and estimated energy, the migration matrix would be perfectly diagonal and in the graph above we would see just a line. However, due to the spillovers of events, for a fixed E_{true} some events might spill over to higher or lower energy and therefore the matrxi is not purely diagonal anymore.

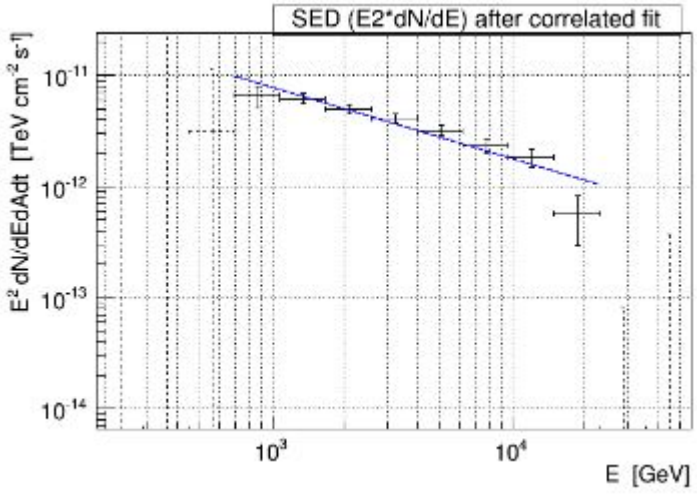

Figure 5.10: Spectral Energy Distribution of the GC.

will use a statistical approach based on the *Full likelihood* method, that takes better into account the features of the expected DM induced gamma-ray spectra. This is the subject of the following part of this chapter.

5.3 DM optimized analysis with the Full-Likelihood method

5.3.1 The J factor

The equation for the differential flux of gamma rays produced by annihilating dark matter (previously discussed in chapter 3, where s is the distance of the line of sight element to the observer)

$$\frac{\mathrm{d}\Phi_\gamma(,\mathrm{E},\Delta\Omega)}{\mathrm{dE}} = \frac{<\sigma v>}{2m_\chi^2}\frac{dN_\gamma}{dE}\frac{1}{4\pi}\int_{\Delta\Omega}\mathrm{d}\Omega\int_{\text{line of sight}}\rho^2_{\mathrm{DM}}(\mathrm{s},\Omega)\,\mathrm{ds} \tag{5.1}$$

can be written as follow, separating the particle physics component and the astrophysical component:

$$\frac{\mathrm{d}\Phi_\gamma(\mathrm{E},\Delta\Omega)}{\mathrm{dE}} = \underbrace{\frac{1}{4\pi}\frac{<\sigma v>}{2m_\chi^2}\frac{dN_\gamma}{dE}}_{\text{particle physics}}\cdot\underbrace{J(\Delta\Omega,\overrightarrow{n})\Delta\Omega}_{astrophysics} \tag{5.2}$$

where $\overrightarrow{n}$ is a particular observational direction along the solid angle $\Delta\Omega$ and $J(\Delta\Omega,\overrightarrow{n})$ is defined as follow:

$$J(\Delta\Omega,\overrightarrow{n}) = \frac{1}{\Delta\Omega}\int_{\Delta\Omega}\mathrm{d}\Omega\int_{\text{line of sight}}\rho^2_{\mathrm{DM}}(\mathrm{s},\Omega)\,\mathrm{ds} \tag{5.3}$$

expressed typically in units of $\mathrm{M}_\odot^2\,\mathrm{kpc}^{-5}$ or $\mathrm{GeV}^2\,\mathrm{cm}^{-5}$ for the annihilation case.

As can be seen, the J-factor depends on the chosen density profile. Using the public-code CLUMPY [22], that performs semi-analytical calculation of the J-factor for decaying/annihilating DM in the Galaxy, we obtained the Galactic Center DM density profiles for NFW and Einasto model and the corresponding J-factors. The obtained results can be seen in Figure 5.11. For this analysis we will use the NFW dark matter halo model for conciseness. If we had chosen the Einasto profile, our results would not have changed significantly, as we will discuss below.

5.3.2 Definition of the ROI

The first step is to define the *region of interest* (ROI) in order to maximize the discovery potential. The assumed halo profile needs to be taken into account together with the FoV of the instrument; in addition the inner Galactic halo is dominated by astrophysical sources described in Chapter 4 , such as the the diffuse emission, the Fermi Bubbles and the GC point source (that we actually detect in our analysis). In order to search for a DM signal, these astrophysical sources need to be removed from the search or to be carefully kept under consideration during the analysis, for instance by modelling them or defining a control region used to estimate the astrophysical background, the latter being our approach.

It would be ideal to choose a control region far from the barycentre where the contribution to the signal produced by DM annihilation is minimal in order to obtain a "pure" astrophysical background. This poses a problem since the GC halo is much more extended than the FoV of the MAGIC telescopes: the solution is to chose a ROI very close to the GC, where the DM

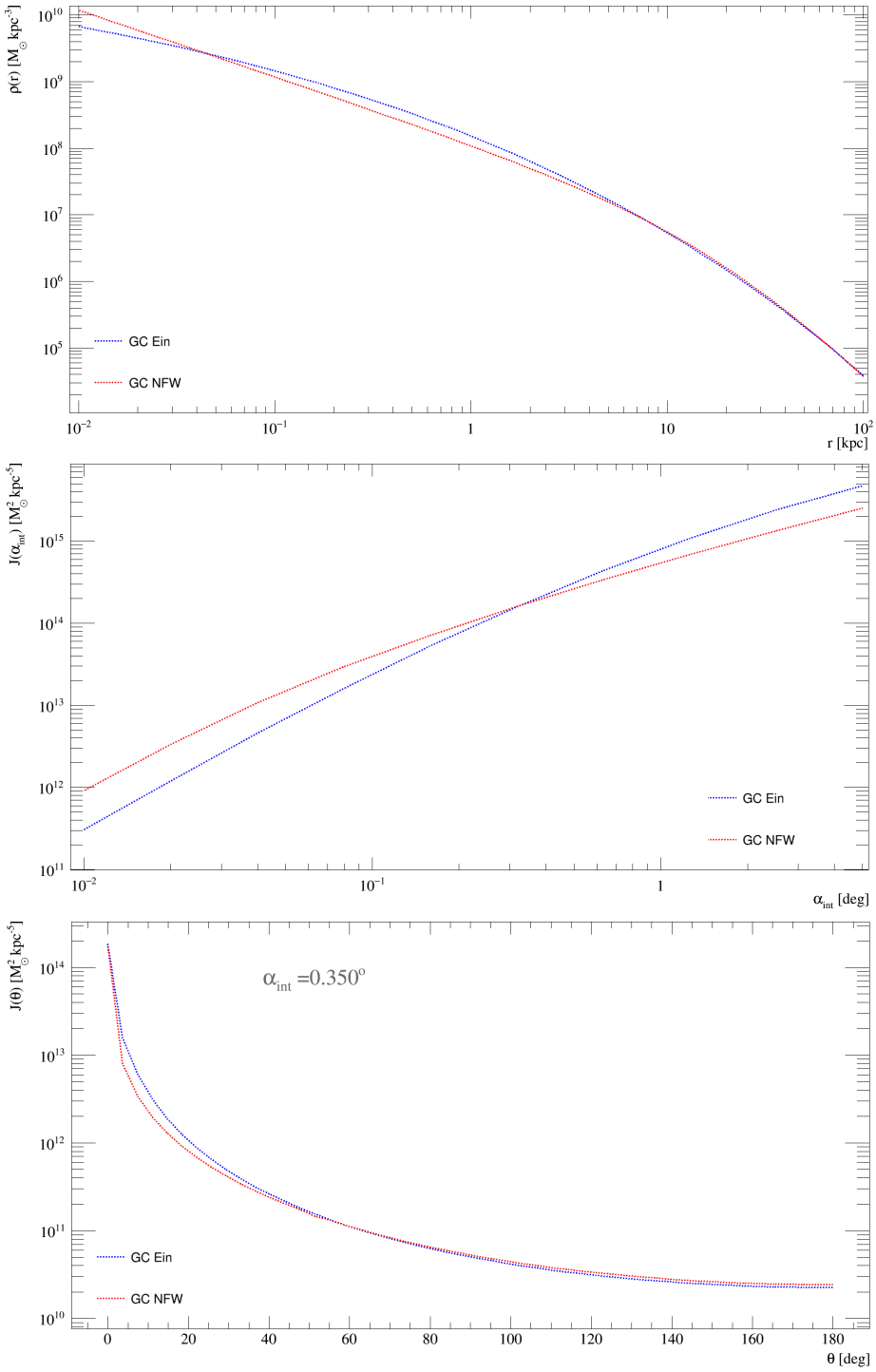

Figure 5.11: Density profiles and corresponding J-factors for GC obtained using CLUMPY, where the blu indicates the Einasto profile and the red the NFW profile. Top: density profiles of the DM halo; middle: J-factor as a function of the integration angle α_{int}; bottom: J-factor for a fixed integration angle $\alpha_{int} = 0.35^{o}$ as a function of the angular distance to the Galactic Centre.

density is putatively large and steeply falling with the galactocentric distance, and define the control region further away where the DM density is lower. With this definitions however,

the control region still includes a small DM signal, limiting the sensitivity of the search. The background is chosen from a control region corresponding to the Off region, which has an angular distance of 0.8º from the barycentre.

As previously said, the DM distribution is expected to be largest at the barycentre of the Galaxy, corresponding to the position of the GC point source. However, this is the place where we have a strong detection of astrophysical gamma rays from the central black hole. In principle, if this central emission would be known with good precision, it would be possible to search for DM gamma ray excess *on top* of this emission. However, the practical implementation of this solution in our version of the Full Likelihood method, still under development, was not possible given the time constraints of the thesis. Therefore we decided to cut-out the central region with angular distance θ_{min}<0.15° from the barycentre of the GC, that corresponds to more or less 1.5 times the telescope Point Spread Function. This guarantees that our sample is free from significant contamination from astrophysical sources, given that the diffuse contributions already discussed have quite hard spectra and low fluxes, and therefore absolutely irrelevant considering this region selection. A more sophisticated analysis, still under discussion, will encompass the full region and treat the GC excess as background in the Likelihood method.

The θ_{max} has been obtained by maximizing the *Q-factor* defined as follow

$$Q(\theta_{max}) = \frac{\int_0^{2\pi} \mathrm{d}\phi \int_0^{\theta_{\max}} \mathrm{d}\theta \mathrm{los}(\theta)\theta}{\sqrt{\int_0^{2\pi} \mathrm{d}\phi \int_0^{\theta_{\max}} \mathrm{d}\theta\, \theta}} \tag{5.4}$$

where los(θ) is the integral of the DM density square along the line of sight and θ and ϕ are the polar coordinates around the barycentre. The Q factor is basically proportional to the number of gamma events divided by the square root of the number of the background events, therefore its optimisation is analogue to the optimization of the Signal over Noise ratio. Our optimization lead to a $\theta_{max} = 0.35°$ as can be seen in Figure 5.12.

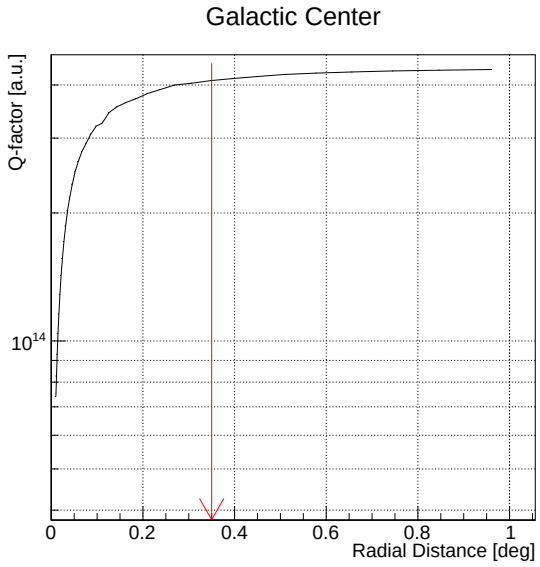

Figure 5.12: Q factor for the GC. The optimal value θ_{max} is indicated by the red line and coincides to the angular distance where the Q factor flattens.

Therefore our ROI is the region with 0.15°<θ<0.35°.

5.3.3 The Full Likelihood method

The Full Likelihood method is a MARS compatible code called MDM, which was discussed extensively in Ref. [12]. The Poisson Likelihood function is normally used in the analysis chain of IACT to detect a source by comparing the integrated number of events measure in the On region N_{on} to the number of events of the background region N_{off}. As N_{on} and N_{off} are both random variables that obey the Poisson statistics, the number of estimated gamma-ray and background events, respectively g and b, can be obtained by maximising the likelihood function so defined:

$$\mathcal{L}(g, b|N_{on}, N_{off}) = \frac{(g+b)^n}{n!} e^{-(g+b)} \times \frac{(\tau b)^m}{m!} e^{-\tau b} \tag{5.5}$$

where τ is the normalization factor between the search region and the control region. This approach works well for astrophysical sources, where simple power-law emission is observed, but since it does not discriminate between any spectral features, it is not optimal for the DM annihilation or decay spectra, which have a known shape (described in Chapter 3).

The Full Likelihood approach is optimized for DM searches by including in the likelihood analysis the well known DM spectral shape (for a given model and decay channel). The Full Likelihood function is so defined:

$$\begin{aligned}\mathcal{L}(s, b; E_1, \cdots, E_{N_{on}}, E_{N_{on}+1}, \cdots, E_{N_{on}+N_{off}}) = \frac{(g+b/\tau)^{N_{on}}}{N_{on}!} e^{-(g+b/\tau)} \times \frac{n^{N_{off}}}{N_{off}!} e^{-b} \\ \times \prod_{i=1}^{N_{on}} f(E_i|g, b) \times \prod_{i=1}^{N_{off}} g(E_i|b)\end{aligned} \tag{5.6}$$

where $f(E_i|s, b)$ and $g(E_i|b)$ are respectively the probability density functions for reconstructed energy of On and Off events, coming respectively from the signal region and the control region.
Practically, the control region is the "null hypothesis" i.e. there is no DM signal and the signal region, where the DM signal is expected to be measured, is the non-null hypothesis. Maximising the likelihood means maximising the probability that the null excess we observed is compatible with the DM signal for a given mass, J-factor and decay channel, keeping the parameter $< \sigma v >$ free. We obtain then the Upper Limits for the number of gamma rays produced by DM annihilation which corresponds to the Confidence Level [1]=95%, i.e. that the non-null hypothesis (DM signal) is verified 95% of the events and the null hypothesis (no DM signal i.e. no observed DM excess) is verified for the remaining 5% of the events.

In case of no-detection, this gives us upper limits on the number of signal events in the ROI, which we want to translate into upper limits to $< \sigma v >$. This is done again automatically by the MDM code, with the following steps. The differential gamma-ray flux is

$$\frac{\mathrm{d}\phi(\mathrm{E})}{\mathrm{dE}} = \frac{\mathrm{dg}}{\mathrm{dEdAdt}} \tag{5.7}$$

using the notation described above where g is the number of estimated gamma-ray events with true energy E. The expected number of signal events g for a steady source in a given

[1] When measuring a parameter, the observed value is always associated with a Confidence interval, which represents the range of values for the distribution parameter that are both reasonable and plausible; Upper Limits are one-sided intervals of Confidence intervals. Confidence Level is a statistical method for setting confidence intervals on parameters and such a method is defined to yield a $100(1-\alpha)\%$ CL if, when repeating the experiments many times, the resulting interval includes the true parameter at least $100(1-\alpha)\%$ of the time, independently of the value of the true parameter. Therefore at maximum $\alpha\%$ of the times the resulting interval does not include the true parameter.

observation time T_{eff} is the integral of 5.3.3 times the effective area (which since it depends on the energy remains inside the integral) times the observation time:

$$g = T_{eff} \int_0^\infty \mathrm{dE} \frac{\mathrm{d}\Phi(\mathrm{E})}{\mathrm{dE}} \mathrm{A_{eff}(E)} \tag{5.8}$$

The expected number of detected gamma rays above a certain value of the estimated energy E_{min} also depends on the energy dispersion function, which is the probability density function for the energy estimator, $G(E'; E)$, resulting in the following equation:

$$g(E'{>}E_{min}) = T_{eff} \int_{E_{min}}^\infty \int_0^\infty \mathrm{dE} \frac{\mathrm{d}\Phi(\mathrm{E})}{\mathrm{dE}} \mathrm{A_{eff}(E) G(E'; E)} \tag{5.9}$$

However, from Equation 5.3.1, we know the expression for the $\mathrm{d}\Phi(\mathrm{E})/\mathrm{dE}$ which, substituted in Equation 5.3.3 and expressing everything as a function of $< \sigma v >$, gives the follow:

$$< \sigma v > = g \times \frac{8\pi m_\chi^2}{J T_{eff} \int_{E_{min}}^\infty \int_0^\infty \mathrm{dN_\gamma} \frac{\mathrm{d}\Phi(\mathrm{E})}{\mathrm{dE}} \mathrm{A_{eff}(E) G(E'; E)}} \tag{5.10}$$

The necessary input for MDM are obtained through the MARS executables: the diffuse MC data need to be simulated for the ROI, *coach* has to be run to obtain the corresponding RF, which then have to be applied to *melibea* and in the end *flute* has to be run. Since the set of simulated MC are for 62<Zd<70 Zd our data are cut for the same Zd interval.

As can be seen from Equation 5.3.3, the following input are required:

- the energy list of the photons for the On and Off region, which have been extracted from melibea;
- the hadronness cuts to apply to the events, that have been extracted from flute;
- the effective collection area, obtained by flute **??** through MC simulations;
- the energy resolution and bias, corresponding to the probability density function for the energy estimator $G(E'; E)$, has been extracted from the migration matrix produced by flute;
- optimized τ, which is the normalization factor between the search region and the control region;
- the effective time;

The result can be seen in Figure 5.13 and will be extensively discussed in the next chapter.

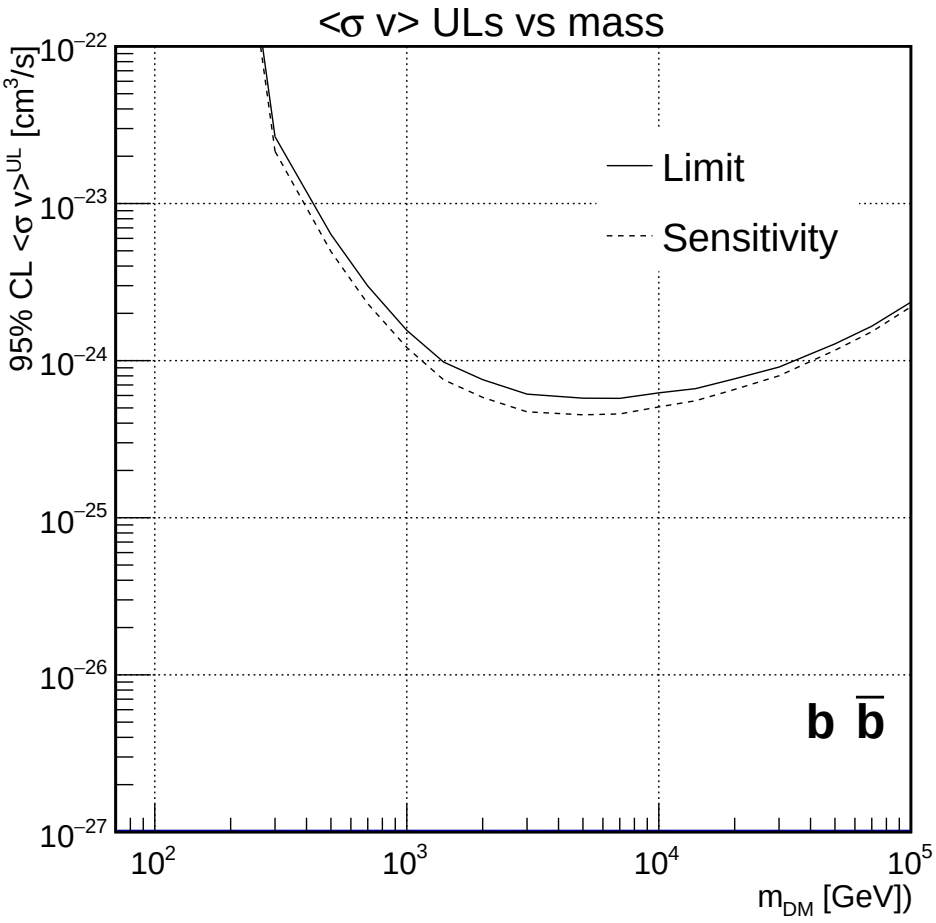

Figure 5.13: Upper limits for the velocity averaged dark matter self annihilation cross section with a 95% CL as obtained by this work.

Chapter 6

Results and Conclusions

> There are things known and there are things unknown, and in between are the doors of perception.
>
> Aldous Huxley

6.1 Results

Before analysing and comparing the results of this work, we will make a quick excursus on previous results by the Fermi-LAT and HESS instruments on the search for DM in the Galactic Centre.

The Fermi-LAT results on upper limits on the velocity averaged dark matter self annihilation cross section [**?**] were obtained by optimizing the ROI using a data-driven procedure that maximizes the S/N for the different dark matter density profiles and can be seen in Figure 6.1.

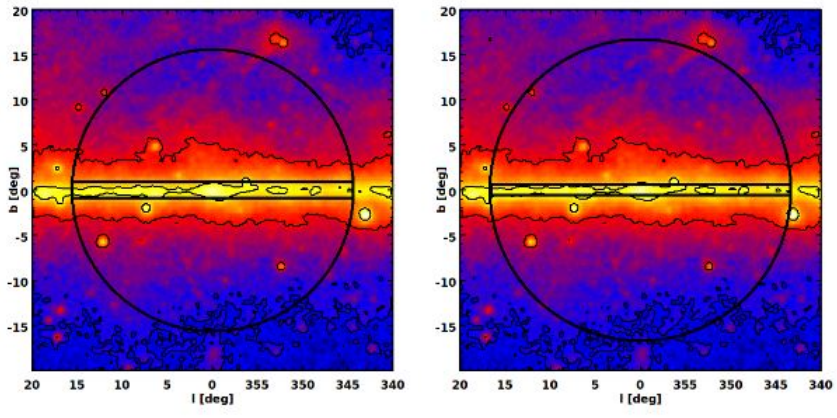

Figure 6.1: Maps of the observed gamma-ray flux in the energy range 1-100 GeV and of the optimized ROI for the Einasto (on the left) and NFW (on the right) dark matter profiles. The ROI corresponds to the region inside the circle excluding the Galactic plane. The color scale is logarithmic and the yellow, red and blue colours correspond respectively to 3.6×10^{-9},6.4×10^{-10} and 3.6×10^{-10}.

To obtain upper limits on the velocity averaged dark matter self annihilation cross section,

the integrated gamma-ray flux of the expected DM signal for each energy bin was required not to exceed the upper limit on the signal flux evaluated following the Bayesian procedure [**?**] and no background subtraction was performed. The results for a DM annihilation channel into $b\bar{b}$ is shown in Figure 6.2.

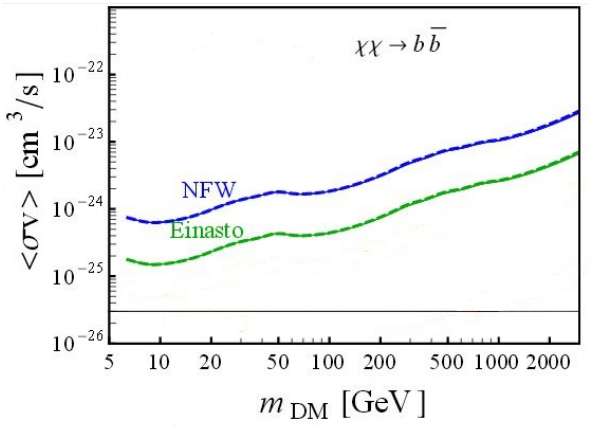

Figure 6.2: 3σ upper limits for $< \sigma v >$ of DM self annihilating into a $b\bar{b}$ decay channel for NFW and Einasto DM profiles.

The HESS analysis [**?**] was done using data from the years 2004-2008 for a total of 112 hours of observations; the maximum zenith angle is 30° with a mean of 14°. The signal region is defined with an angular distance θ<1.0°, excluding again the region corresponding to the Galactic plane with |b|<0.3°. The exact construction of the background region is explained in Figure 6.3.
Using a local DM density of $\rho_{loc} = 0.3\,\mathrm{GeV/cm^3}$ and a distance of the GC of $d_{GC} = 8.5$ kpc and cusped DM Einasto and NFW profiles, upper limits for the $< \sigma v >$ of annihilating DM where obtained, which can be seen in Figure 6.5.

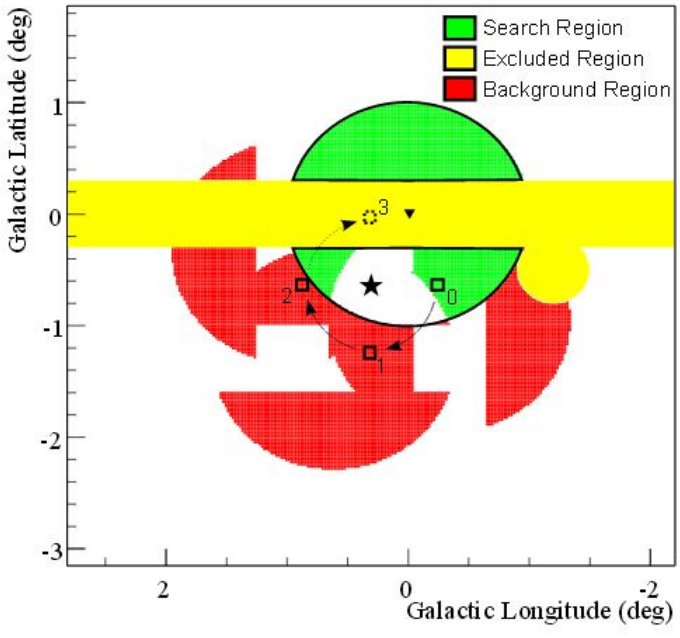

[H]

Figure 6.3: Signal and background region for a single telescope pointing position, showed as a star. The green area depicts the DM source region, with the exluded central region showed in yellow. In order to obtain similar gamma-ray detection efficiency in both the signal and background regions, for this given pointing position the background regions (in red) are obtained by rotating individual pixels of size $0.02° \times 0.02°$ belonging to the source region around the pointing position by 90°, 180° and 270°. For instance, with pixel 0 being in the source region, pixels 1 and 2 serves as background control regions, while pixel 3 is not used as its location corresponds to the excluded region. For this particular pointing position, the blank regions have not been considered in the analysis and correponds to pixels for which no background pixels could be constructed, due to the sovrapposition of the source and background/excluded regions.

With more recent results, the HESS-I array of four telescopes [**?**] observed the GC during the year 2010 using also the ON/OFF observation mode, for a total time of 9 hours and with the mean zenith angle of the observations 12°. The ON regions has a radius of 2° and centres at $l = 1°$ and $b = -0.7°$ in galactic coordinates and to avoid the detection of gamma rays from astrophysical sources, the galactic plane has been excluded (the central region with $|b|<0.3°$, as can be seen in Figure 6.4). Two background regions (OFF1 and OFF2) are defined symmetrically $\sim 8°$ away from the ON region, and the telescopes points consequently for 33 minutes to OFF1, the signal region and OFF2. The dark matter density profiles used are cored NFW and cored Einasto.

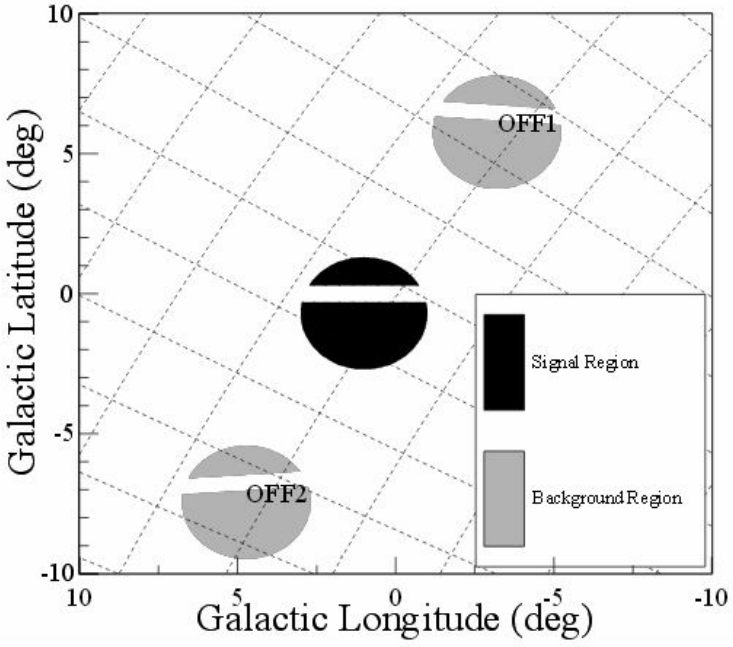

Figure 6.4: Representation of the signal and background regions for the HESS observations. The signal region is defined with a 2° radius excluding the central $|b|<0.3°$, corresponding diffuse emission from the Galactic plane. The two background regions are similarly defined, and situated symmetrically $\sim$ 8° away from the signal region. [**?**].

Using a likelihood method, they observed no gamma-ray excess and then obtained an upper limit for $< \sigma v >$ which can be observed in Figure 6.5.

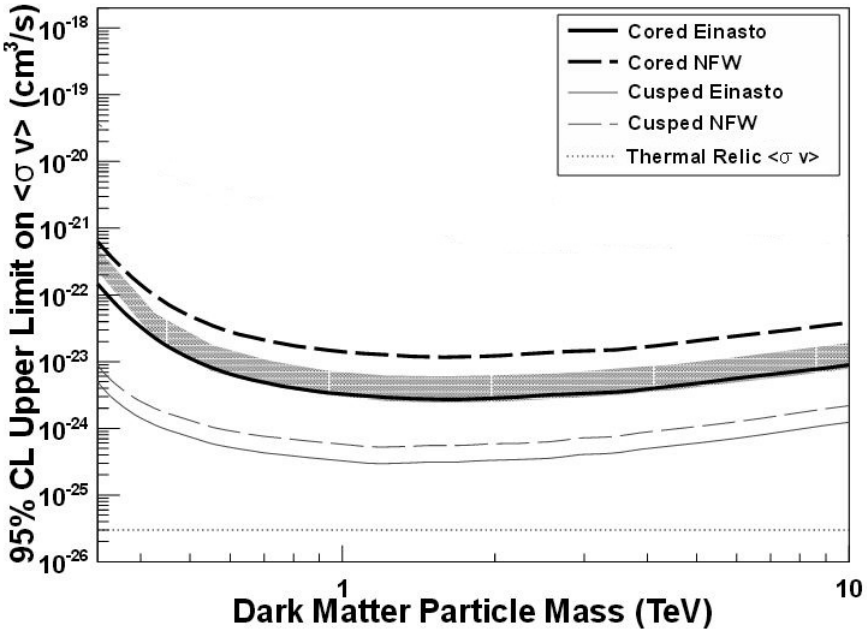

Figure 6.5: Upper limits for a 95% CL on the $< \sigma v >$ of self annihilating dark matter as a function of its mass. Both the HESS results for cored and cusped profiles are shown, and for comparison also the $< \sigma v >$ of a thermal relic DM is plotted.

With these introduction, we can start discussing our results, which are plotted in Figure 6.6 together with the Fermi-LAT and the HESS results (the former of the two analysis previously discussed).

For our analysis we considered a NFW dark matter halo profile; however this choice only

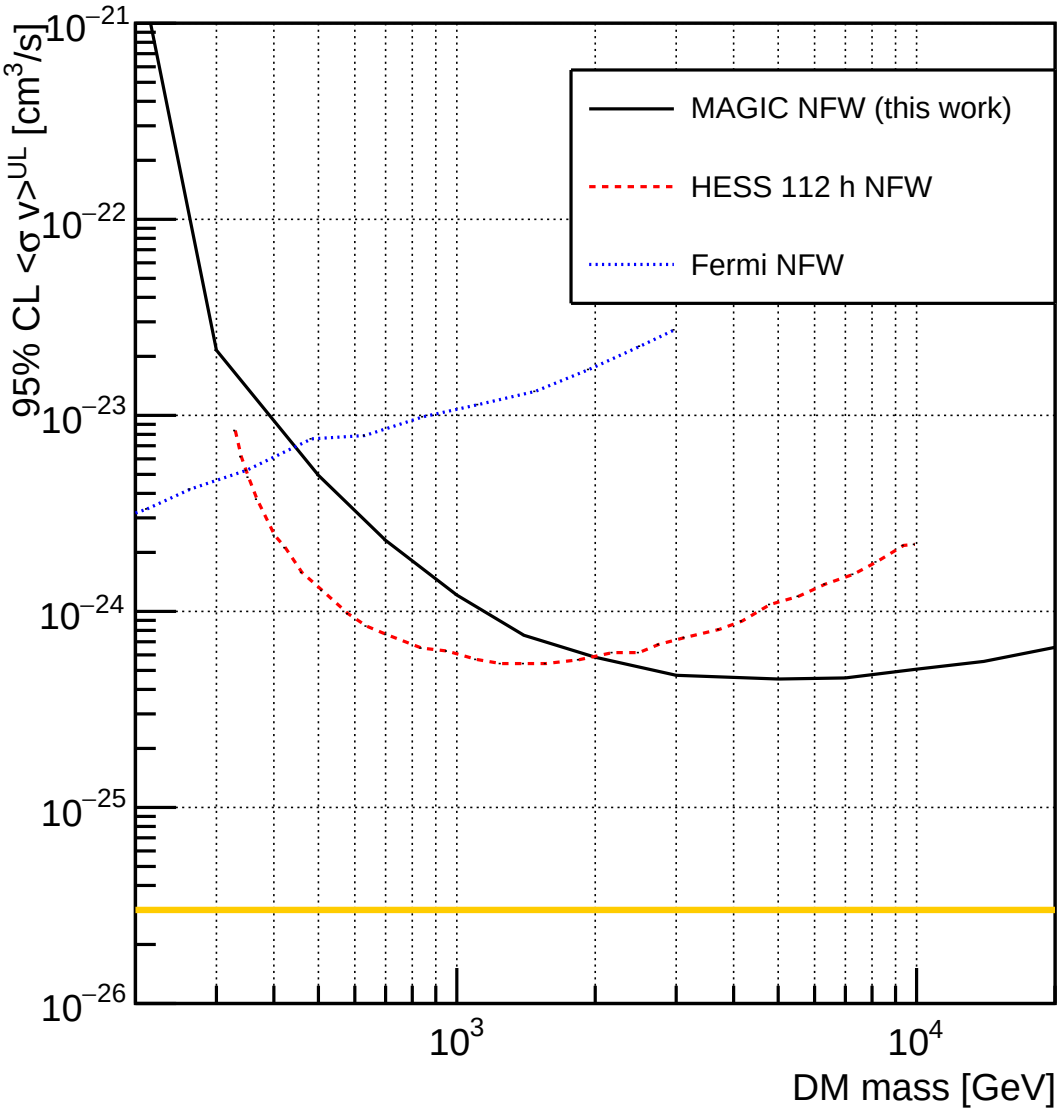

Figure 6.6: Upper limits on the velocity averaged dark matter self annihilation cross section for a $b\bar{b}$ decay channel with a 95% CL as obtained by this work, by the FERMI-Lat and by HESS. The orange line shows the thermal relic DM $< \sigma v >$ which corresponds to $3 \times 10^{-26}\,\mathrm{cm^3 s^{-1}}$.

minorly affect our results, since the J factor for the Einasto and NFW profiles differs at most by a factor two XXX. Also to keep in mind is that we considered dark matter annihilating purely into bottom and antibottom quarks, when realistically the annihilation has branching ratios into probably several other channels, as a combination of quark-antiquark pairs, gauge and Higgs bosons ($W^{\pm}$, Z, H) and charged leptons (e^+e^-, $\mu^+\mu^-$, $\tau^+\tau^-$). This choice is motivated by several reasons, and it has become somehow a customary way to show constraints on DM annihilation rate. The reasons are multiple: from one side, the annihilation channel into $b\bar{b}$ is actually probable when one performs branching ratios calculations on actual simulated MSSM DM particle. In addition, all quark channel have similar spectra than this one. Finally, using this choice, we can easily compare our results with other experiments. A thing that could not be possible, or straight forward, when using other channels, because the spectrum enter

the likelihood function, and therefore results from HESS and Fermi-LAT cannot be easily rescaled.

As one can see from the Figure 6.6, Fermi-LAT results are the most constraining at low DM mass. This is due to the intrinsic difference of instruments like satellite pair-conversion experiments, that are statistically limited at energies above few hundreds of GeV, where instead ground-based Cherenkov telescopes are optimally sensitive. The low DM mass region is therefore better sampled by Fermi-LAT. Moving to higher energies, the HESS results are the most constraining because of the advantageous position of the HESS telescopes combined with a large sensitivity of an array of four telescopes: since they are situated in Namibia, in the Southern Hemisphere, they observe the GC at low zenith angles and therefore the window for observation is longer during the year, as well as the observations can guarantee the lowest energy threshold, thus harvesting more photons from the source by integration a large energy range. In addition, the HESS data encompass 112 hours of observation, almost twice as much as the hours of this work. Moreover, due to the larger FoV of the HESS telescopes, the background control region was defined further away from the GC, where the DM density profiles decreased resulting in a less contamination of DM signal.

Finally, we notice that our results are instead more constraining above 2 TeV, that is for DM masses larger than that. This results comes from the very good performance of ground-based Cherenkov telescopes for high energies when observation are performed at high zenith angle. To our knowledge, these results are the best achieved at the galactic center above 2 TeV.

Despite the promising results, we highlight here that these are preliminary, and need still careful checks and integration. The purpose of this work was to tune the full likelihood reconstruction technique with MAGIC data.

The advent of CTA promises even more restraining results on the DM searches at the Galactic Centre, reaching a sensitivity up to the thermal relic predicted cross section, adding a new piece to the puzzle of DM searches at GC.

6.2 Conclusions

A search for a gamma-ray signal from DM annihilations coming from the Galactic Centre was conducted using MAGIC data in the period from 2013-2014. The region with angular distance $0.15° < \theta < 0.35°$ was chosen for the search, therefore excluding the central GC point source, and the control region was situated at an angular distance of $\theta = 0.8°$. Using a NFW dark matter halo profile, no significant signal was found, therefore we used a likelihood function which included in the analysis procedure the DM annihilation spectrum. By taking advantage of the distinct features expected in the gamma-ray spectrum of DM origin, a better sensitivity was achieved than the more general Poisson likelihood approach. We therefore obtained upper limits on the flux produced by annihilating DM into $b\bar{b}$ pairs which were translated into upper limits on the velocity-weighted DM annihilation cross-section $< \sigma v >$. A more realistic annihilating DM would produces various particles, as quarks-antiquarks and leptons; however. Our results were more constraining than the HESS results above 2 TeV, corresponding to $< \sigma v > \sim 6 \times 10^{-25}$, although the HESS telescopes, situated in the Southern Hemisphere, can observe the GC at lower Zenith angles for more hours.
The next goal is a more complex analysis of the Galactic Centre, including all the available data and different annihilation channels for a more realistic approach. This future analysis will also involve an implementation of the full likelihood function in order to include also the central region with angular distance $\theta < 0.15°$ from the barycenter of the GC in the search

region for DM annihilation signal.

Appendix A

The Fermi-LAT

Originally called Gamma-Ray Large Area SPace Telescope(GLAST), the instrument was later renamed Fermi-LAT, Large Area Telescope, in honour of the physicist Enrico Fermi and it was launched in orbit in 2008 and still operating nowadays. It is an imaging high energy gamma-ray telescope, operating in the energy range between 20 MeV and 300 GeV, with a wide field of view of about 60° around its axis.
As can be seen in Figure A.1, the incident radiation pass first through an anticoincidence shield detector, then trough conversion foils, thin layers of high atomic number atomi: near their strong electromagnetic field, the photons pair produce protons and electrons which continue moving in the direction of the incident gamma-ray, since their rest mass is smaller than the gamma ray energy. Their paths are measured by particle tracking detectors and their energies are measured by a calorimeter. The electrons and positrons then produce electromagnetic showers in the calorimeter.
The anticoincidence detector consists of scintillator tiles and is used to discriminate between cosmic rays and gammas, since it produces a flash of light when charged particles pass through.

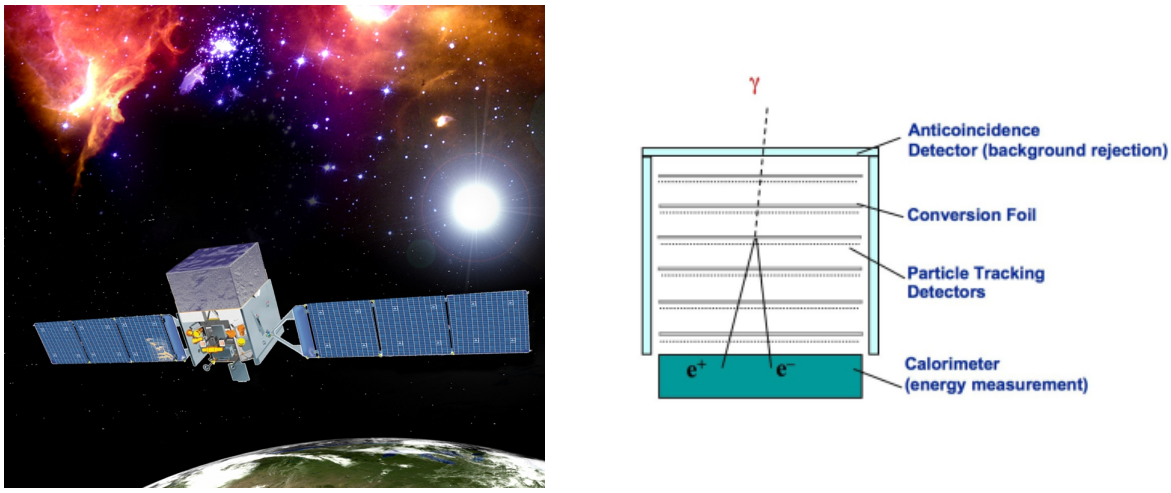

Figure A.1: Left: representation of the Fermi-LAT. Right: schematic strucuture of the LAT.

The output data are produced as charged particles in the shower deposit their energy in the tracker and calorimeter and consist of pulsed signal; reconstructing the path of the particle and the energy loss, the energy and direction of the original gamma ray can be obtained.

Appendix B

Cherenkov emission

The secondary particles produced in the cascades emit Cherenkov radiation: the Cherenkov radiation is named after the russian scientis Pavel Alekseyevich Cherenkov who discovered it in 1934 and later, for this discovery, received the Nobel prize in physics in 1958 with Ilya Frank and Igor Iamm.

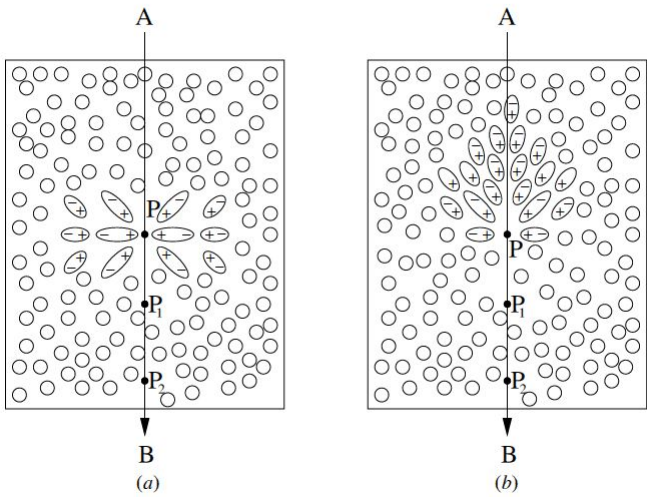

Figure B.1: The local polarization produced in a medium during the passage of a particle; on the left the case where the velocity of the particle is $v < c/n$, on the right where the velocity of the particle is $v > c/n$. [75]

This radiation occurs when a charged particle travels in a dielectric medium: it affects the molecules causing re orientation of the dieltric dipoles. As can be seen in figure B.1, if the particle moves slowly ($v < c/n$ where c/n is the velocity of light in the medium with index n) the disturbance is symmetrical around and along the direction of the moving particle, so that there is no residual electric field and no emission. If instead $v > c/n$, the particle is moving faster than the electromagnetic wave induced by the polarization itself, , giving rise to a varying electric dipole momentum along the direction of the particle. As a consequence a coherent wave front is emitted (Cherenkov emission) in a beamed cone centered along the direction of the moving particle of angle

$$\cos\theta = 1/(\beta n) \tag{B.1}$$

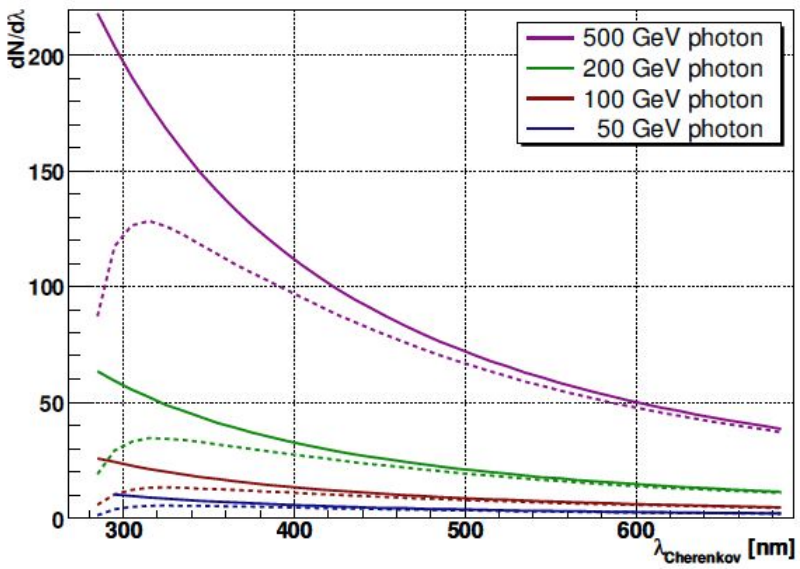

Figure B.2: Spectra of the Cherenkov radiation produced by gamma-ray induced extensive air showe at 10 km a.s.l. (solid line) and at 2200 m a.s.l., after the absorption mechanism lead to strong spectral extinction at lower wavelenght.

This identifies a velocity threshold where $\beta_{th} = 1/n$ and the corresponding energy threshold

$$E_{th} = \frac{m_0 c_0^2}{\sqrt{1 - \beta_{th}^{-2}}} = \frac{m_0 c_0^2}{\sqrt{1 - n^{-2}}} \tag{B.2}$$

where m_0 is the rest mass of the moving particle. The number of Cherenkov photons emitted by a charged particle with atomic number Z per wavelength λ and per path length is equal to:

$$\frac{\mathrm{dN}}{\mathrm{dx d}\lambda} = \frac{2\pi\alpha Z^2}{\lambda^2}\left(1 - \frac{1}{\beta^2 n^2(\lambda)}\right) \tag{B.3}$$

where α is the fine structure constant.
Because of this inverse squared dependency on the wavelength of the Cherenkov photons, the maximum emission is expected at shorter wavelength (UV band) and then decreasing as the wavelength decreases. However, due to absorption mechanisms in the atmosphere, such as Mie and Rayleigh scattering and the absorption by the ozone molecules, the spectrum is modified, showing a peak at UV wavelenght as can be seen in Figure B.2

Appendix C

The DISP extimation

The DISP parameter (Distance between the Image centroid (i.e. the image center of gravity) and the Source Position (i.e. the point of the camera corresponding to the direction of the incoming shower) as can be seen in Figure C.1 and is used to reconstruct the arrival direction of the incident gamma ray.

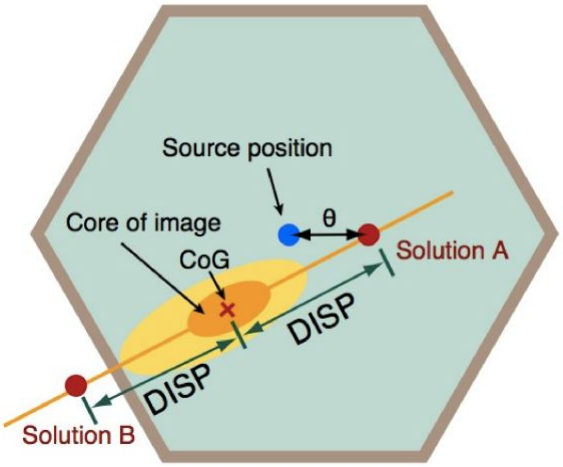

Figure C.1: Sketch of the DISP parameter on the camera, showing the *ghost-busting*: two possible solutions for this parameter are possible, and as a consequence two opposite arrival directions. To minimize the error on the arrival directions, stereo observations are necessary.

If only one telescope is used for the observations, there is a right-left ambiguity, called *ghost-busting*: since it is difficult to discriminate between which incident photons are coming from the head or the tail of the shower, there are two possible solutions for the DISP parameter respect to the centre of gravity of the image on the camera.
With stereo observations, this problem is solved, as can be seen in Figure :after obtaining four possible source positions, the one with the smallest distance and the closest to the intersection of the axes of the two ellipses is chosen. The events to badly reconstructed are excluded, and this also improves the gamma-hadron discrimination, since the hadronic showers produces spread images where it is difficult to identify both the center of gravity and the major axis.

Appendix D

Effective collection Area

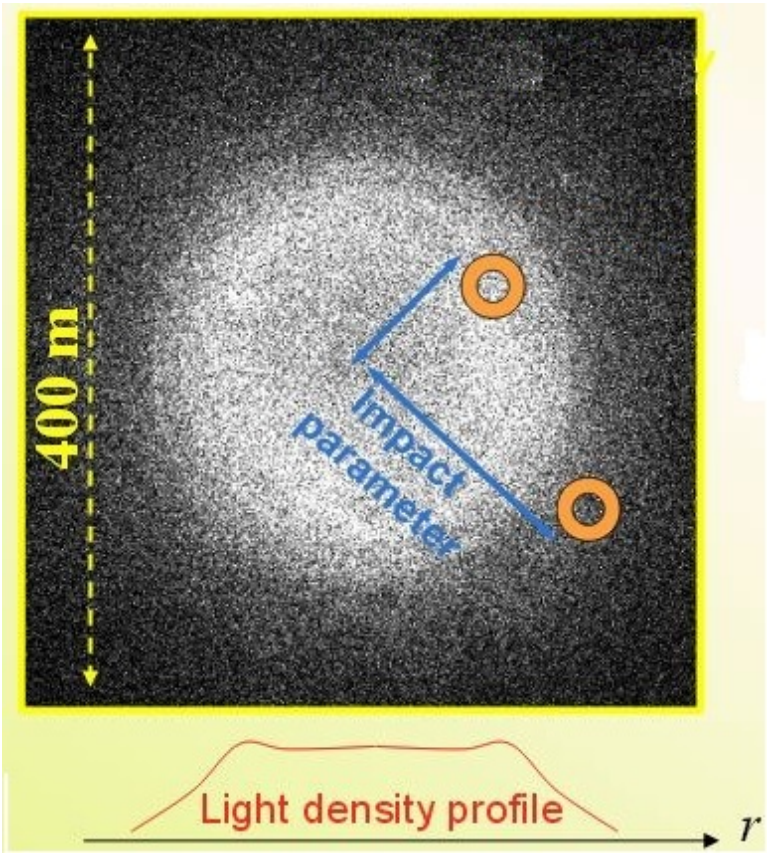

Figure D.1: Top: ground light density, which for a 100 GeV photons is $< 10\text{photons/m}^2$: the bright central circle is the lightpool and the orange rings represent the telescopes in case of a stereoscopic system; the impact parameter is then the distance between the location of the telescope and the center of the lightpool. If the impact parameter is bigger than the radius of the lightpool ($\sim$ 120 meters) the probability to detect the shower is null. Bottom: light density profile of the lightpool.

To first approximation the geometrical area can be described as the mirror surface of the telescope that images the shower, but there's actually much more beyond it: the effective collection area is connected to the detection probability $P_\gamma(E, r, \theta)$ which depends on the energy and zenith angle of the gamma ray and on the impact parameter, which is the distance of the telescope to the center of the lightpool. The flux observed by the telescope depends on the detection probability and on the flux of the gamma source:

$$\frac{\mathrm{dN}_\gamma}{\mathrm{dE}} = \int_\phi \int_r P_\gamma(E, r, \theta)\Phi(E, \theta) r \mathrm{dr} = 2\pi \int_\mathrm{r} \mathrm{P}_\gamma(\mathrm{E}, \mathrm{r}, \theta)\Phi(\mathrm{E}, \theta)\mathrm{rdr} \tag{D.1}$$

The *Effective Collection Area* is then defined as

$$A_{eff}(E,\theta) = 2\pi \int_r P_\gamma(E,r,\theta) r \mathrm{dr} = \int_{-\infty}^{+\infty} \int_{-\infty}^{+\infty} \mathrm{P}_\gamma(\mathrm{E},\mathrm{x},\mathrm{y},\theta)\mathrm{dxdy} \tag{D.2}$$

where x and y are the plane coordinate of the cherenkov lightpool and r is the radial distance. So the observed flux results to be

$$\frac{\mathrm{dN}_\gamma}{\mathrm{dEdt}} = A_{eff} \frac{\mathrm{d}\Phi(\mathrm{E},\theta)}{\mathrm{dt}} \tag{D.3}$$

If the detection probability would be strictly either 1 or 0, the energy as a function of this probability would assume the shape of a step function, as can be seen here on the right and the Energy threshold would be the value of the energy for which the detection probability shifts from the zero value to the unity value.

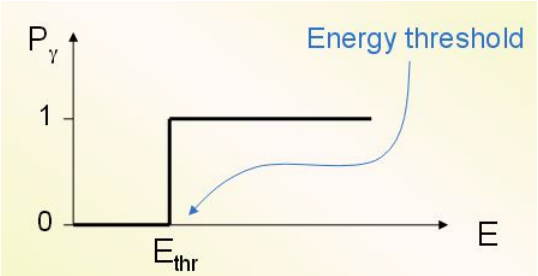

But since the probability assumes continuous values from 0 to 1, the effective collection area has a more curvous shape which can be seen in Figure D.2.

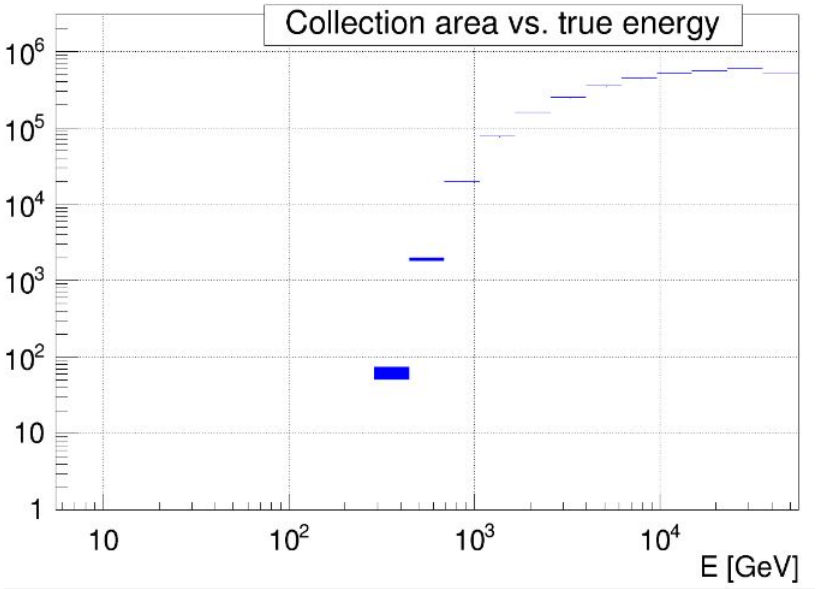

Figure D.2: Dependence of effective area from the energy for the GC obtaind through simulation: it shows a more smooth behaviour than the step function. The Energy Threshold is of the order of hundreds of GeV because of the high Zd angle condition of observation-

Practically, the effective area is calculated through Monte Carlo simulations. Starting from EquationD, we can write

$$P_\gamma(E,x,y,\theta) = \frac{N_{\gamma,final}(x,y)}{N_{\gamma,sim}(x,y)} \tag{D.4}$$

where the $N_{\gamma,sim}(x,y)$ are the number of gamma rays uniformly simulated in an area A_{MC}. Since $N_{\gamma,sim}(x,y) = N_{\gamma,sim}/A_{MC}$ and $N_{\gamma,final} = \int_{-\infty}^{+\infty}\int_{-\infty}^{+\infty} N_{\gamma,final}(x,y)$dxdy, substituting everything in Equation D, we obtain

$$A_{eff} = \frac{N_{\gamma,final}}{N_{\gamma,sim}} A_{MC} \tag{D.5}$$

so the effective area is the area where the MC rays are generated times the global efficiency, which is the ratio of the number of observed gamma rays over the number of simulated gamma rays.
However, because of the dependences held in the probability $P_\gamma(E,x,y,\theta)$, also the effective area depends on the energy of the gamma ray, on its direction (Zd and Az) and on the angle between its direction and the telescope axis. Therefore the effective area has to be calculated in bins of these values. The effective area also depends on the selection cuts applied to the data, for instance from the cuts applied to reduce the background.

At first approximation, the distance to the shower core scales as $\cos\theta_{Zd}$, where θ_{Zd} is the Zenith distance; as a consequence the light flux density on the ground scales as $\cos^2\theta_{Zd}$ and the effective area as the inverse of the flux, i.e. as $\cos^{-2}\theta_{Zd}$.

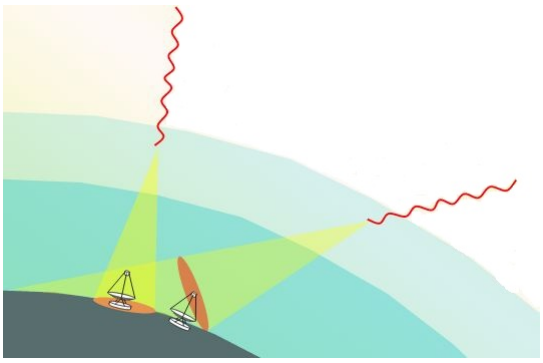

Therefore, as can be seen in Figure D.3, for low Zd, the light pool is smaller, the distance to the shower core is smaller, and the flux photon density is higher since the light is less absorbed, which leads to a lower energy threshold. On the opposite, for high Zd, the light pool is broader, the distance to the shower core is bigger leading to a smaller photon density and a higher energy threshold.

Although for high Zd the effective area is bigger, which apparently seems an advantage, things are more complicated: due to the smaller flux density, the reconstruction of events are trickier. In addition, since the shower is further away, the shower images are smaller on the camera, and analysis is more challenging due to the less powerful background suppression.

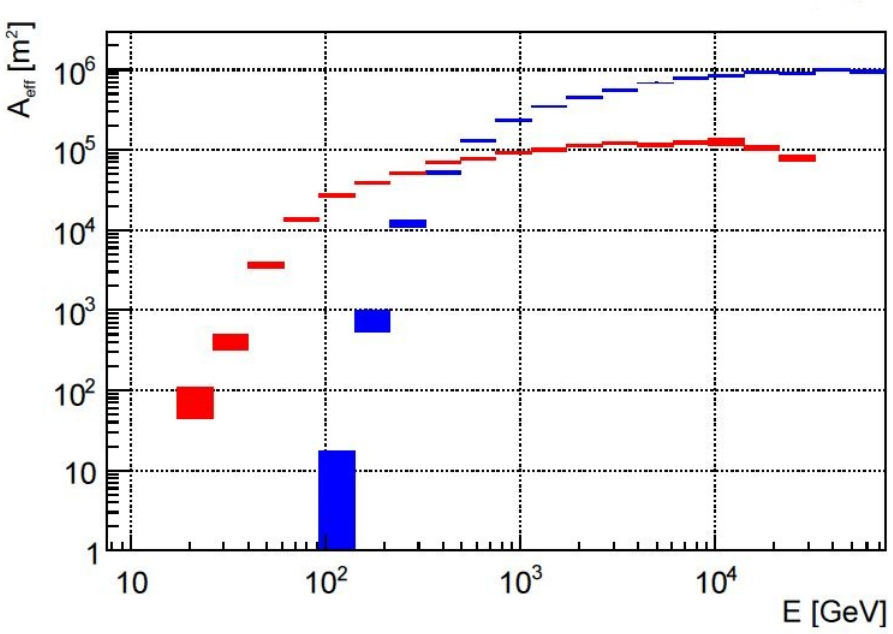

Figure D.3: Dependence of effective area from the energy: the red shows the Zd range $5^o - 35^o$ for the Crap Nebula and the blue shows the $58^o - 70^o$ Zd range for the GC. [39].

Bibliography

[1] F. A. Aharonian and S. V. Bogovalov. Exploring physics of rotation powered pulsars with sub-10 GeV imaging atmospheric Cherenkov telescopes. *New Astronomy*, 8:85–103, February 2003.

[2] Georges Aad et al. Search for new phenomena in final states with an energetic jet and large missing transverse momentum in pp collisions at $\sqrt{s} = 8$ TeV with the ATLAS detector. 2015.

[3] A. A. Abdo and Fermi LAT Collaboration. Detection of Gamma-Ray Emission from the Starburst Galaxies M82 and NGC 253 with the Large Area Telescope on Fermi. *The Astrophysical Journal*, 709:L152–L157, February 2010.

[4] F. Acero. Localising the VHE gamma-ray source at the Galactic Centre. *Mon. Not. Roy. Astron. Soc.*, 402:1877–1882, 2010.

[5] M. Ackermann et al. The Spectrum and Morphology of the Fermi Bubbles. *Astrophys.J.*, 2014.

[6] P.A.R. Ade et al. Planck 2015 results. XIII. Cosmological parameters. 2015.

[7] F. Aharonian and F. Aharonian. Spectrum and variability of the Galactic Center VHE gamma-ray source HESS J1745-290. *Astron. Astrophys.*, 503:817, 2009.

[8] F. Aharonian et al. Very high-energy gamma rays from the direction of Sagittarius A*. *Astron. Astrophys.*, 425:L13–L17, 2004.

[9] F. Aharonian et al. H.E.S.S. observations of the Galactic Center region and their possible dark matter interpretation. *Phys. Rev. Lett.*, 97:221102, 2006. [Erratum: Phys. Rev. Lett.97,249901(2006)].

[10] J. Albert et al. Implementation of the Random Forest Method for the Imaging Atmospheric Cherenkov Telescope MAGIC. *Nucl. Instrum. Meth.*, A588:424–432, 2008.

[11] J. Aleksic et al. The major upgrade of the MAGIC telescopes, Part I: The hardware improvements and the commissioning of the system. 2014.

[12] J. Aleksic, J. Rico, and M. Martinez. Optimized analysis method for indirect dark matter searches with Imaging Air Cherenkov Telescopes. *JCAP*, 1210:032, 2012.

[13] W. B. Atwood, A. A. Abdo, M. Ackermann, W. Althouse, B. Anderson, M. Axelsson, L. Baldini, J. Ballet, D. L. Band, G. Barbiellini, and et al. The Large Area Telescope on the Fermi Gamma-Ray Space Telescope Mission. , 697:1071–1102, June 2009.

[14] A. Ballone, M. Schartmann, A. Burkert, S. Gillessen, R. Genzel, T. K. Fritz, F. Eisenhauer, O. Pfuhl, and T. Ott. Hydrodynamical Simulations of a Compact Source Scenario for the Galactic Center Cloud G2. *The Astrophysical Journal*, 776, October 2013.

[15] Gianfranco Bertone, Dan Hooper, and Joseph Silk. Particle dark matter: Evidence, candidates and constraints. *Phys.Rept.*, 405:279–390, 2005.

[16] Geoffrey C. Bower, Sera Markoff, Jason Dexter, Mark A. Gurwell, James M. Moran, et al. Radio and Millimeter Monitoring of Sgr A*: Spectrum, Variability, and Constraints on the G2 Encounter. 2015.

[17] T. Bretz, D. Dorner, R. M. Wagner, and P. Sawallisch. The drive system of the Major Atmospheric Gamma-ray Imaging Cherenkov Telescope. *Astropart. Phys.*, 31:92–101, 2009.

[18] A. Bulgarelli, V. Fioretti, A. Zoli, Aboudan, and CTA Consortium. The On-Site Analysis of the Cherenkov Telescope Array. *ArXiv e-prints*, September 2015.

[19] Andreas Burkert, Mark Schartmann, Christian Alig, Stefan Gillessen, Reinhard Genzel, et al. Physics of the Galactic Center Cloud G2, on its Way towards the Super-Massive Black Hole. *Astrophys.J.*, 750:58, 2012.

[20] R. Catena and P. Ullio. A novel determination of the local dark matter density. , 8:4, August 2010.

[21] J.A.R. Cembranos, V. Gammaldi, and A.L. Maroto. Spectral Study of the HESS J1745-290 Gamma-Ray Source as Dark Matter Signal. *JCAP*, 1304:051, 2013.

[22] A. Charbonnier, C. Combet, and D. Maurin. CLUMPY: a code for gamma-ray signals from dark matter structures. *Comput. Phys. Commun.*, 183:656–668, 2012.

[23] M. Chernyakova, D. Malyshev, F. A. Aharonian, R. M. Crocker, and D. I. Jones. The high-energy, Arcminute-scale galactic center gamma-ray source. *Astrophys. J.*, 726:60, 2011.

[24] Maca Clavel, R. Terrier, A. Goldwurm, M.R. Morris, G. Ponti, et al. The reflection of two past outbursts of Sagittarius A* observed by Chandra during the last decade. *IAU Symp.*, 303:344–348, 2014.

[25] Douglas Clowe, Marusa Bradac, Anthony H. Gonzalez, Maxim Markevitch, Scott W. Randall, et al. A direct empirical proof of the existence of dark matter. *Astrophys.J.*, 648:L109–L113, 2006.

[26] MAGIC collaboration. Mars data analysis manual, 2015.

[27] MAGIC collaboration. Position reconstruction Theory , 2015. http://wiki.magic.pic.es.

[28] VERITAS collaboration. Veritas, 2015. http://veritas.sao.arizona.edu/.

[29] HESS collabotration. HESS, 2015. http://www.mpi-hd.mpg.de/hfm/HESS/.

[30] Roland M. Crocker, Geoffrey V. Bicknell, Andrew M. Taylor, and Ettore Carretti. Giant Shocks in the Fermi Bubbles and the Origin of the Microwave Haze. 2014.

[31] Patrick Crumley and Pawan Kumar. Radio Emission from the Bow Shock of G2. *IAU Symp.*, 303:312–314, 2014.

[32] W.J.G. de Blok. The Core-Cusp Problem. *Advances in Astronomy*, 2010:5, 2010.

[33] Guillaume Dubus. Gamma-ray binaries and related systems. *Astron.Astrophys.Rev.*, 21:64, 2013.

[34] A. Eckart and R Genzel. Stellar proper motions in the central 0.1 PC of the Galaxy. *MNRAS*, 284:576–598, January 1997.

[35] ESO. Best View Yet of Dusty Cloud Passing Galactic Centre Black Hole , 2015. http://www.eso.org/public/news/eso1512/.

[36] Marco Fatuzzo and Fulvio Melia. Diffusive Cosmic-ray Acceleration in Sagittarius A*. 2012.

[37] Fermi-LAT. High-Energy Gamma-Ray Emission From Solar Flares: Summary of Fermi LAT Detections and Analysis of Two M-Class Flares. 2013.

[38] G. J. Fishman, P. N. Bhat, R. Mallozzi, J. M. Horack, T. Koshut, C. Kouveliotou, G. N. Pendleton, C. A. Meegan, R. B. Wilson, W. S. Paciesas, S. J. Goodman, and H. J. Christian. Discovery of Intense Gamma-Ray Flashes of Atmospheric Origin. *Science*, 264:1313–1316, May 1994.

[39] Christian Fruck. The galactic center resolved with magic and a new technique for atmospheric calibration, 2015. PhD Thesis.

[40] J. R. Garca, F. Dazzi, D. Hfner, D. Herranz, M. Lpez, M. Mariotti, R. Mirzoyan, D. Nakajima, T. Schweizer, and M. Teshima. Status of the new Sum-Trigger system for the MAGIC telescopes. In *Proceedings, 33rd International Cosmic Ray Conference (ICRC2013)*, 2014.

[41] S. Gillessen, R. Genzel, T.K. Fritz, E. Quataert, C. Alig, A. Burkert, J. Cuadra, F. Eisenhauer, O. Pfuhl, K. Dodds-Eden, C. F. Gammie, and T. Ott. A gas cloud on its way towards the supermassive black hole at the Galactic Centre. *Nature*, 481:51–54, January 2012.

[42] Stefan Gillessen, Reinhard Genzel, Tobias K Fritz, Frank Eisenhauer, Oliver Pfuhl, et al. Pericenter passage of the gas cloud G2 in the Galactic Center. *Astrophys.J.*, 774:44, 2013.

[43] Lisa Goodenough and Dan Hooper. Possible Evidence For Dark Matter Annihilation In The Inner Milky Way From The Fermi Gamma Ray Space Telescope. 2009.

[44] W. Miller Goss, Robert L. Brown, and K.Y. Lo. The discovery of sgr a*. 2003.

[45] Yi-Qing Guo, Qiang Yuan, Cheng Liu, and Ai-Feng Li. Hybrid model of GeV-TeV gamma ray emission from Galactic Center. *J.Phys.*, G40:065201, 2013.

[46] U. S. Inan, M. B. Cohen, R. K. Said, D. M. Smith, and L. I. Lopez. Terrestrial gamma ray flashes and lightning discharges. *Geophysical Research Letters*, 33(18):n/a–n/a, 2006.

[47] M. Kachelriess. Lecture notes on high energy cosmic rays. 2008.

[48] N.E. Kassim, T.N. Larosa, T.J.W. Lazio, and S.D. Hyman. *Wide Field Radio Imaging of the Galactic Center*, volume 186 of *Astronomical Society of the Pacific Conference Series*. June 1999.

[49] Eduard P. Kontar, A. Gordon Emslie, Anna Maria Massone, Michele Piana, John C. Brown, et al. Electron-Electron Bremsstrahlung Emission and the Inference of Electron Flux Spectra in Solar Flares. *Astrophys.J.*, 670:857, 2007.

[50] K. Kosack et al. TeV gamma-ray observations of the galactic center. *Astrophys. J.*, 608:L97–L100, 2004.

[51] M. Kuhlen. The Dark Matter Annihilation Signal from Dwarf Galaxies and Subhalos. *Advances in Astronomy*, 2010:45, 2010.

[52] D. Kunneriath, A. Eckart, S.N. Vogel, P. Teuben, K. Muzic, et al. The Galactic centre mini-spiral in the mm-regime. *Astron.Astrophys.*, 538:A127, 2012.

[53] Masaaki Kusunose and Fumio Takahara. A Leptonic Model of Steady High-Energy Gamma-Ray Emission from Sgr A*. *Astrophys. J.*, 748:34, 2012.

[54] Martin Lopez-Corredoira, A. Cabrera-Lavers, T.J. Mahoney, P.L. Hammersley, F. Garzon, et al. The Long Bar in the Milky Way. Corroboration of an old hypothesis. *Astron.J.*, 133:154–161, 2007.

[55] Y. Maeda, F.K. Baganoff, E.D. Feigelson, M. Morris, M.W. Bautz, et al. A chandra study of sgr a east: a supernova remnant regulating the activity of our galactic center? *Astrophys.J.*, 570:671, 2002.

[56] Stephen Serjeant Mark H. Jones, Robert J.A. Lambourne. *An Introduction to Galaxies and Cosmology*. Cambridge University Press, 2015.

[57] M.S.Longair. *High Energy Astrophysics Vol 1*. Cambridge University Press, 1992.

[58] NASA. NASAs Chandra Detects Record-Breaking Outburst from Milky Ways Black Hole , 2015. http://www.nasa.gov/press/2015/january/nasa-s-chandra-detects-record-breaking-outburst-from-milky-way-s-black-hole/.VRKze-HHh5B.

[59] J.F. Navarro, C.S. Frenk, and S.D.M. White. The Structure of Cold Dark Matter Halos. *Astrophisical Journal*, 462:563, May 1996.

[60] F. Nesti and P. Salucci. The Local Dark Matter Density. *ArXiv e-prints*, December 2012.

[61] Karlsruhe Institute of Technology. CORSIKA an Air Shower Simulation Program, 2015. http://www.ikp.kit.edu/corsika/.

[62] Joel R. Primack and Michael A.K. Gross. Hot dark matter in cosmology. 2000.

[63] WOlfendale A.W. Ramana Murthy P.V. *Gamma-ray astronomy*. Cambridge Astrophysics Series, 1993.

[64] Leslie J. Rosenberg. Dark-matter QCD-axion searches. *Proc.Nat.Acad.Sci.*, 2015.

[65] B. Rossi and K. Greisen. Cosmic Ray Theory. *Reviews of Modern Physics*, 13:240–309, October 1941.

[66] Pasquale Dario Serpico and Dan Hooper. Gamma-rays from Dark Matter Annihilation in the Central Region of the Galaxy. *New J.Phys.*, 11:105010, 2009.

[67] Meng Su, Tracy R. Slatyer, and Douglas P. Finkbeiner. Giant Gamma-ray Bubbles from Fermi-LAT: AGN Activity or Bipolar Galactic Wind? *Astrophys.J.*, 724:1044–1082, 2010.

[68] R.A. Treumann and C.H. Jaroschek. Fundamentals of Non-relativistic Collisionless Shock Physics: V. Acceleration of Charged Particles. 2008.

[69] Ken'ichi Tsuchiya et al. Detection of sub-TeV gamma-rays from the Galactic Center direction by CANGAROO-II. *Astrophys. J.*, 606:L115–L118, 2004.

[70] Ralf Ulrich, Ralph Engel, and Michael Unger. Hadronic Multiparticle Production at Ultra-High Energies and Extensive Air Showers. *Phys.Rev.*, D83:054026, 2011.

[71] Moore T.J.T. Hoare M.G. Lumsden S.L. Mottram J.C. Thompson M.A. Urquhart J.S., Figura C.C. and Oudmaijer R.D. The RMS survey: galactic distribution of massive star formation. *MNRAS*, 437:1791–1807, 2014.

[72] Christopher van Eldik. Gamma rays from the Galactic Centre region: a review. 2015.

[73] Christopher van Eldik. Gamma rays from the Galactic Centre region: a review. *Astropart.Phys.*, 71:45–70, 2015.

[74] Q. Daniel Wang, F. J. Lu, and E. V. Gotthelf. G359.95-0.04: pulsar candidate near sgr a*. *Mon. Not. Roy. Astron. Soc.*, 367:937–944, 2006.

[75] T.C. Weekes. *Very High Energy gamma-ray Astronomy*. IOP Series in Astronomy and Astrophysics, 2003.

[76] F. Yusef-Zadeh, M. Morris, and D. Chance. Large, highly organized radio structures near the galactic centre. *Nature*, 310:557–561, August 1984.

[77] R. et al for the MAGIC collaboration. Zanin. MARS, the MAGIC analysis and reconstruction software. In *Proceedings, 33rd International Cosmic Ray Conference (ICRC2013)*, 2013.

List of Figures

1.1 Sketch of electron Bremsstrahlung. 8
1.2 Geometry of synchrotron emission and its power spectrum. 9
1.3 Spectrum of Inverse Compton radiation and typical spectral energy distribution of a AGN. 10
1.4 A cosmic ray "scattering" in a magnetic cloud moving with velocity V [47] . 11
1.5 The schematic representation of the diffuse shock acceleration of a charged particle. 12
1.6 The all sky image above 1 GeV constructed from two years of observations by Fermi Gamma-ray Space Telescope. 13
1.7 Reconstructed Fermi-LAT spectral energy distribution of the sun's flares. . . 14
1.8 Spectrum of the Galactic diffuse gamma ray emission from the Galactic center region. 15
1.9 Sites and radiation mechanism of non thermal emission in pulsars 16
1.10 Pulsar's magnetosphere and polar cap and outer gap models. 17
1.11 Possible scenarios for gamma-ray emission in binary sistems 18
1.12 Unified model for AGNs explaining the different observed emission as a function of viewing angle. If the AGN is observed perpendicular to the direction of the jets, the torus obscures the black holes and the galaxies is seen either as radio loud or radio quiet. As the viewing angle decreases, also emission lines from the gas clouds are visibile; when the observed is aligned along the jets, their emission becomes the most dominant and the Doppler effect boosts the emission so that VHE gamma-rays are observed; this object is classified a blazar. . . . 19
1.13 Jet structure of a GRB. 20

2.1 Electromagnetic shower as described by the Heitler model 22
2.2 The longitudinal development of an electromagnetic shower for different primary gamma ray energies 23
2.3 A schematic diagram of the developement of the interaction of a Cosmic Ray with the Earth's atmosphere [57] 24
2.4 Simulated electromagnetic shower on the left and hadronic shower on the right produced by a primary particle with 100 GeV energy. 26
2.5 Cherenkov lightpool as a superposition of Cherenkov emission at different altitudes. 27
2.6 Sketch of the primary particle's path. 28
2.7 Illustration of the Hillas parameters. 29
2.8 Images on the camera as produced by a gamma shower, an hadronic shower, a muon event and a background event 30
2.9 Different distribution of some parameters for gamma and hadronic showers . 31

2.10 The HESS telescopes situated in Namibia. [29] . . . 32
2.11 The FLWO basecamp and the VERITAS telescopes situated in Arizona. [28] 32
2.12 The MAGIC telescopes situated in La Palma at the Roques de los Muchachos. 33
2.13 The MAGICs reflector surface. . . . 34
2.14 Frame of the MAGIC telescopes . . . 35
2.15 Camera of MAGIC-I. . . . 35
2.16 The macrocell structure of the Sum-Trigger in the camera . . . 37

3.1 The swiss astronomer Fritz Zwicky. . . . 39
3.2 Rotation curve of NGC3198 spiral galaxy. . . . 40
3.3 Composite image of the Bullet Cluster. . . . 41
3.4 The power spectrum of the CMB. . . . 43
3.5 Simulations of CDM, WDM and HDM scale structure. . . . 45
3.6 The particles and relative sparticles Zoo. [15] . . . 46
3.7 upper limits for WIMP annihilation cross section as a function of the WIMP mass as obtained from the ATLAS monojet analysis. . . . 47
3.8 The three different sources and energy distribution of γrays production by WIMP annihilation. . . . 48
3.9 On the left, the annihilation spectra for a 100 GeV WIMP, on the right for a 500 GeV WIMP, for different annihilation modes. [66] . . . 49

4.1 Radio image of the GC from the VLA at $\lambda = 90cm$. . . . 52
4.2 Chandra X-ray map in Galactic coordinates of a $2^o \times 0.8^o$ region around the GC. . . . 53
4.3 Cloud model and shocked stellar wind model for the G2 cloud. . . . 54
4.4 Images from infrared light coming from glowing hydrogen of the G2's orbit. . 55
4.5 Fermi Bubbles' image. . . . 56
4.6 Navarro, Frenk and White profile in 2008. . . . 57
4.7 Gamma-ray spectrum of the GC source HESS J1745-290 . . . 59
4.8 Spectral energy distribution of Fermi-LAT source 2FGL J175.6-2858. . . . 59
4.9 Map of the 90cm VLA radio flux density of 20 pc around the GC coming from the SgrA East as a shell like structure surrounding SgrA* in projection. . . . 60
4.10 Fit of the Fermi and Hess data points for a hadronic model requiting a time variability for the protons production. . . . 62
4.11 Fit of the Fermi and Hess data points for a hadronic model without requiring any time variability of protons production. . . . 63
4.12 The calculated spectra produced in the hybrid model . . . 64
4.13 Fit of the combined emission of HESS J1745-290 and 2FGL J1745.6-2858 as orginated from a DM mass of$\sim$ 52 GeV annihilating into $W^{\pm}$ and an underlying background spectrum. . . . 65
4.14 Measured spectrum of the Galactic Center within 0.5^o on the left and 3^o on the right. . . . 65

5.1 Representation of the MARS analysis chain . . . 68
5.2 Zd distribution of the GC data . . . 69
5.3 Median DC and Transimission as a function of the Julian days for the GC data 69
5.4 Angular distribution of the Off data. . . . 70
5.5 Median DC and Transimission as a function of the Julian days for the Off data 71
5.6 Wobble mode in case of two wobbles. . . . 72

5.7 Theta-square plots of the GC 74
5.8 Skymap of the GC with the relative flux of the On and Off region. 74
5.9 Hadronness cuts as a function of Estimated energy and Migration Matrix, produced by flute 75
5.10 Spectral Energy Distribution of the GC 75
5.11 Density profiles and corresponding J-factors for GC. 77
5.12 Q factor for the GC. 78
5.13 Upper limits for the $< \sigma v >$ obtained by this work. 81

6.1 Maps of the observed gamma-ray flux in the energy range 1-100 GeV and of the optimized ROI for the Einasto and NFW dark matter profiles 83
6.2 Fermi results for upper limits on $< \sigma v >$ of DM self annihilating into a $b\bar{b}$ decay channel for NFW and Einasto DM profiles. 84
6.3 Signal and background region for a single telescope pointing position. 85
6.4 Representation of the signal and background regions for the HESS observations. 86
6.5 Upper limits on the $< \sigma v >$ of self annihilating dark matter as a function of its mass as obtained by HESS. 86
6.6 Upper limits on the velocity averaged dark matter self annihilation cross section for a $b\bar{b}$ decay channel with a 95% CL as obtained by this work, by the FERMI-Lat and by HESS. The orange line shows the thermal relic DM $< \sigma v >$ which corresponds to $3 \times 10^{-26}\,\mathrm{cm^3 s^{-1}}$. 87

A.1 Left: representation of the Fermi-LAT. Right: schematic strucuture of the LAT. i

B.1 The local polarization produced in a medium during the passage of a particle; on the left the case where the velocity of the particle is $v < c/n$, on the right where the velocity of the particle is $v > c/n$. [75] ii
B.2 Spectra of the Cherenkov radiation produced by gamma-ray induced extensive air showe at 10 km a.s.l. (solid line) and at 2200 m a.s.l., after the absorption mechanism lead to strong spectral extinction at lower wavelenght. iii

C.1 Sketch of the DISP parameter on the camera. iv

D.1 Ground light density and light density profile for a 100 GeV photons v
D.2 Effective area versus true energy. vi
D.3 Dependence of the effective area on the zenith angle. viii

List of Tables